SURFACE MODIFICATION OF TITANIUM DIOXIDE NANOPARTICLES

by

CLIFTON COUSHATTA WATKINS

SHANE C. STREET, COMMITTEE CHAIR
KEVIN H. SHAUGHNESSY
GREGORY B. THOMPSON
SILAS C. BLACKSTOCK
DAVID E. NIKLES

A DISSERTATION

Submitted in partial fulfillment of the requirements
for the degree of Doctor of Philosophy
in the Department of Chemistry
in the Graduate School of
The University of Alabama

TUSCALOOSA, ALABAMA

2016

ABSTRACT

Nanocrystalline titanium dioxide (TiO_2), a wide band-gap semiconductor, is synthesized by a sol-gel method for studies of its photocatalytic activity. In this work, surface modification of TiO_2 utilizing various species is performed. The surface modifications are performed on both pure and doped TiO_2. It is shown that surface modifications affect the phase transition temperature of TiO_2. Band gap energy modifications, via dopants, in combination with surface absorbed species have been shown to affect the photocatalytic activity of TiO_2. Surface adsorbed species must be inert to redox reactions in order remain bound to the surface, yet facilitate charge transport from the TiO_2 bulk into a species on the surface. Typically dye sensitizers are anchored to semiconductor oxide surfaces via carboxylates. The polarization at the carboxylate-oxide interface junction may interfere with the charge injection process. Here, the use of anchors containing species of different polarities (phosphates, sulfates, silicates, etc.) at the interface junction is analyzed for improvements in the charge injection process. This charge injection process is measured by observing the extent in which methylene blue is degraded. In this work, characterization is performed by a variety of microscopic and spectroscopic techniques.

DEDICATION

This dissertation is dedicated to Lauren, my lovely wife and my best friend, for constantly providing me with support and the motivation to persevere despite significant time away while pursuing its completion. I also dedicate this dissertation to our children for always holding me to a higher standard. Also, to my parents, take this dissertation as tangible proof that your messages of hard work and determination were well received. Lastly, this is also dedicated to my siblings, family and friends for helping to mold me into the person that I am today.

LIST OF ABBREVIATONS AND SYMBOLS

°C	Degrees Celsius
λ_{max}	Maximum wavelength
α-A	Amorphous to Anatase transition
A-R	Anatase to Rutile transition
a.u.	Arbitrary/Absorbance units
APTES	(3-Aminopropyl)triethoxysilane
Ar-ion	Argon ion (laser)
Arb units	Arbitrary Units
B-mod	Borate modified
B-R	Brookite to Rutile transition
Btu	British Thermal Unit
C-mod	Carboxylate modified
CB	Conduction Band
CCD	Charge Coupled Device
cm^{-1}	Wavenumbers
CPS	Counts per second
DRIFTS	Diffuse Reflectance Infrared Fourier Transform Spectroscopy
EDS	Energy Dispersive Spectroscopy
eV	Electron Volt
EtOH	Ethanol; ethyl alcohol

FTIR	Fourier Transform Infrared Spectroscopy
He-Ne	Helium-Neon (laser)
IPA	Isopropanol; 2-propanol; isopropyl alcohol
IR	Infrared
keV	Kiloelectron volt
kV	Kilovolt
kWh	Kilowatt hour
mL	Milliliter
M	Molarity
MCT	Mercury Cadmium Telluride
mg	milligram
mL	milliliter
mol	Mole
mW	milliWatt
pH	Negative Logarithm of the H^+ Concentration
nm	nanometer
P-mod	Phosphate modified
PTT	Phase Transition Temperature
Raman	Raman Spectroscopy
ROS	Reactive Oxygen Species
RPM	Revolution per minute
S-mod	Sulfate modified
Si-mod	Silicate modified

SMS	Surface modifier/modification species
SST	Sea surface temperature
Ti-but	Titanium butoxide
Ti-O*i*Pr	Titanium(IV) isopropoxide
UV	Ultraviolet
UV-Vis	Ultraviolet-Visible Spectroscopy
VB	Valence Band
XPS	X-ray photoelectron spectroscopy
XRD	X-ray diffraction

ACKNOWLEDGMENTS

First and foremost, I would like to thank my Lord and savior, Jesus Christ, for providing me with the capability to read, comprehend, and perform to the best of my ability. I would also like to thank my co-research advisors, Dr. David Nikles and Dr. Shane Street, for their support and patience while seeing me through this degree program. To these gentlemen, I also have a great appreciation for collectively molding me into both the person and scientist that I am today by utilizing their contrasting yet equally effective supervisory styles. I am very grateful to my committee members, Dr. Shaughnessy, Dr. Blackstock and Dr. Thompson for serving and assessing my dissertation.

I would like to thank the University of Alabama for providing me with the opportunity and facilities to complete my studies. Special thanks to the faculty, support staff and funding sources (Southern Regional Education Board- external funding; chemistry department- internal funding). I want to acknowledge past and present group members- while not a comprehensive listing- Dr. James Burgess, Dr. Shelby Shuler, Dr. Medhat Farahat, Dr. Dwayne Reed, Dr. Jeremy Pritchett, Dr. Keith McNeil, Dr. Amanda Glover, and Dr. Lei Zhang.

Lastly, I would like to thank the United States Marine Corps and the Department of Veteran Affairs. The experiences I encountered while affiliated with these two organizations taught me invaluable lessons about myself and I will forever be grateful for it.

CONTENTS

LIST OF TABLES

LIST OF FIGURES

CHAPTER 1 – INTRODUCTION

Titanium, originally discovered in 1791, was not appreciated for its remarkable properties until around 1925 when samples of sufficient purity were obtained. Its high strength to weight ratio led to its use mainly in the aeronautics industry. Titanium dioxide (TiO_2), identified in 1821, was first used as a yellow enamel opacifier in 1900. A Norwegian scientist would expand on this work by receiving a patent for utilizing TiO_2 as a pigment in 1913.[1] Despite the advances, it was not until 1916 that the technology needed to mass produce TiO_2 was developed.[2] By the late 1950s the production of high quality white TiO_2 pigment had been achieved. Also in the 1950s, the versatility of TiO_2 was made evident when the discovery of a native oxide layer was determined to be the reason that titanium metal exhibited excellent corrosion resistant properties.[3] The next major step in the technological "evolution" of TiO_2 came in 1972 when Fujishima and Honda showed that chemical reactions could be driven by its ability to absorb UV photons.[4] From this process, commonly referred to as photoactivity, a multitude of TiO_2 based technologies have spawned. The common theme in technologies including TiO_2 is that they all involve reactions at the surface, so as the nature of the surface changes its ability to perform certain functions does as well.

This dissertation will focus on the interfacial chemistry of titanium dioxide and how manipulations of its surface can alter the properties otherwise present in its unmodified, or pristine, condition. This introductory chapter will summarize the properties of TiO_2 and modifications that can affect the photoactivity.

1.1 Energy and Human History

Over the course of history, the ability to capture energy has been fundamental to the survival of life. Autotrophs, organisms that require relatively simple compounds for metabolic synthesis, obtain the necessary energy to do so from solar radiation or inorganic chemical reactions. On the other hand, heterotrophs, organisms that require complex organic compounds for metabolic synthesis, get their energy from autotrophs. As humans evolved, the knowledge of how to control fire over 400,000 years ago proved to be the most important use of energy created outside the body. The utilization of fire to extract energy from recently deceased organisms was man's first incursion into utilizing large amounts of energy that was stored many years prior. As the millennia passed with no significant advances in new energy rich materials, it was not until about 300 years ago that the use of fossil fuels became a mainstay in human civilization.[5] Despite the inefficiency in how fossil fuels are used, the low cost abundance of energy they contain has and continues to sustain an unprecedented worldwide population growth that began during the industrial revolution and continues through present times.

With the continued and prolonged use of fossil fuels, a better understanding of their origin, availability and sustainability has been acquired. For many decades now, there has been a common understanding that the rates in which these resources are being consumed far exceed the rates in which they are produced. Consequently, the great scientific and technological challenge of the early 21st century is the availability and exploitation of inexpensive sources of renewable energy. In 2014, approximately 89% of the United States' energy demands were met by non-renewable sources, among which fossil fuels (coal, natural gas and petroleum) claimed the overwhelming majority (~81%).[6] While nonrenewable energy sources provide consumers with the lowest cost per kWh, environmental concerns resulting from their utilization has forced many to look beyond the direct economic benefits. When considering the constantly depleting stockpiles and the environmental concerns, the general focus has shifted from nonrenewable to renewable energy sources. Such a shift, even if partially implemented, would have a significant impact on the way our society currently produces and utilizes energy. The most recent data shows that renewable energy accounts for about 10% (Figure 1.1) of the United States energy production. Although hydroelectric, wind, biomass, geothermal and solar are all considered renewable, no source shows more potential than solar energy. The amount of solar energy that strikes the Earth's surface in one hour is enough to power the world's energy demands for an entire year.[7] To this end, solar energy is the most obvious choice as a long term solution for meeting the world's energy demands. Photosynthesis, the process by which organisms convert solar energy into chemical energy, is the most prevalent example of using solar energy to meet energy requirements.[8] While green plants are the most common example, simple bacteria and blue-green algae are among the earliest organisms to employ the photosynthesis process.[5] Despite photosynthesis being nature's way of harvesting and utilizing solar energy, other naturally occurring materials have shown the ability mimic photosynthesis. Unlike photosynthesis, which occurs in living organisms, these non-living materials have an added level of versatility in that life sustaining conditions need not be considered when utilizing their photoactive properties.

1.2 Concept of Photoactivity

Photochemistry is the general term used to define the interactions of light with matter. Though light, or electromagnetic radiation, consists of a wide range of wavelengths,

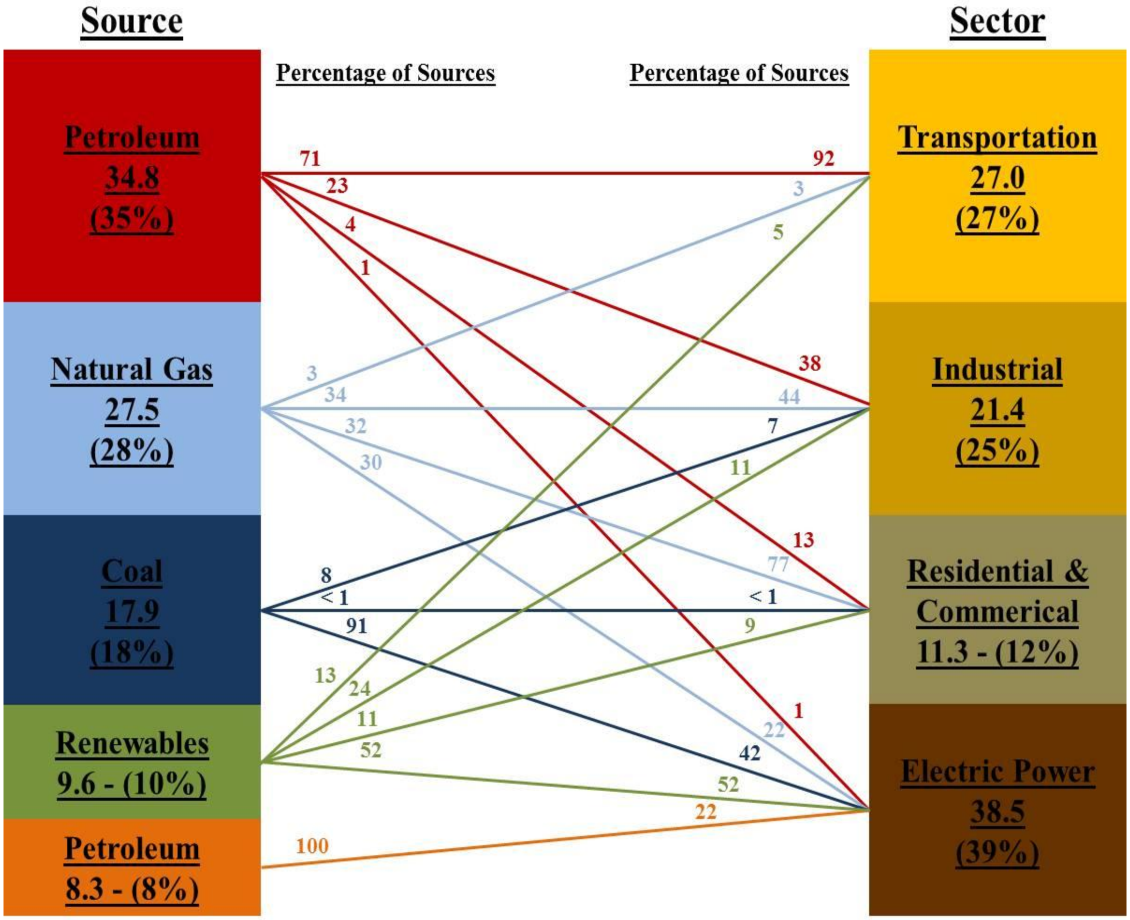

Figure 1.1: Primary energy consumption by source and sector for 2014. Units are petaBtu (10^{15}); adapted from ref. [6].

photochemistry typically deals with the infrared, visible, and ultra-violent ranges.[8] The term photochemistry is generally used regardless of whether the interaction of matter with light causes a reaction or light is produced as a result of a reaction. In this dissertation, the focus will be on the former.

The total energy of an atom or molecule is the sum of three components: the motion of its electrons, the vibrations of atoms contained within, and the rotation of the species in its entirety (equation 1.1).[9] The energy levels of the three aforementioned states are quantized, that is they

$$E_{total} = E_{el} + E_{vib} + E_{rot} \tag{1.1}$$

have specifically defined yet separate energy states which are the only allowed energy levels. When light is absorbed by an atom or molecule in its ground state (lowest electronic energy state), the formation of an excited state (species containing excess energy) occurs. The Bohr condition asserts that for this transition to occur, the incident radiation must have the same energy as the energy difference between the initial state and the final state (figure 1.2).[8] Although not drawn to scale, figure 1.3 shows the transitions of the three types of energies that compose the total energy of a diatomic molecule. When the incident radiation is infrared (IR), visible, or ultraviolet (UV), the extent of chemical processes that occur as a result of these electronically excited states is generally termed photoactivity.

1.3 Photocatalysis

There are many naturally occurring compounds that exhibit photoactive properties. The ability of these compounds to absorb light is governed by their band gap energy. According to

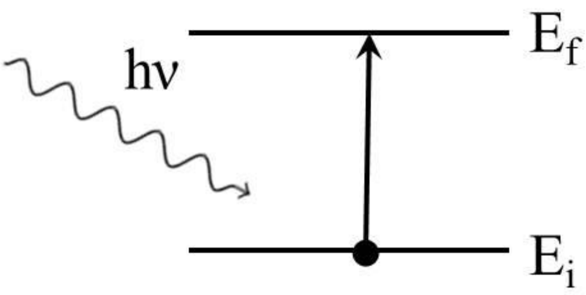

Figure 1.2: Excitation of species from initial state to final (excited) state by the absorption of radiation; modified from ref. [8]

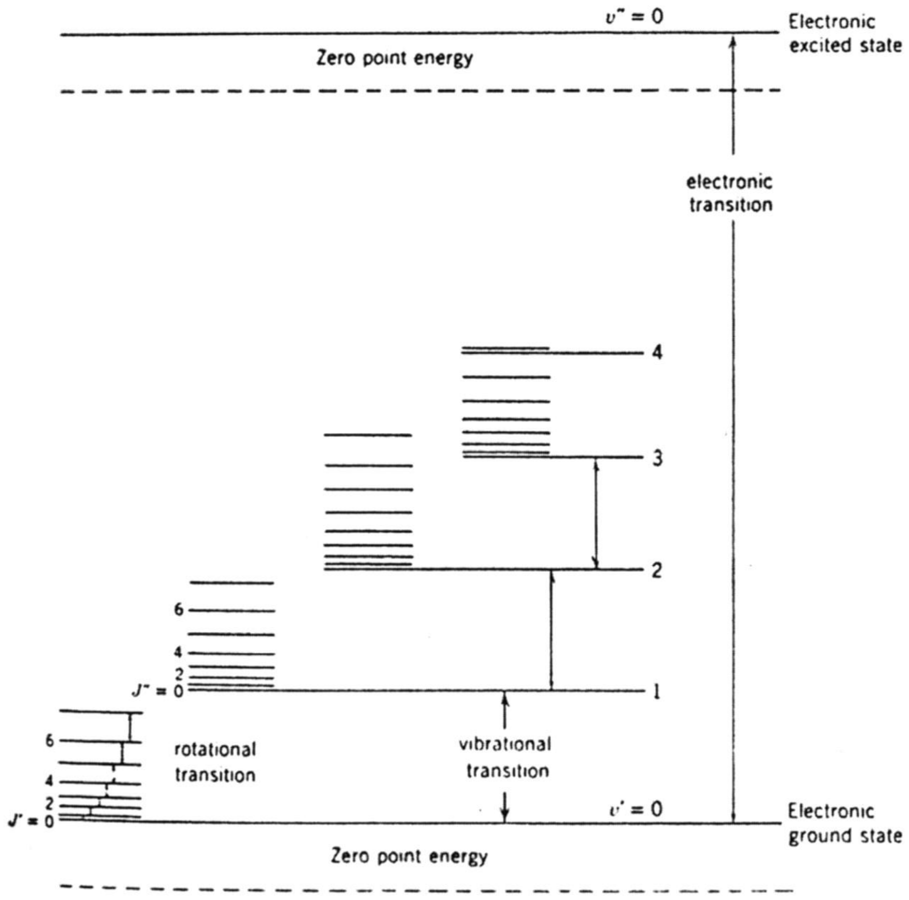

Figure 1.3: Energy levels of a diatomic molecule (the spaces between energy levels are not drawn to scale); modified from ref. [9].

band theory, when the wave functions of atoms interact the outcome is a wave function of lower energy and one of higher energy. A more stable (lower energy) bonding orbital and a less stable (higher energy) antibonding orbital is the result of this interaction.[10] Once created, electrons will fill these newly formed orbitals in the lowest energy conformation possible. In doing so, the lower energy orbital (valence band) will be filled while the higher energy orbital (conduction band) will not. In specific cases, the top of the filled valence band (VB), also known as Fermi level, is separated from the conduction band (CB) by the band gap. This “distance” between the two bands, in energy, is used to categorize compounds as conductors, semiconductors, or insulators. A visual representation of the band gaps for the three classes of solids are shown in figure 1.4.[11] In conductors there is no band gap energy as the VB and CB overlap which allows for the free movement of electrons between the two bands and therefore conduction through the crystal. In both semiconductors and insulators, the band gaps have defined values with the magnitude of energy between the two bands being the determining factor. While the energy differences are somewhat arbitrary, semiconductors have band gap energies less than 5.0 electron volts (eV) and insulators have band gap energies greater than 5.0 eV.[10] When considering the solar radiation that strikes the Earth’s surface, as shown in figure 1.5, very little if any of the radiation exceeds about 4.5 eV.[12] Thus, the utilization of semiconductors as a means of harvesting solar radiation for the purpose of driving chemical processes is firmly supported by theory as these energy levels have properly overlapping ranges.

Some semiconductor materials are commonly termed “wide band-gap semiconductors”- a term, while it is not very clearly defined, generally refers to materials with band gap energies falling in the visible to UV range. These wide band-gap semiconductor materials are steadily being discovered as modifications to the structure of the naturally occurring compounds allow

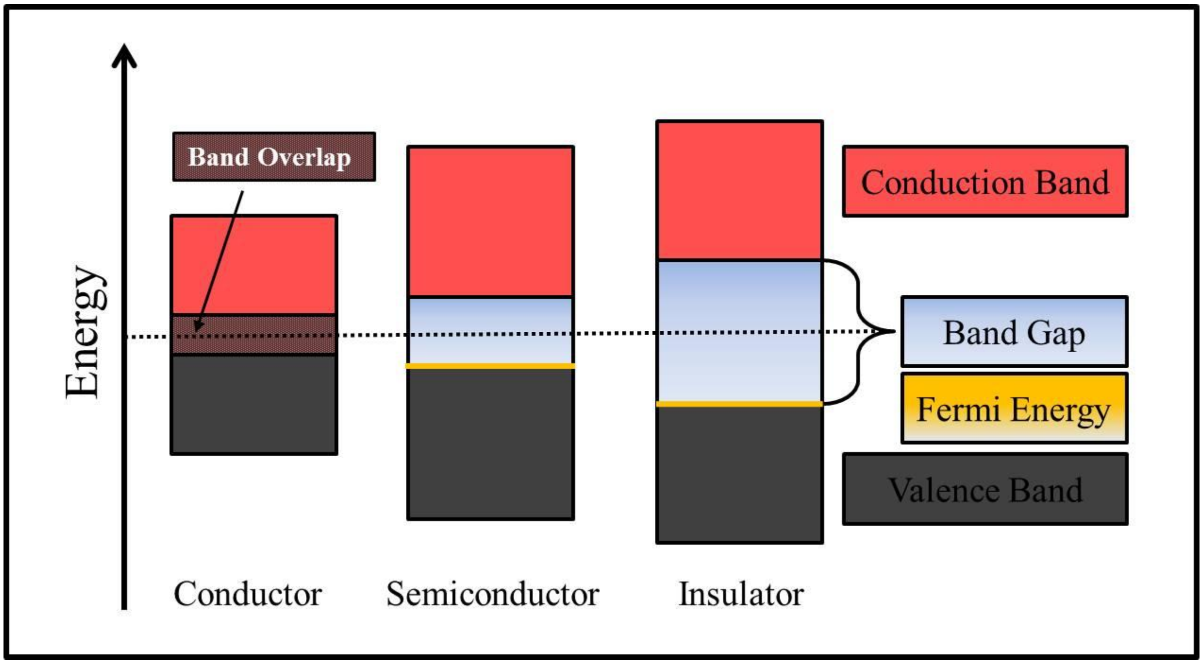

Figure 1.4: Cartoon of the band gap for three classes of solids; modified from ref. [11].

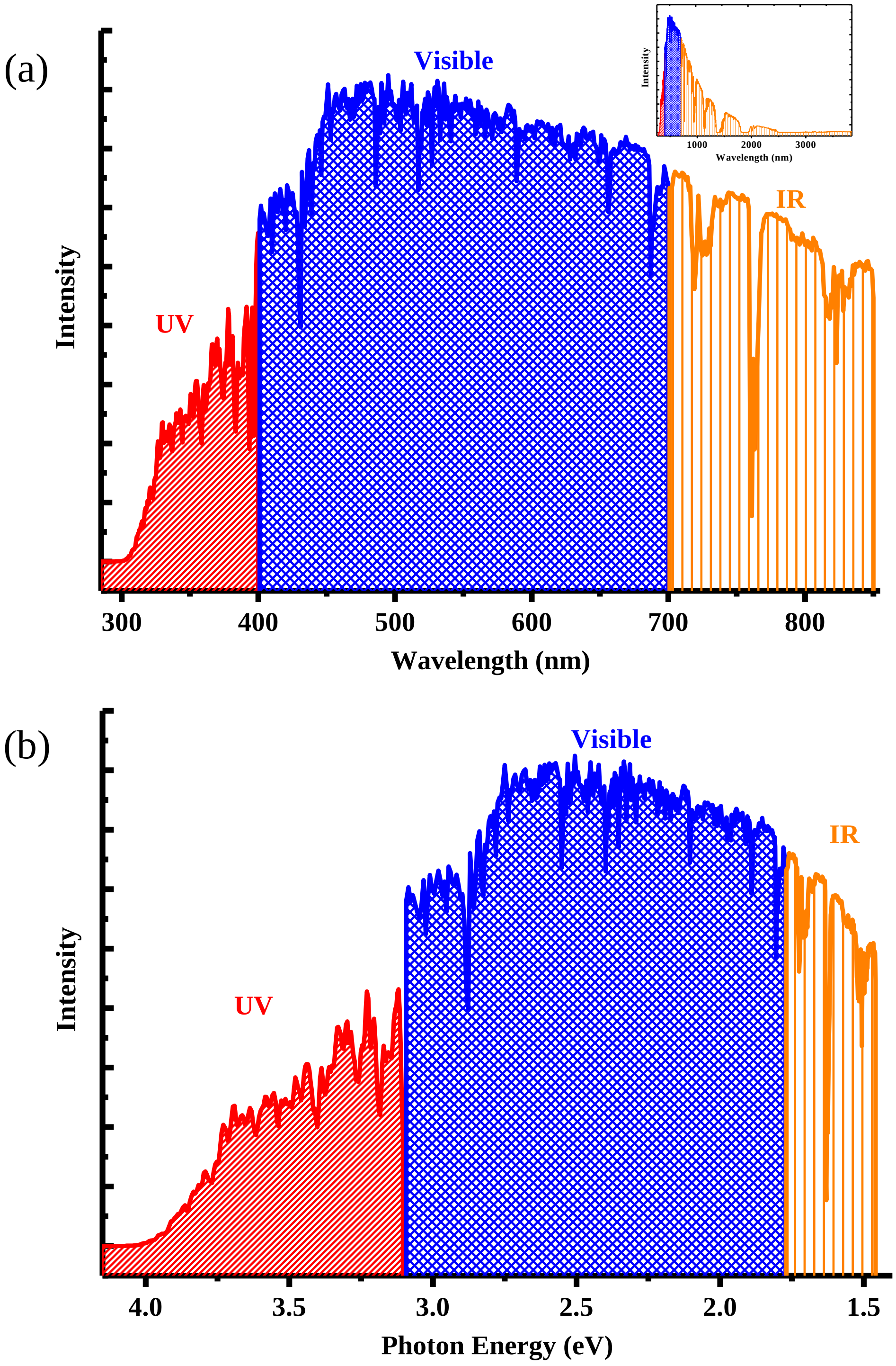

Figure 1.5: Spectra of solar radiation incident upon Earth's surface at 53° from zenith- given in (a) wavelength and (b) electron volts; adapted from ref. [12].

for the desired band gap energy to be achieved. Although oftentimes the parent compound has been well studied and has proven useful for a specific technology, these modifications induce changes that can allow for a host of new capabilities previously determined to be impossible by the unmodified semiconducting molecule.

1.4 Titanium Dioxide

Titanium dioxide (TiO_2), also known as titania, is a naturally occurring mineral that possesses a wide range of applications. Some applications include food additives, coatings, paper, plastics, sunscreens and cosmetics.[13-15] Its versatility is mainly attributed to being chemically inert, relatively low in cost, and abundant.[16, 17] Despite its many uses, the most prevalent use of TiO_2 is as a white powder pigment due largely to its bright white color, very high refractive index, and ability to retain its white color after exposure to UV light.[15]

Commercial applications of photodriven processes utilizing TiO_2 include air and water sanitation,[18, 19] self-cleaning glass,[20] and anti-fog coatings.[21] The aforementioned technologies as well as many lab-scale technologies (water splitting for H_2 production, specialty chemical production,[22] CO_2 reduction to useful compounds, large scale wastewater remediation, etc.) utilize sunlight as the energy source. TiO_2 in its pristine, or unmodified, state has a bandgap energy that allows for the absorption of UV light. With only about 4% of incident sunlight falling in the UV range, there has been a steady increase in research devoted to increasing the photoactivity of TiO_2. Two types of modifications are often used: bulk and surface modifications. Bulk modifications involve introducing impurities into the crystal lattice of the material to modify the bandgap whereas surface modification is when a species is adsorbed to

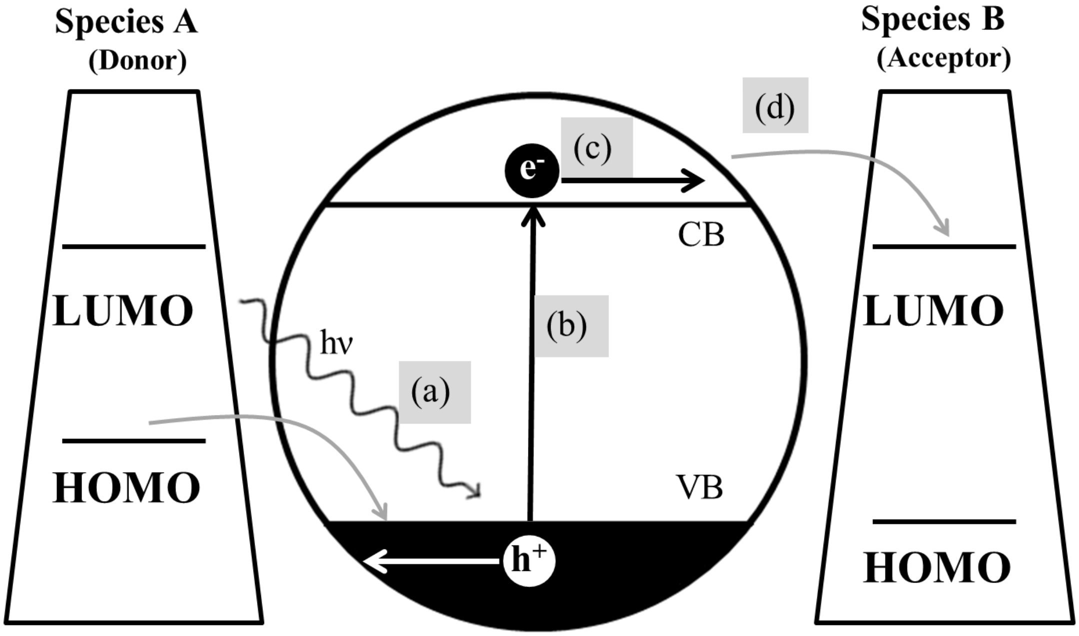

Figure 1.6: General mechanism for photoactivity of TiO_2: (a) a photon is absorbed as light interacts with the sample; (b) absorbed energy promotes an electron from the valence band to the conduction band; (c) both the electron (e^-) and hole (h^+) created by the electron's excitation migrate to the surface of the particle; (d) the electron and hole react with surface absorbed species

the surface in order to facilitate the attachment of other photon capturing molecules. The photoactivity of TiO_2 can be generally described by four steps, as shown in figure 1.6: (a) light interacts with the sample and a photon is absorbed; (b) the energy absorbed promotes an electron from the valence band to the conduction band- this separation of charge prompts the creation of a positively charged hole and a negatively charged electron pair (c) both the electron (e^-) and hole (h^+) created by the electron's excitation migrate to the surface of the particle; (d) the electron and hole react with surface absorbed species- often as competing (oxidative/reductive) reactions. The photodriven TiO_2 reaction mechanism is often shown as the following chemical reactions (eq. 1.2). Furthermore, surface absorbed species (shown as donor and acceptor in figure 1.6) are reacted upon by either hydroxyl radicals or superoxide species that result when the e^- and h^+

$$TiO_2 + h\nu \rightarrow e^- + h^+ \tag{1.2}$$

$$H^+ + H_2O \rightarrow H^+ + \cdot(OH)^- \tag{1.3}$$

$$e^- + O_2 \rightarrow \cdot O_2^- \tag{1.4}$$

react with water and O_2 molecules that are innately present on metal oxides.[23] Subsequent reactions of hydroxyl radicals and superoxide species lead to the creation of other oxygen containing species such perhydroxyl (HOO·) and hydrogen peroxide (H_2O_2), commonly included in a general class of compounds referred to as reactive oxygen species (ROS), that are known to target molecules after migrating away from the surface of TiO_2.[24]

1.4.1 TiO_2 Morphology

With the exception of helium, all substances can be sufficiently cooled to form a solid phase.[25] Upon solidification, if the constituent atoms form a long range ordered threedimensional pattern, the structure is considered crystalline. Alternatively, if no long range ordered pattern is achieved the solid structure is termed amorphous. While some compounds solidify in a single orientation every time, there are also others in which the positioning of the component atoms can vary slightly upon solidification. When this phenomenon occurs among species with the same component atoms, polymorphs are formed. It is important to note that polymorphs are commonly referred to as phases and the two terms are often used interchangeably.

TiO_2 is known to have many different polymorphs- both man-made and naturally occurring.[26-29] Of these polymorphs, the three most common are anatase, rutile and brookite as shown in figure 1.7. Brookite, being the least studied of the three, shares many of the same properties as rutile while also exhibiting the same general chemistry.[30] The main disadvantage of brookite, when compared to the other two polymorphs, is that it has a bandgap energy that is slightly larger which makes it much less effective as a photocatalyst (see figure 1.7). Anatase has been historically known as the preferred phase for photocatalytic studies as its band gap energy is the smallest of the three phases and consequently absorbs a greater percentage of incident sunlight. Rutile has traditionally been considered as the most stable phase and is the phase used in most industrial applications. Anatase and brookite are considered metastable because higher temperatures can induce their transformation to the most stable rutile phase. Both pristine and amorphous TiO_2 can be driven to anatase phase by heating to about 400 °C for 4 hours, and both anatase and brookite phases can be driven to rutile by heating to about 750 °C for 4 hours.[31] Thermodynamic stability however, has been shown to be particle-size dependent. Macrocrystalline samples, or samples larger than 14nm in diameter, prefer the rutile phase while microcrystalline (less than 14nm in diameter) samples prefer anatase.[32] As a result of small

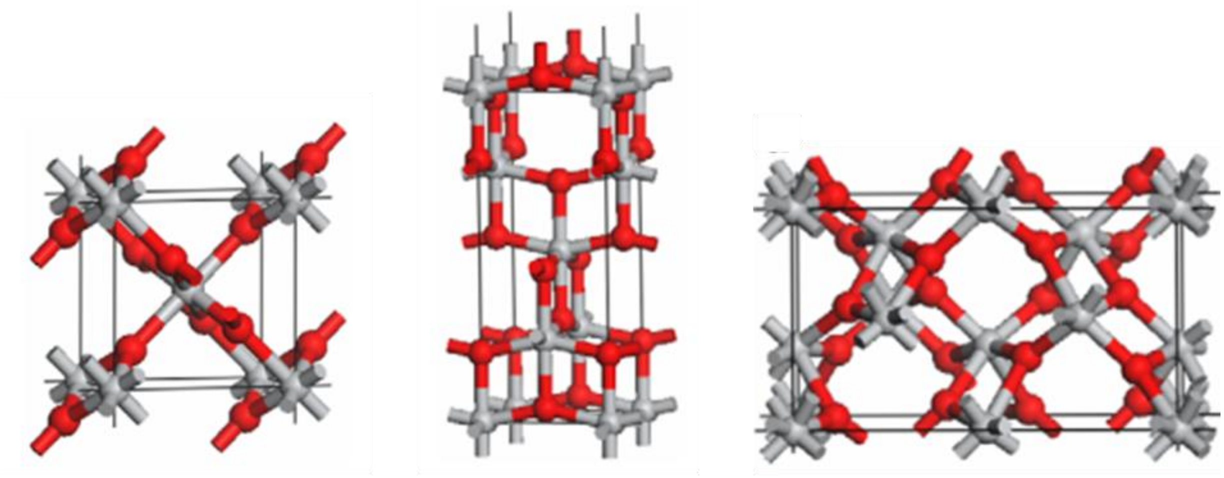

Rutile
3.2 eV

Anatase
3.0 eV

Brookite
3.1-3.4 eV

Figure 1.7: Unit cells and band gap energies of three naturally occurring TiO_2 polymorphs: rutile, anatase and brookite; reproduced from ref. [28].

microcrystalline TiO_2 particles preferring the anatase phase, many research groups have traditionally reported anatase to be the more photoactive phase. There is recent work in the literature, however, that indicates TiO_2 photoactivity is both particle size and surface area dependent.[33, 34] When these two properties are normalized for both anatase and rutile phases, they are determined to have very similar photoactivities.[35]

1.4.2 TiO_2 Synthesis

TiO_2 is both a very common and versatile mineral. While some applications require very precise specifications (such as particle size, morphology, impurity content, etc.), the most widely used applications do not. For those applications that do not require such specifications, processing of the TiO_2 beyond mining, cleaning and converting into a powder is not necessary. When pure TiO_2 is required, synthetic production generally falls into either vapor phase or solution phase catagories.[36]

Vapor phase production of TiO_2 typically involves the conversion of some titanium-bearing mineral to titanium tetrachloride ($TiCl_4$). During this process, commonly referred to as the chloride process, the titanium ore is exposed to chlorine gas at ~900 °C while in the presence of petroleum coke as a reducing agent which promotes titanium conversion to $TiCl_4$. The purification of $TiCl_4$ is achieved by the removal of other volatile and non-volatile metal chlorides. Chloride gas is then removed from the purified $TiCl_4$ as the sample is oxidized by heating to 985 °C in an oxygen flame, thus forming highly crystalline TiO_2.[37]

Synthetic reactions involving metal alkoxides have been extensively studied with experiments dating back as early as the mid 1900's.[38-40] When exposed to water, metal alkoxides undergo a vigorous hydrolysis reaction that produce metal hydroxides or hydrated oxides as shown in the general reaction equation below (eq. 1.5). After the hydrolysis reaction begins, a concurrent and competing polymerization reaction begins.[41, 42] The initial hydrolysis reaction (eq. 1.6) produces partially and/or completely hydrolyzed metal species that depend on the reaction kinetics. The second polymerization reaction (eq. 1.7) arranges the hydrolyzed products into a polymeric network. The solid inorganic network formed during the polymerization

$$\mathrm{M{-}(OR)_n + H_2O \rightarrow M{-}(OH)_n + nR{-}(OH)} \qquad (1.5)$$

$$\mathrm{{\equiv}Ti{-}(OR) + H_2O \rightarrow {\equiv}Ti{-}(OH) + R{-}(OH)} \qquad (1.6)$$

$$\mathrm{{\equiv}Ti{-}(OH) + (RO){-}Ti{\equiv} \rightarrow {\equiv}Ti{-}O{-}Ti{\equiv} + R{-}(OH)} \qquad (1.7)$$

reaction proceeds as far as the hydrolysis conditions allow. The hydrolysis reaction conditions dictate the relative concentrations of the terminating bonds (OH) of the polymerization reaction by altering the reaction kinetics, thus ultimately controlling particle size and morphology.[43] Titanium alkoxides most often used in sol-gel reactions include ethoxide, butoxide and isopropoxide as the carbonaceous species.[44-51] In the aqueous environment, the carbonaceous alkoxide species ultimately dissociates from the metal and forms the appropriate alcohol. This reaction process has commonly become known as the sol-gel synthesis method.[41] Sols are defined as colloidal (1-100 nm) particles within a liquid, while gels generally refer to an interconnected rigid network of polymeric chains with lengths greater than a micrometer and pores of submicrometer dimensions.[52] When performed at room temperature and pressure, the sol-gel method produces amorphous TiO_2 particles with size being controlled by the acidity of the water.[53-55] Once synthesis is complete, the amorphous particles are then annealed in order to induce crystallinity. A slight derivation of the sol-gel method, known as the hydrothermal method, uses increased pressures and/or temperatures during the synthesis step to produce crystalline particles.[56-58] This method most often employs an autoclave and typically produces larger particles with less surface area. The hydrothermal method has also been shown to produce highly crystalline TiO_2 particles of varying shapes.[59-62]

1.4.3 TiO_2 Bulk Modification (doping)

As is the case with many wide band gap semiconductors, it is not uncommon to incorporate ions into the crystal lattice of TiO_2. This modification of the bulk structure is known as doping. Introducing a dopant species can change the bandgap energy of TiO_2 by introducing extra bands into the band structure as shown in figure 1.8. These bands decrease the transition energy that electrons have to travel when going from valence to conduction band upon excitation. Pristine TiO_2 requires light in the UV range to overcome the bandgap energy, while dopants are capable of lowering the required excitation energy to the visible light range.

TiO_2 doping is typically achieved by adding the dopant species into the sol-gel mixture prior to the hydrolysis step (eq. 1.6). This places the dopant atoms into the TiO_2 lattice as it is being formed. It has also been suggested in literature that co-crystallization occurs as the trace amounts of oxides are formed and trapped within the porous nanostructure when using transition metal cations as the dopant species.[27] A recent study has introduced the idea of "surface doped" TiO_2 in a literal sense. In this study, pure TiO_2 powders were prepared then dispersed in a coating solution that contained a titanium precursor and transition metal ions.[63] This study takes advantage of the idea that surface cations can enhance photoactivity by promoting charge carrier separation, providing more reaction sites and preventing the individual particles from aggregating.[64, 65]

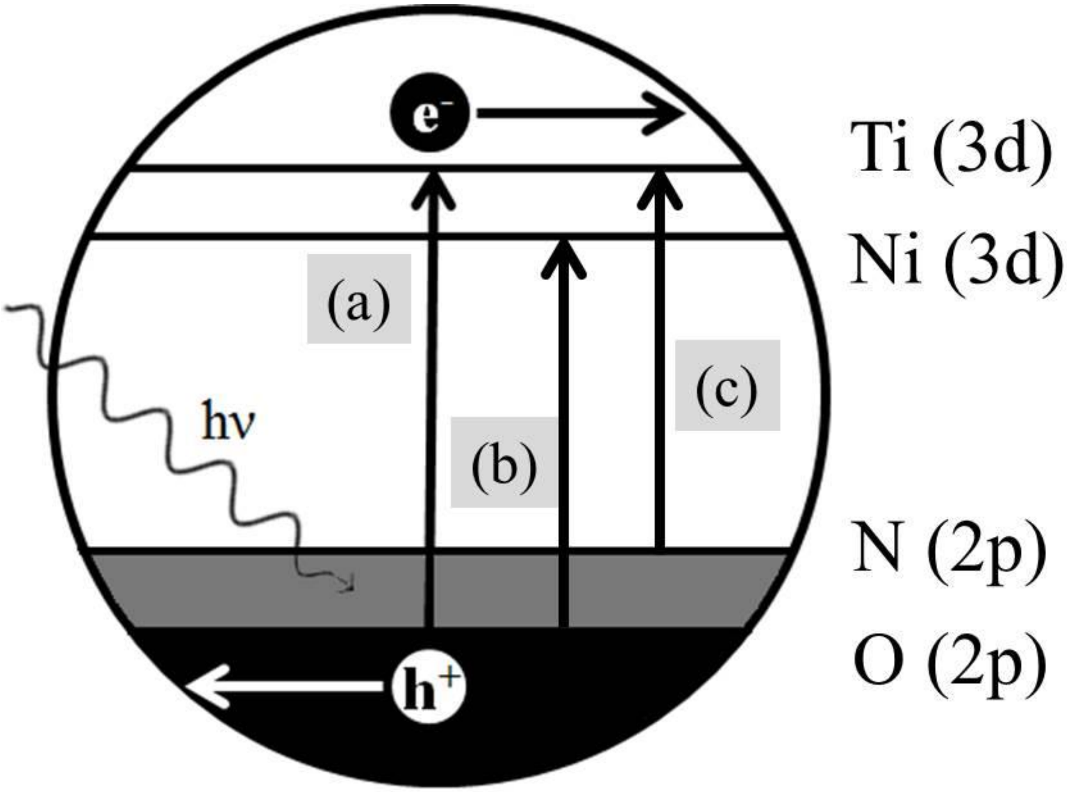

Figure 1.8: Cartoon demonstrating the effect of doping on the bandgap of TiO_2. (a) pure TiO_2 requires light in the UV range to excite an electron from the VB to the CB; (b) TiO_2 doped with nickel atoms has a smaller band gap energy due to the lowering of the CB; (c) TiO_2 doped with nitrogen atoms has a smaller band gap energy due to the raising of the VB

Optimizing the photoactivity of doped TiO_2 can be a complicated process because the molecule being doped, nature of the dopant and concentration of the dopant can all be very important factors. Because TiO_2 is often doped then driven to a crystalline phase with high heat and/or pressure, cationic dopants are mostly used for they can survive the intense treatment conditions. There are studies that have attempted to use anionic dopants but they tend not to survive the intense heating process needed to induce crystallization.[66] Also, unless carefully managed, there is the potential for some carbon doping to occur as the organics from the precursor chemicals may not be completely removed from the sample – despite the intense treatment conditions.

1.4.4 TiO_2 Surface Modification

TiO_2 surface modification has been performed extensively for several years.[27, 67-73] The surface of TiO_2 is where all the chemistry occurs. Even after doping, the efficiency of TiO_2 as a photocatalysts is determined by the reactions that occur at the surface. An entire field was born in 1968 when it was discovered that organic dyes can generate electricity at oxide electrodes when illuminated.[74] Over the years, the nature of the organic dye has changed but the reason for implementing it remains unchanged. Because pristine TiO_2 absorbs UV light (a minor part of incident radiation), attaching an antennae molecule or light scavenger that is capable of absorbing the more abundant visible light found in incident sunlight could make this system a viable alternative energy capture material.

In the 1980's, photochemical experiments were performed with Ruthenium (II) 2,2'-bypridyl (Rubpy) based complexes utilizing TiO_2, in both particle and photoelectrode form, as the substrate material.[75, 76] In 1991, O'Regan and Gratzel expanded upon this work and developed the dye sensitized solar cell (DSSC).[77] Further experimentation utilizing TiO_2 electrodes and Rubpy complexes led to the development of a complex in 1993, recognized as N3 dye, that would stand as a benchmark standard in photovoltaic performance for about 8 years.[78, 79] The same research group establish a new benchmark in 2003 with the development and utilization of yet another Rubpy complex that has been coined "black dye".[80, 81] For years, the anchoring group for these molecular dyes was the carboxylate functional group.[82] The oxygen(s) on the carboxylate group are capable of bonding with exposed titanium sites present on the surface of TiO_2. Similarly, other inorganic oxoacids can be used to bind to the surface of TiO_2. In an aqueous system, such as the sol-gel reaction conditions, an oxoacid could be added as a reactant and successfully adsorbed to the surface.[83-85] The surface bound oxoacid will be termed "head group" or "anchoring group" throughout this work. Once adsorbed to the surface, the covalent nature of the intramolecular bonds of the head group can withstand the charge transfer process upon irradiation.

1.5 Determination of Photocatalytic Activity

There are countless ways in which TiO_2 can be modified in an attempt to enhance photocatalytic activity. After these modifications are performed, there are equally as many ways to determine if the respective modifications enhance or inhibit the photocatalytic activity. In the literature, the most common way of determining this is to monitor the concentration of a species that can be easily monitored by spectroscopic means. This idea is consistent with the purpose in which many commercial applications aspire to use TiO_2- decomposition of pollutants.

Model compounds, often organic dyes that have very intense electronic transitions, are most commonly used for qualitative analysis of one photocatalysts versus another. The simplest method for achieving this comparative analysis is to monitor the decrease in concentration as samples are irradiated with light with respect to time. A more thorough analysis can be performed by monitoring the decomposition products, for only then can a reaction mechanism be determined – oxidative or reductive. Because the rate of photodegradation can be affected by many conditions, it is important to keep conditions such as pH, temperature, light flux and concentrations as uniform as possible.

Although there are many model compounds to choose from, this work will employ the dye commonly known as methylene blue (MB). Like many of the dyes used for this purpose, it has a very strong electronic transition that can be easily monitored by UV-Vis spectroscopy. MB, a cationic dye that has been well studied for many years, has two general decomposition pathways. The reductive pathway, or pathway that uses electrons generated by TiO_2 photoexcitation, leads to the demethylation of MB until the final product, phenothiazine, is formed.[86] The oxidative pathway, or pathway that uses holes generated by TiO_2 photoexcitation, leads to the ring cleavage pathway.[87]

The demethylation, or reductive, pathway is the most common decomposition pathway for MB when used as part of TiO_2 photocatalytic studies. It is worth noting that there have been cases when both decomposition pathways have simultaneously occurred.[88-90] The disappearance of the intense blue color of MB can be used as a general indicator of photoactivity when used in this type system, but it should not be solely used as an indication of the reaction kinetics.

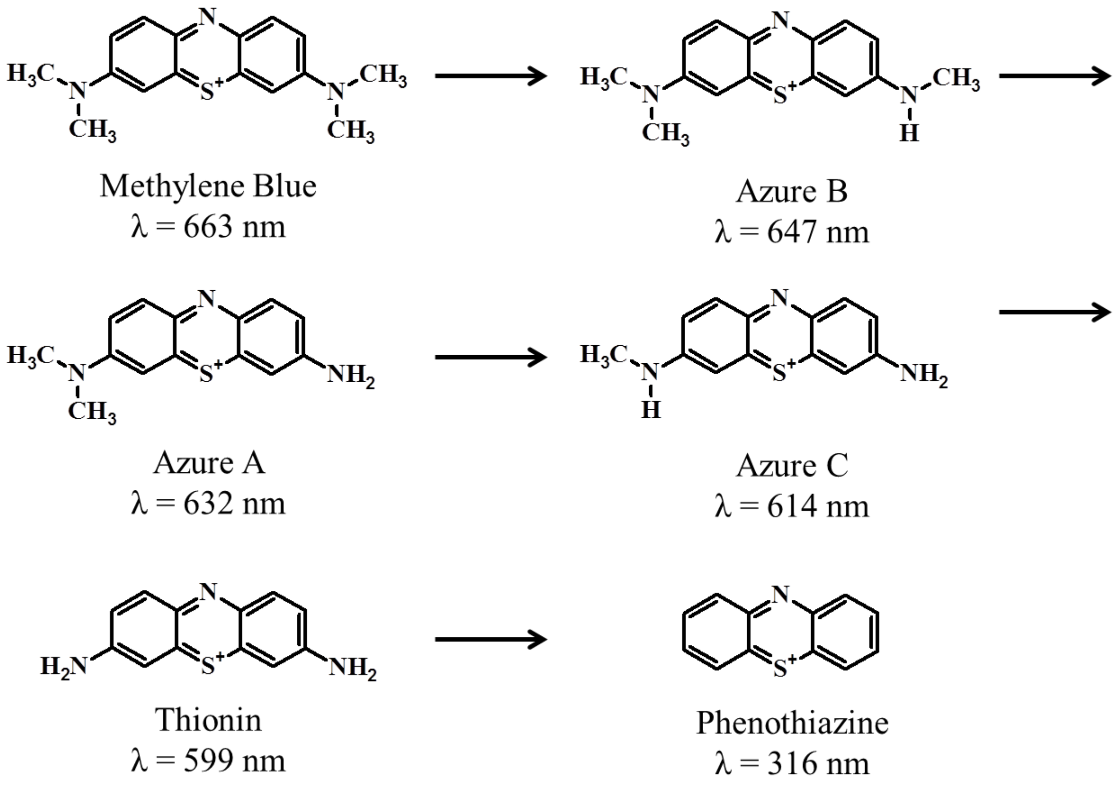

Figure 1.9: Degradation of methylene blue via the demethylation pathway; modified from ref. [88]

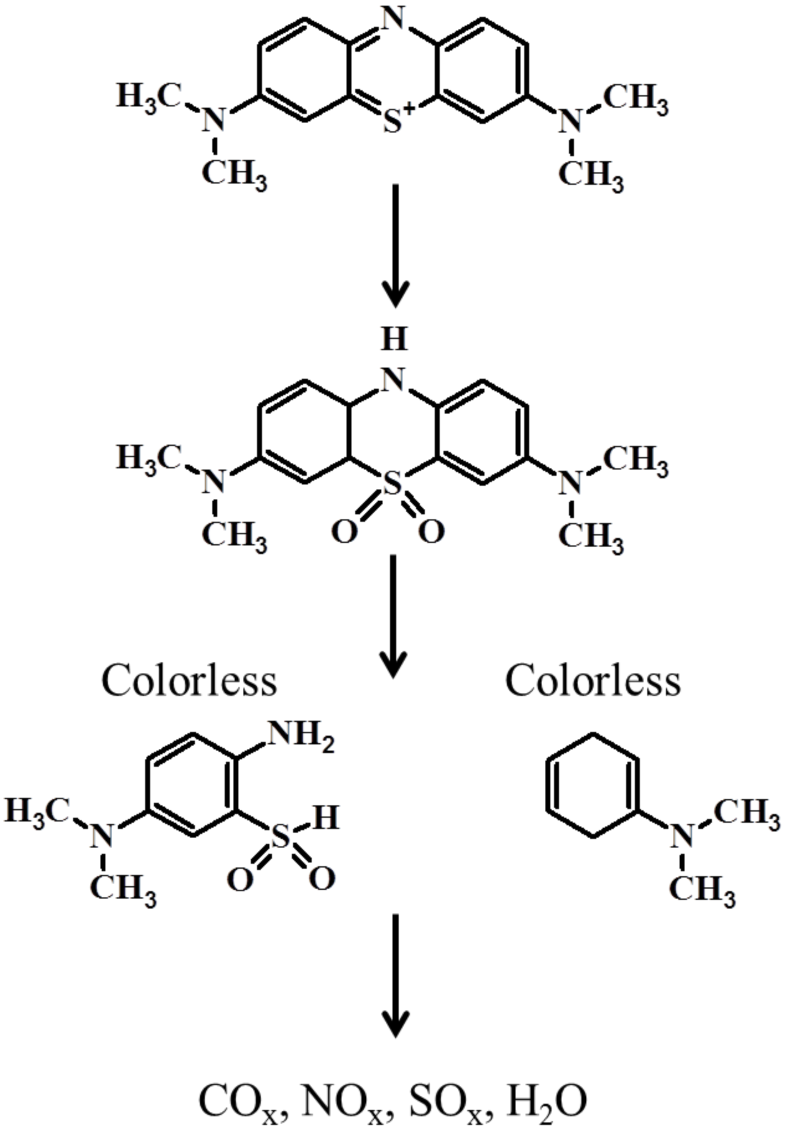

Figure 1.10: Degradation of methylene blue via the ring cleavage pathway; modified from ref. [88]

1.6 Outline of this Dissertation

TiO_2 has been widely studied for a very long time. Despite this, new and interesting properties are being discovered all the time as a result of modifications that are being made to TiO_2. The motivation behind this work was to explore a seemingly overlooked aspect of using TiO_2 as a photocatalysts; determining whether the charge transfer process is affected by the covalent nature of the surface bound species alone and in combination with doping. Molecules bound to TiO_2 by the carboxylate functional group dominated the literature when talking about the potential applications utilizing TiO_2 for its photocatalytic properties. In an attempt to synthesize the most efficient TiO_2 system possible, optimizing the metal-ligand interface would allow us to use and consult with the large body of work already done while also ensuring that we were performing new science. The goal was to answer the charge transfer question while utilizing relatively inexpensive starting materials, room temperature (and pressure) synthesis methods and to avoid generating hazardous waste. By employing room temperature, aqueous based sol-gel synthesis method we were able to meet these goals.

Chapter 2 summarizes the experimental methods by giving a comprehensive list of all instrumentation used in this work. Chapter 3 will discuss the effect of surface modification on TiO_2 phase transition temperature. Chapter 4 will cover the photocatalytic properties of TiO_2 that has been concurrently doped and surface modified. Chapter 5 will review a separate body of work in which Raman spectroscopy can be used to analyze the impact of El Niño on mollusk biomineralization. The remaining chapters will cover ancillary and future works.

CHAPTER 2 –EXPERIMENTAL METHODS

2.1 Introduction

This section will discuss the various instrumental techniques and chemicals utilized throughout this work. The general procedure detailing how TiO_2 particles were synthesized, isolated and collected is also included. Specific reaction conditions for both surface modified and transition metal doped samples will be discussed in detail in subsequent chapters.

2.2 Raman Spectroscopy

Raman spectra were measured using a HORIBA® Jobin Yvon LabRam HR800UV confocal microscope. Data was acquired by an external computer via the software LabSpec®. The excitation source used was a 633 nm Helium Neon (He-Ne) laser with 20 mW power and a 100 μm confocal hole. The solid samples analyzed in this work were placed on a standard disposable borosilicate microscope slide. The analysis of samples was performed in air as no special atmospheric conditions were required. The 50x magnification objective lens was used in this work unless otherwise stated.

2.2.1 Theory of Raman Spectroscopy

Lord Rayleigh in 1871 and Albert Einstein in 1910 were among the first to study the scattering of light by various media. They observed that radiation passing through a transparent medium interacts with atoms or molecules and scatters in all directions with no change in wavelength[91] – a process commonly known as elastic scattering. This idea was the predecessor of Adolf Smekal's theoretical prediction in the early 20th century that a change in frequency results from scattered monochromatic radiation, or inelastic scattering. The physicists C.V. Raman and Krishnan were the first to report the observation of inelastic scattering.[92] This accomplishment earned Raman the Nobel Prize in 1928.[91] When acquiring Raman spectra, a sample is irradiated by powerful monochromatic radiation in the visible or near-infrared region. After interacting with a molecule, the subsequent emitted radiation is classified as Rayleigh scattering or Raman scattering (see figure 2.1). Rayleigh scattering, a form of elastic scattering, is when the scattered radiation has a wavelength that is the same as the incident radiation after interacting with a molecule, and this type of scattering has a much greater intensity than the other class. This process occurs when a molecule is excited from its initial vibrational electronic state to a virtual state and returns to its original state upon relaxation, thus energy is neither gained nor lost. Raman scattering, however, is a form of inelastic scattering that occurs when energy is transferred to a species while interacting with incident photons. This occurs when incident radiation excites a molecule from its original electronic state and upon relaxation it returns to either an electronic energy state that is higher (Stokes) or lower (anti-Stokes) than the original energy state. These transitions are dependent upon the molecule becoming polarized, so the selection rule for Raman spectroscopy states that a Raman active mode can occur only if the polarizability changes during vibration when the sample is irradiated. For molecules containing N number of atoms, there are 3N – 6 normal vibrations (3N – 5 for linear molecules). Of these vibrational modes, some may have vibration at exactly the same frequency. In this case, the modes are called degenerate and only a single feature will be displayed in the spectrum at the respective frequency unless Fermi resonance causes the band to split.

The Raman scattering process occurs much less frequently as the energy difference of this radiation is as much as 10^{-3} to 10^{-5} weaker in intensity than Rayleigh scattering.[9] The relationship of Raman scattering to Rayleigh scattering is the basis on which Raman spectra is viewed. Regardless of the wavelength of the exciting source, the more prevalent Rayleigh scattering is set as the zero position. Because Raman scattering is the magnitude of change in energy absorbed by the molecule with respect to the incident energy upon it, this scattering is referred to as a shift. Figure 2.2 shows the representative spectra of a carbon tetrachloride sample. Both the Stokes and anti-Stokes lines are shifted an equal distance from the Rayleigh line. The anti-Stokes lines are less intense than the Stokes lines because incident radiation encounters molecules that are already in an excited vibrational electronic state far less frequently than molecules that are not. For this reason, the more intense Stokes lines are generally used when reporting Raman spectra.

2.2.2 Raman Calibration

As shown in figure 2.3, both the silicon {100} and the D-band of diamond exhibit a very strong band after a single accumulation (scan) and one second of accumulation time. In this work, a standard silicon wafer was used as the very intense {100} band was centered on the full width at half maximum at ~520.7 cm^{-1}. The silicon wafer used for calibration in this work

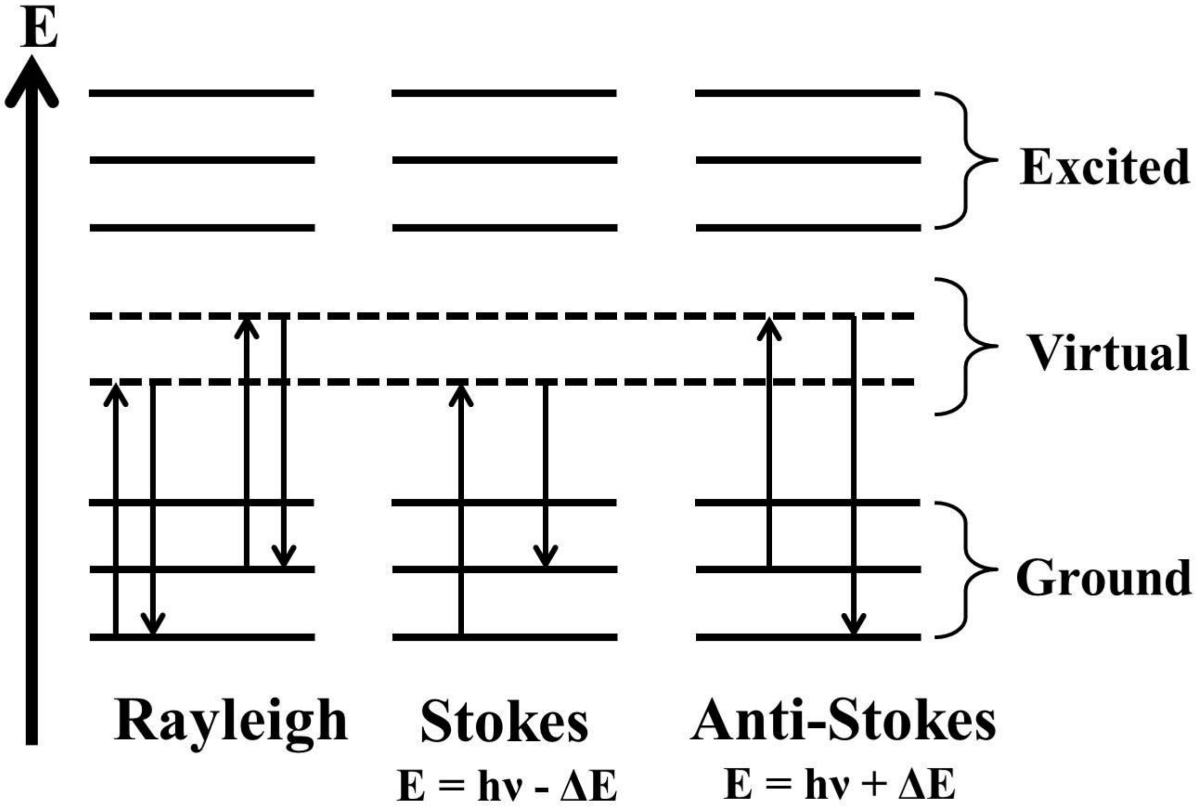

Figure 2.1: Energy level diagram for Rayleigh and Raman transitions (energy levels are not drawn to scale)

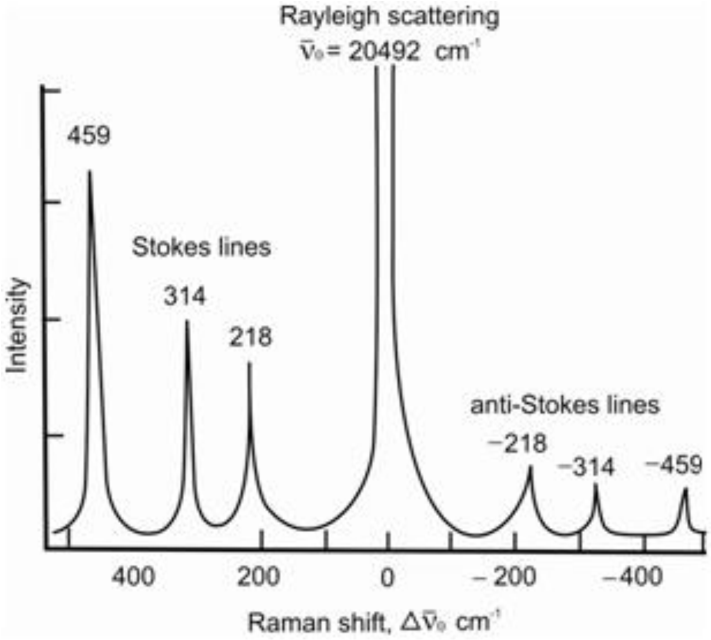

Figure 2.2: Raman spectra of carbon tetrachloride excited by 488nm Ar$^+$ laser; reproduced from ref. [9]

required no special preparation, as a visual inspection is sufficient for determining if any cleaning is required. A silicon wafer or diamond sample can be used for calibration. The peak intensities of these two samples are very sharp, pronounced and well-studied which allows for optimal use as a sample for calibration.

2.2.3 Raman Operation

The Raman spectrometer used in this work is used together as both a light microscope and for Raman analysis. Initially, a sample is placed on a standard disposable borosilicate microscope slide, and then placed on the microscope's stage. No special atmosphere considerations were made, for all samples were air stable. This system has a camera included that allows images to be displayed on the computer monitor as opposed to utilizing the standard objective lens that is normally used on light microscopes. The area of the sample that is located in the focal plane is the area that will be subjected to Raman analysis (see figure 2.4). Using white light (xenon lamp) to illuminate the sample via an optical fiber, the objective lens is used to focus on the sample's region of interest. Once the region of interest is identified, a "black out" curtain is placed over the sample stage to serve as a barrier to prevent fluorescent light from interfering with the sample analysis. At this point, the while light is switched off and the laser beam stops are mechanically removed which allows the beam to irradiate the sample. Both of these functions are controlled by flipping the respective rocker switches located on the control box. When the surface of the sample being analyzed is in the focal plane, the laser beam (visible on the video monitor) will converge to its smallest possible size. The beam spot will be diverged when in both under-focused and over-focused conditions with respect to the surface of the sample being analyzed. At this point, the analysis parameters can be set and the sample is ready to be analyzed.

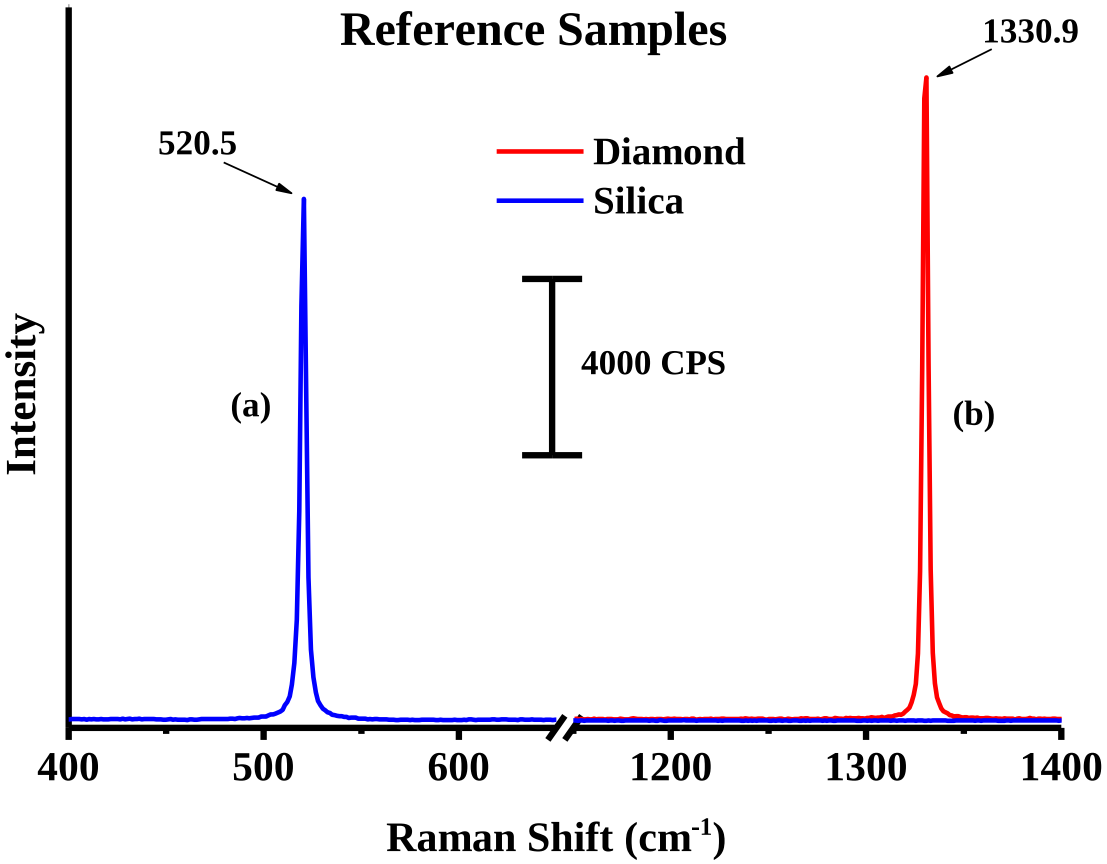

Figure 2.3: Raman spectrum of two samples used to calibrate Raman spectrometers. (a) Silicon wafer with the {100} plane causing the peak at 520 cm^{-1}. (b) The D-mode of single crystal diamond at 1331 cm^{-1}.

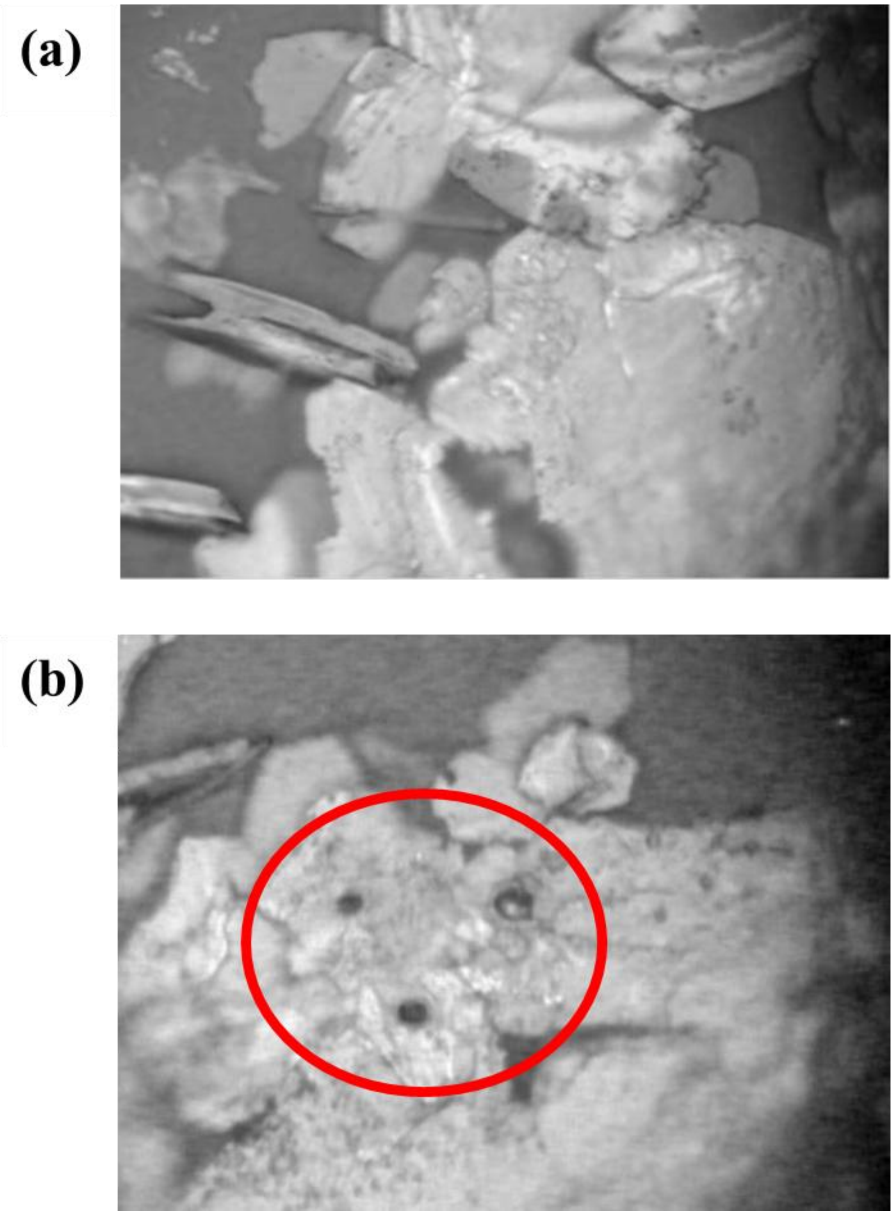

Figure 2.4: Ru(BPY)$_3$ crystals as observed by a Raman microscope via a 10x objective; (a) an example of a single sample of varying height; focusing on a single surface allow for the best analysis; (b) burned sample as a result of the intense laser beam

The spectral region, or region to be analyzed, can be customized by wavenumbers which allows for the analysis of only the desired region(s). The hardware, in its current configuration, limits analysis to the ranges of about 100 cm^{-1} to 4500 cm^{-1}. The number of accumulations, or scans, can be optimized as this controls the averaging out of the designated number of scans. Accumulation, or dwell, times need to be adjusted as they affect signal intensity. Accumulation number and accumulation time are directly proportional to signal-to-noise and peak intensity respectively. Both of these parameters exhibit diminishing returns at some point, so the minimum settings needed to produce a high quality representative spectrum may change as the sample does. When utilizing higher accumulation times, especially when working with organic samples, beam damage to samples can become a problem as shown in figure 2.4. This phenomenon will be noticeable if the real time peak intensities begin to decrease as the number of accumulations increase. A quick visual inspection utilizing the white light can be used to confirm in the event that decreasing peak intensities occur as sample is being analyzed.

2.3 Fourier Transform Infrared Spectroscopy (FTIR)

For this work, two different instruments were used as each utilized different sampling techniques. Both systems were purged with compressed air that was filtered and dried by two desiccant towers. Both systems were connected to the same purging system.

2.3.1 Transmission (FTIR)

Transmission measurements were made with a Nicolet 560 Magna IR spectrometer equipped with a mercury cadmium detector. A clean zinc selenide (ZnSe) window was used as the transmission medium. The window was placed in the purged instrument for approximately

20 minutes to allow for the evacuation of ambient air that entered as the sample chamber was being loaded. After these 20 minutes, a background spectrum was taken. Immediately following, a spectrum of the clean crystal was taken in order to determine if the ambient CO_2 peak was present. After the CO_2 peak is minimized, the ZnSe crystal is removed and a small amount of the powdered sample was placed on the crystal. The crystal was then gently tapped to allow for any large and excess sample to fall off. This method leaves a very fine powder on the crystal that does not prevent acceptable signal to noise. For liquid samples, a very fine layer is spread thin over the crystal after the background of the clean crystal was taken. Two hundred and fifty scans were averaged at a resolution of 4 cm^{-1}.

2.3.2 Diffuse Reflectance (FTIR)

Diffuse Reflectance Infrared Fourier Transform Spectroscopy (DRIFTS) technique was performed with a Bruker Vertex 70 FTIR. A room temperature DLaTGS detector was utilized. Three hundred scans were averaged out as the aperture was set at 6 mm and the scanner velocity was 10 kHz. Data processing was performed via the OPUS software installed on a computer. A Harrick Scientific Praying Mantis® Diffuse Reflection accessory was used for measurements. This techniques utilized spectroscopy grade potassium bromide (KBr) purchased from Fisher Scientific. When not in use, the KBr was placed in a vacuum oven to remain dry. When ready for use, the powder was placed in the provided sampling cup via the provided funnel. After depositing the KBr, a spatula was used to gently smooth off the top of the sample holder. The sample holder containing the KBr was then placed inside the Praying Mantis accessory. This accessory has a much smaller volume to evacuate when compared to the Nicolet FTIR (previous section), so after about 5 minutes a background spectrum was taken. Immediately following its completion, a sample spectrum was taken in order to determine if ambient CO_2 was detectable.

After a minimized peak is observed, the KBr is then emptied onto a piece of weigh paper. A very small amount of powdered sample is then mixed in with the KBr with a clean Pasteur pipette. The filter paper is then folded and used to pour the mixture of analyte and KBr. Once again, any excess powder is gently wiped away with a spatula while being careful not to pack the sample into the sample holder. The sample holder is then placed into the sample chamber. After about 5 minutes, a representative spectrum is obtained.

2.4 X-Ray Diffraction (XRD)

XRD measurements were done on a Bruker D8 Discover with GADDS. This instrument is outfitted with a centric Eulerian cradle and a Hi-STAR area detector. The sample holder consisted of stainless steel well plate. Initially distilled water was used to clean out the well plate. A final cleaning was done with absolute ethanol. The plate was then thoroughly dried with a paper towel. The final step consisted of spraying the well plate with electronic grade dried compressed air from a can (Belkin®).

The powder sample was poured into the well and carefully leveled off with a spatula while being careful as to avoid packing the sample. The power setting for the Cobalt source (Co kα = 1.78897 Ǻ) was 40 kV and 35 mA. Samples were set to continuous rotation and an oscillation pattern in the X and Y directions with an amplitude of 2 mm once analysis began. Sample times varied as the large and more crystalline materials gave excellent peak intensities, while smaller and less crystalline materials gave weaker signals.

For crystalline materials, the average crystallite sizes were estimated using the Scherrer equation.[93] In this equation, ϕ is the size of the crystallite in nanometers, K is a shape factor, λ is the wavelength of the x-ray in nm (0.178897 Co kα), β is the full width at half maximum of the

$$\phi = \frac{K\lambda}{\beta \cos(\theta)} \tag{2.1}$$

peak in radians and θ is the peak position Because the technique is based on the constructive interference of x-rays as they interact with planes of atoms, nanoparticles expose a bit of a limitation to this technique as the smaller particle sizes present smaller planes of atoms. The smaller planes of atoms decrease the amount of constructive interference which in turn decreases the sensitivity of this technique. When utilizing XRD, crystallographers attribute peak broadening to disorder, or a loss of long distance translational periodicity, in the structure of a material.[94] Though there are other material properties that can cause peak broadening, a uniform broadening of all peaks in the spectrum are generally indicative of smaller particle sizes.

Although XRD has long been deemed the standard when determining the phase and average particle size of crystalline materials,[95] in some cases the aforementioned Raman spectroscopy can be more beneficial for determining these two parameters. Whereas XRD requires long range periodicity, only librational and lattice Raman modes are sensitive to long range periodicity. The widths of the remaining Raman modes are sensitive to the short range order of the first (~ 0.1 nm - 0.5 nm) and second (~ 0.5 nm - 5 nm) atomic shells with bending and stretching modes being specifically sensitive to local geometric disorientation and neighboring disorder respectively.[96]

2.5 Ultraviolet-Visible Spectroscopy (UV-Vis)

Electron absorption spectra were measured with a Varian Cary 50 UV-vis spectrophotometer. Solutions containing the respective analyte(s) were placed in a 1 cm path

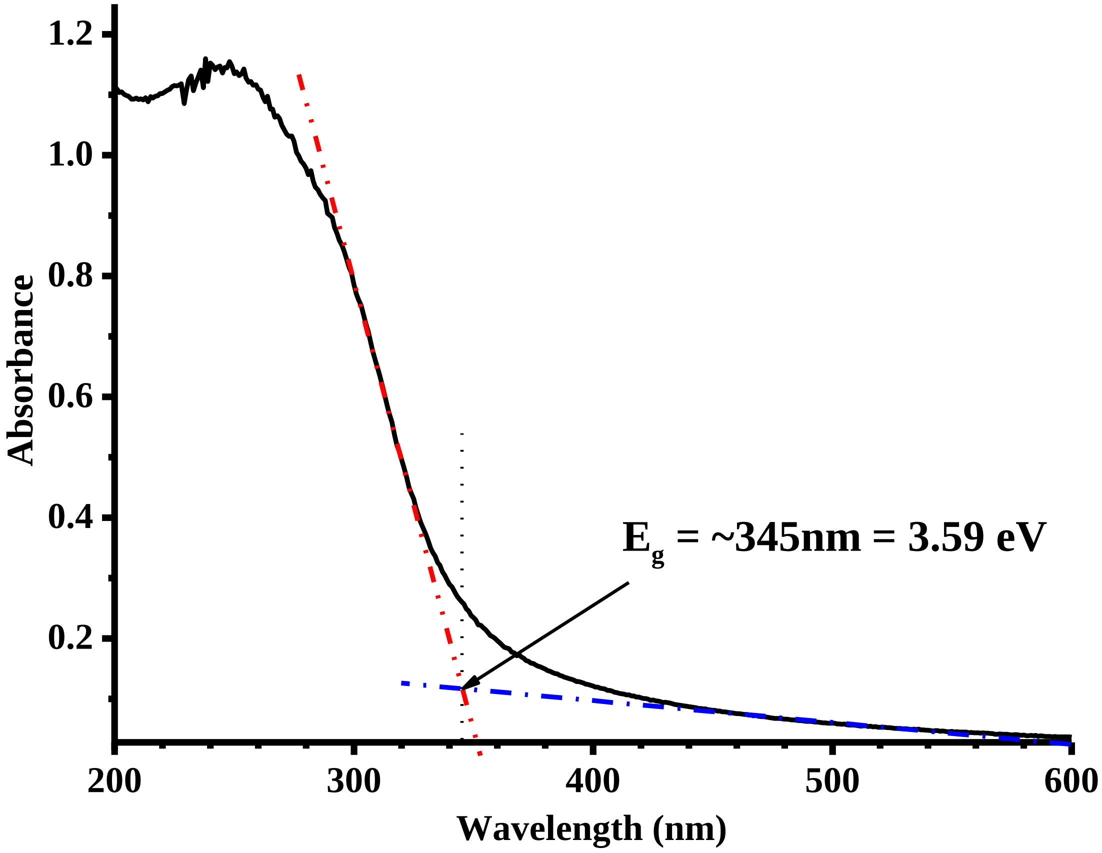

Figure 2.5: UV-Vis spectrum showing the experimentally determined band gap (E_g)

length quartz cuvette at room temperature. Scan rates were set at 600 nm/min. Bandgap information is obtained from the representative spectrum by extrapolation of the flat line of the low nanometer end and extrapolation of the absorption edge.[97] The wavelength at which these lines intersect is the experimentally determined band gap.[98]

2.6 X-Ray Photoelectron Spectroscopy (XPS)

XPS analysis was performed using a Kratos Axis 165 x-ray photoelectron spectrometer. The base pressure of the system was 2.0 x 10^{-9} torr, and Aluminum kα monochromatic x-ray (1486.7 eV) was the x-ray source used. It operated at 150 W (15 kV at 10mA) and the spectra were collected with a pass energy of 40 eV.

The samples were embedded onto double sided carbon tape with no further preparations. Because the photoemission process (figure 2.6) can cause localized charging, charge neutralization may be required. Sample charging is problematic because it can lead to peak broadening and diminished reliability of the acquired data. When non-monochromatic x-ray sources are used, there are usually a suitable number of low energy electrons (usually less than 5 eV) available in the sample to promote neutralization. The use of monochromatic x-rays for excitation usually requires charge neutralization because the number of low energy electrons is not produced in sufficient quantities to achieve neutralization.[99] In this case, a filament is used to flood the sample with low energy electrons that produce a uniform negative charge of known magnitude across the surface of the sample. After charge neutralization and data acquisition, the peaks are shifted to their correct position by using the adventitious carbon (1s) peak that resides at a binding energy of approximately 284.5 eV as the standard.

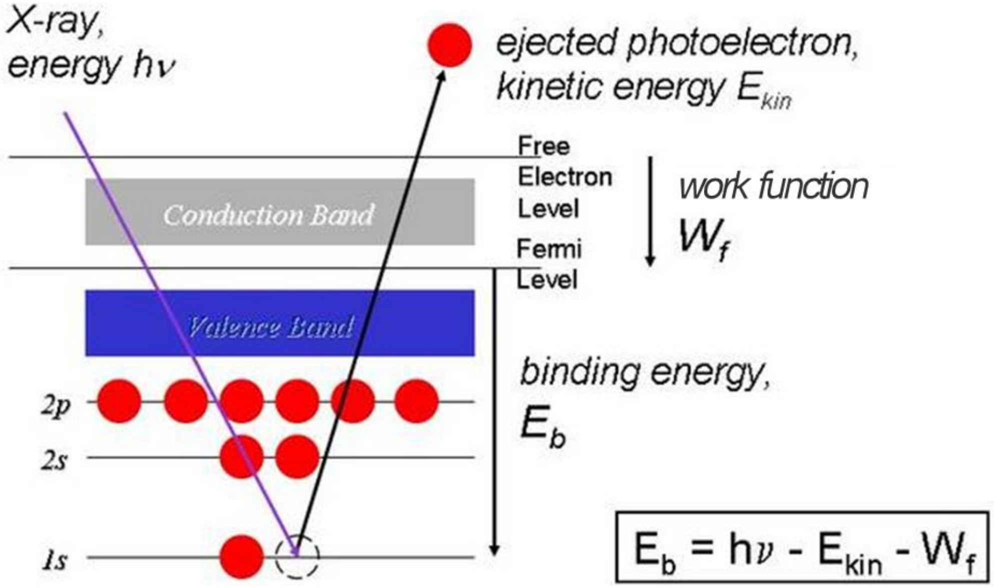

Figure 2.6: Cartoon of the X-Ray photoelectron process. Image adapted from ref [99]

2.7 Tube Furnace

Samples were annealed using a Lindberg/Blue 1100 °C Three Zone Tube Furnace. The furnace was outfitted with a 3-inch diameter quartz tube. The samples were placed in a ceramic boat and/or well plate and placed in the center zone of the furnace where it was heated for the respective heating cycle. The samples were annealed in air with a ventilation snorkel near the open end to remove any liberated gases. The heating rate was 25 °C/min and the samples were allowed to cool naturally.

2.8 Photochemical Reaction Chamber

Irradiation of samples was performed with a Rayonet photochemical reactor (RPR-600 model, Southern New England Ultraviolet inc., Branford CT). The reactor was equipped with a cooling fan as well as a rotating sample holder that can accommodate up to 8 samples. The reactor employed 5 fixed UV lamps (λ_{max} = 254 nm) that produced 8 W per lamp. The spatial energy distribution of this source can be seen in figure 2.7. The irradiated samples were uniformly irradiated due to the 5 RPM rotating sample holder. The solutions were irradiated in quartz test tubes for the required amount of time under ambient conditions. The quartz test tubes utilized were designed and fabricated in house to fit into the photochemical reaction chamber.

2.9 TiO_2 Synthesis

All TiO_2 samples used in this work were prepared via the sol-gel method (see §1.4.2). Although there were variations in the reactants used, the general reaction from initialization to collection of the final product followed the same general procedure. This aqueous based reaction

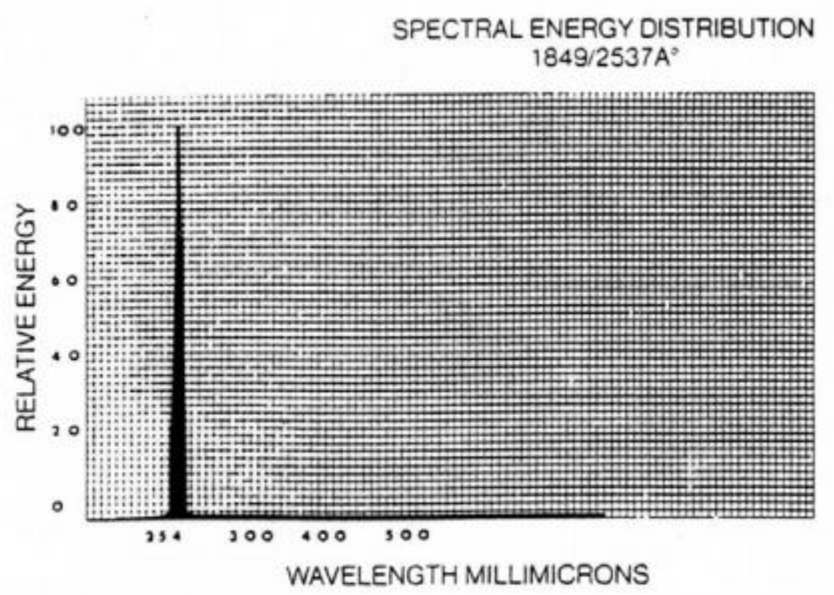

Figure 2.7: Spectral energy distribution of 254 nm (~ 8 W per lap) lamps from Rayonet specification. Reproduced from ref [296]

utilized fairly low cost reagents, avoided the use of dangerous chemicals and produced very few toxic waste products. Specific reaction conditions for both surface modified and transition metal doped samples will be discussed in detail in subsequent chapters.

2.9.1 Chemicals

All chemicals utilized in this work were used as received. Synthetic reactions involved in the formation and the surface modification TiO_2 utilized the following chemicals: titanium (IV) isopropoxide (97%), propionic acid (99.5%), and boric acid (99.5%) were all purchased from Sigma-Aldrich. Sulfuric acid (Certified ACS Grade - Fisher), phosphoric acid (85% - EM Science), 3-aminopropyl triethoxysilane (95% - Gelest), isopropyl alcohol (ACS Grade) and deionized water were also used in this work. Reagents used in the doping of TiO_2 included cobaltous chloride hexahydrate (98%), vanadyl acetylacetonate (98%) and cupric chloride dihydrate (laboratory grade). The cobalt and vanadium complexes were purchased from Sigma-Aldrich, whereas the copper compound was purchased from Fisher Scientific.

2.9.2 Washing Procedure

All TiO_2 synthesis reactions were considered complete after stirring for 2 hours, the reaction mixture was emptied directly into 15 mL centrifuge tubes, capped and centrifuged at ~2000 rpm for several minutes. After this first centrifugation step, the supernatant was discarded and DI water was added until the tube was partially filled. At this point, the partially filled tube was capped, shaken and ultrasonicated in order to disperse the precipitate in the water in an attempt to dissolve any unwanted species that may have been either physisorbed or trapped in the pores of the gel formed during the reaction. The unwanted species included isopropanol, a byproduct of the titanium precursor used, as well as the respective surface modifying species.

After the sonication step, DI water was added until the tube was filled. The sample was then sonicated again before being placed into the centrifuge. This procedure was repeated for a minimum of 5 cycles as all samples were determined to be clean after the fifth washing cycle.

Surface modification used oxyacids. Upon completion of the each centrifugation step the pH of the supernatant was tested with a piece of pH paper. The particles were considered clean when the pH of the supernatant reached a neutral (~7) pH. If the pH of the supernatant was not neutral, the liquid was discarded and the addition of DI water began a new wash cycle. In other work (Chapter 4), transition metal doped samples were prepared using transition metal salt precursors. These salts caused the reaction mixtures to be colored. The samples were considered clean when the supernatant was clear upon visual inspection. If the supernatant retained a color after centrifugation, the wash cycle was repeated.

2.9.3 Filtration and Processing

Once washing was complete, the samples were collected by vacuum filtration. The centrifuge tubes were emptied into a Buchner funnel containing two sheets of Whatman® filter paper. This funnel was used in conjunction with a side-arm Erlenmeyer flask that was connected to the house vacuum line. When only one piece of filter paper was used, the milky solution simply passed through without retaining any of the solid. The second piece of filter paper slows the process considerably but traps the solid and allows for the clear filtrate to pass through. After all the visible liquid had passed through the filter, the vacuum line was left on for a few extra minutes. (Though this step is not required, the extra time allows for the fast moving air to dry the cake enough to form cracks as well as separate the cake from the dry filter paper as it too is dried). The resulting cake was placed in a mortar and the dry filter paper is easily separated from the sample. A pestle was used to press the cake thin in order to ensure a more thorough drying and the sample was placed in a vacuum oven at 40 °C for several hours. A low vacuum was turned on in order to remove the residual water vapor from the chamber as it dried out of the sample. The sample was ground using the pestle every couple of hours until the powder was dry and had a very fine consistency.

2.9.4 Drying and Collection

After about 18 hours at 40 °C, the powder was transferred from the mortar into a screw-cap vial via filter paper or a weigh boat. The samples were then sufficiently dried and ready for analysis. The drying oven was set at this relatively low temperature because higher temperatures and/or longer drying times have been shown to induce crystallization from the amorphous to anatase phase.[31, 100, 101] The particles, as prepared, were then analyzed to determine crystallographic phase. Once the phase was determined samples were annealed to induce crystallization.

CHAPTER 3 – EFFECT OF SURFACE MODIFICATION ON TiO_2 PHASE TRANSITION TEMPERATURE

3.1 Introduction

Anatase, brookite and rutile are the three common polymorphs of TiO_2. Although they all contain the TiO_6 octahedra, the subtle differences in structure contribute to different material properties. Of the three TiO_2 polymorphs, rutile is the most thermodynamically stable phase at room temperature. The other two phases, anatase and brookite, can be irreversibly driven to the rutile phase by exposing to high temperatures.[31, 49, 100-103] The temperatures at which these transitions occur are known as the phase transition temperature (PTT). However, there are several factors that can affect the kinetics that control the amorphous to anatase transition (α-A) transition and the anatase to rutile (A-R) transition.

It has been shown in previous works that the synthesis of TiO_2 via the sol-gel method produces amorphous particles.[104-106] However, a variety of polymorphs can be produced if the reaction parameters (pH, temperature, aging time, addition rates, etc.) are modified.[100, 102, 106-109] Once synthesized, the resulting size, shape, surface area, impurity content and heating rate can affect the subsequent PTT if the desired polymorph is not already achieved.[51, 110-114] This concept is important because some applications, such as porous gas separation membranes and gas sensors, endure harsh conditions that can induce phase transition and as a result decrease the performance of the devices.[115-117]

Single-crystalline TiO_2 is among the most studied systems in the surface science of metal oxides.[27] Among these studies is a body of work that deals specifically with the surface modification of single crystal TiO_2.[70, 118-123] These single crystal studies would be the theoretical basis for making modifications to bulk TiO_2 surfaces. Various oxoacids have been used as models to demonstrate the ability of TiO_2 to accept chemisorption at its surface. Successful surface modification of TiO_2 has been achieved by attaching sulfates,[83, 124, 125] phosphates,[47, 126, 127] silicates,[128-130] and carboxylates[131-133] functional groups. Although these oxoacids are small and simple molecules, they are capable of serving as coupling agents that facilitate binding of much larger and complex molecules to TiO_2 surfaces (§1.4.4).

In this work the reaction conditions utilized lead to the formation of amorphous TiO_2 nanoparticles as prepared. Common oxyacids are included in the reaction mixture and attached to the surface of the amorphous TiO_2 particles. After drying and collecting, the samples are systematically annealed to induce crystallization. The effect of surface modification on phase transition temperature is then determined by comparing the observed values to the literature values of pristine TiO_2.

3.2 Nanoparticle Synthesis

All TiO_2 samples were prepared by the controlled hydrolysis of titanium(IV) isopropoxide (Ti-O*i*Pr) under ambient conditions as previously shown by Korosi.[134] In a 500 mL Erlenmeyer flask, 14.8 mL of Ti-O*i*Pr was diluted with 30 mL of isopropyl alcohol (IPA). The solution was magnetically stirred using a Teflon coated magnetic stir bar. To this mixture, 50 mL of deionized (DI) water was added promoting hydrolysis. After this hydrolysis process, surface modification was effected by adding 200 mL of the respective 0.05M solution to the reaction mixture. The solutions used to attempt surface modification contained phosphoric acid, boric acid, (3-aminopropyl)triethoxysilane (APTES), propionic acid and sulfuric acid. Unmodified, or pure, TiO_2 was prepared similarly as 200 mL of DI water was added instead of a 200 mL solution containing a surface modifying species (SMS). The samples were allowed to stir for 2 hours at room temperature before collecting (as outlined in §2.9).

3.3 TiO_2 Surface Modification

For surface modification, the reaction conditions were carried out in a way that produced TiO_2 particles prior to the addition of the SMS. After initial TiO_2 formation, surface modification was attempted by adding the respective species (figure 3.1) to each reaction. TiO_2 synthesis conditions were held constant and a common concentration of 0.05M of the SMS was used for each reaction. The reaction was performed as described in the previous section to promote surface bonding instead of "trapping" the SMS in the inorganic network as the alkoxide hydrolysis and polymerization reactions occur which lead to particle formation.

When introduced to the reaction mixture, the SMS shown in figure 3.1 dissociate and form ions in solution. As the protons dissociate, the resulting anions are available for bonding with exposed Ti^+ surface sites of TiO_2. The silicate species has the ethoxy groups replaced by hydroxide groups when it initially hydrolyzes as its 0.05M solution is prepared.[135, 136] When the surface modification process was complete, the samples were analyzed for the presence of the SMS. Samples identified as "as prepared" describe samples that were analyzed prior to high temperature annealing. Individual samples were identified based on the SMS utilized during the reaction: unmodified (pure); phosphate (P-mod); carboxylate (C-mod); silicate (Si-mod); borate (B-mod); sulfate (S-mod).

3.3.1 FTIR Analysis

After the synthetic procedures were completed, diffuse reflectance infrared Fourier transform spectroscopy (DRIFTS) analysis was performed to identify the functional groups present via their characteristic vibrational frequencies. Figure 3.2 shows the FTIR spectra of the various powder samples. A more detailed view of all FTIR spectra can be found in the appendix.

Within the graph, spectrum (a) shows pure-TiO_2. The FTIR spectrum of pure TiO_2 consist of a broad feature at the low wavenumber region ~500 cm^{-1} – 900 cm^{-1} that is attributed to Ti─O─Ti lattice vibrations.[47, 137] The peak at 1627 cm^{-1} is due to the O─H bending mode of water and/or surface hydroxides. The high wavenumber features, the broad ~3200 cm^{-1} – 3400 cm^{-1} and 3666 cm^{-1}, represent hydrogen bonding and O─H stretching from surface absorbed water and hydroxide groups respectively.[138] All samples exhibited the general structure of this spectrum which was indicative of TiO_2 being present as the substrate in all the samples. Four of the five SMS were confirmed to be present after the surface modification procedure was carried out (see table 3.1). As these modifications occur, the SMS are bound to the TiO_2 substrate in a specific orientation and a representation of the possible modes of coordination can be seen in figure 3.3. The lone unsuccessful SMS, the borate species labeled as spectrum (b), showed no indication of being present as its spectrum looked virtually identical to the pure TiO_2 spectrum.

The carboxylate species, shown in spectrum (c), is identified by several different features. The ─CH_2─ wag and deformation modes are identified by peaks at 1302 cm^{-1} and 1471 cm^{-1}

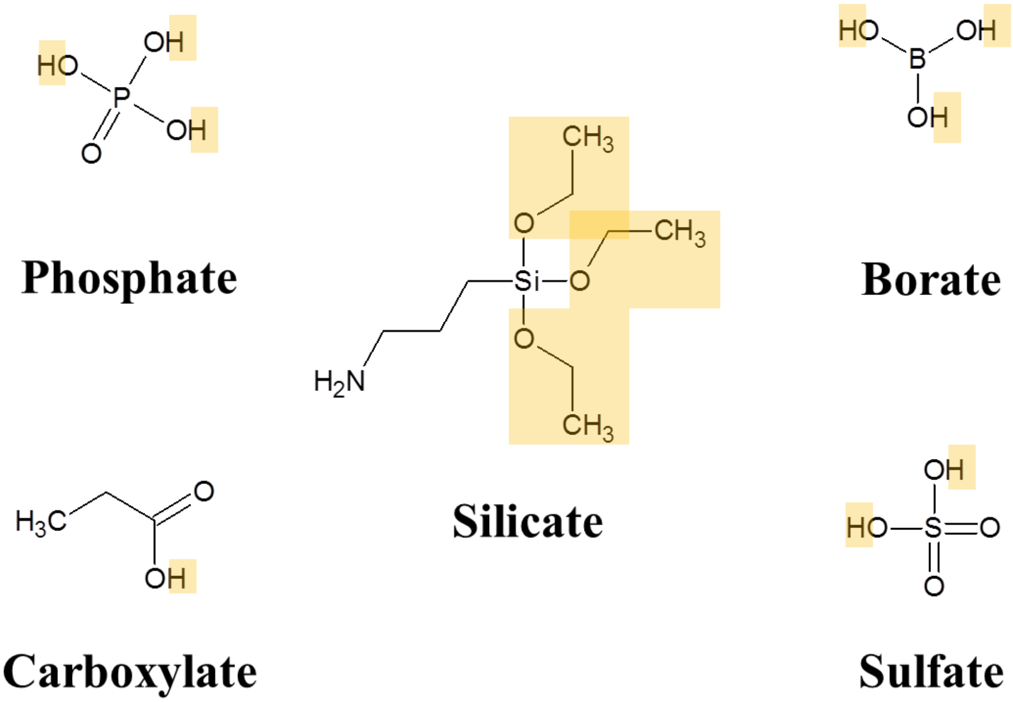

Figure 3.1: Simple molecules used to bond to the surface of TiO_2 nanoparticles. When introduced to the reaction mixture, the highlighted portions dissociate and a potential binding site is exposed. The nomenclature shown is indicative of the functional group involved in TiO_2 surface bonding and is not the actual molecule shown.

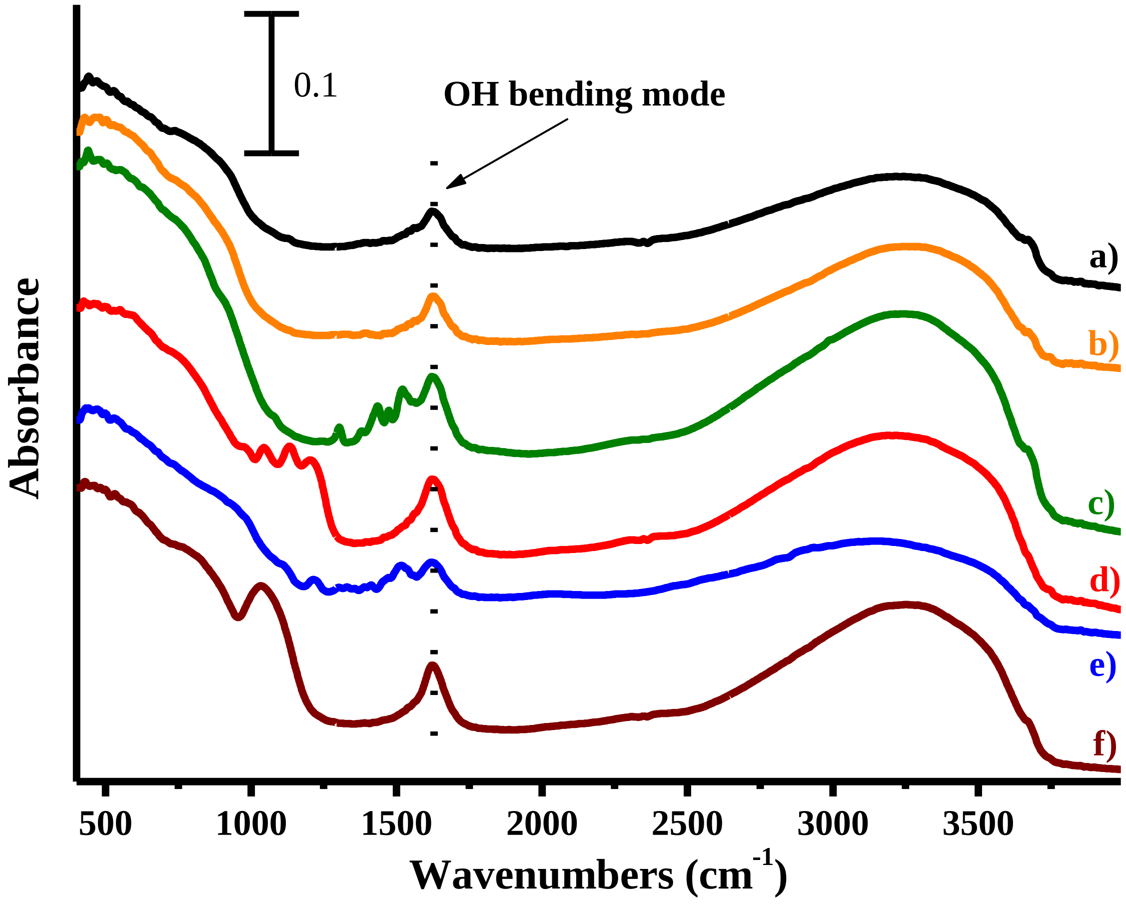

Figure 3.2: FTIR analysis of as prepared-TiO_2 after surface modifications were performed: a) pure; b) B-mod; c) C-mod; d) S-mod; e) Si-mod; f) P-mod. All spectra were vertically adjusted for clarity.

respectively.[139] The feature at 1379 cm^{-1} is the symmetric deformation of $-CH_3$.[140] The symmetric and asymmetric stretching modes of the carboxylate ($-COO^-$) are positioned at 1435 cm^{-1} and 1521 cm^{-1} respectively.[141] The relatively low Δ value, or the difference in wavenumbers between the symmetric and asymmetric stretching modes, indicates that the carboxylate is bound to the surface of the TiO_2 substrate in a bidentate fashion.[141]

The sulfate species, shown in spectrum (d), is identified by the four rather distinct features. The free sulfate is categorized in the T_d point group. This high-symmetry point group has four fundamental modes of which only two are infrared active, ν_3 and ν_4. When the sulfate species forms a complex by bonding to a metal, the symmetry is lowered and all four fundamental modes can become infrared active depending on the type of coordination to the metal. The four features observed in this work were 978 cm^{-1}, 1043 cm^{-1}, 1131 cm^{-1} and 1203 cm^{-1} correspond to the ν_1 and ν_3 (degenerate splitting) modes that correspond to symmetric and asymmetric stretching modes respectively.[141-143] The method of sulfate binding to the surface of the TiO_2 substrate is apparently bidentate because of the higher frequencies of the binding modes when compared to unidentate and bridging sulfato complexes found in literature.[141, 144]

The silicate species, shown in spectrum (e), also contained carbonaceous species that caused several features in the corresponding region of interest. The peaks at 1103 cm^{-1} is due to the Si—O symmetric stretch, 1214 cm^{-1} the $Si-CH_2$ wag, 1302 cm^{-1} the $-CH_2-$ wag, 1329 cm^{-1} the Si—CH scissoring, 1354 cm^{-1} the C—H deformation, and 1389 cm^{-1} the $-CH_3$ symmetric deformation. The peak found at 1411 cm^{-1} is the $Si-CH_2-$ deformation mode. The shoulder feature at 1471 cm^{-1} can be attributed to the deformation of the central $-CH_2-$ of the propyl chain found in the APTES ligand. The larger peaks located at 1515 cm^{-1} and 1620 cm^{-1} are

Sample	Wavenumbers (cm^{-1})	Vibrational Modes
(a) Pure TiO$_2$	500 cm^{-1} – 900 cm^{-1}	Ti─O─Ti lattice vibrations [47, 137]
	1627 cm^{-1}	O─H bending mode [47]
	3200 cm^{-1} – 3400 cm^{-1}	H bonding, surface adsorbed water [138]
	3665 cm^{-1}	Ti─O─H stretch [137]
(c) C-Mod TiO$_2$	1302 cm^{-1}	─CH$_2$─ wag [139]
	1379 cm^{-1}	─CH$_3$ symmetric deformation [140]
	1435 cm^{-1}	─COO$^-$ symmetric stretch [141]
	1471 cm^{-1}	─CH$_2$─ deformation [139]
	1521 cm^{-1}	─COO$^-$ asymmetric stretch [141]
(d) S-Mod TiO$_2$	978 cm^{-1}	ν_1 M─SO$_4$ symmetric stretch [141, 143, 145]
	1043 cm^{-1}	ν_3 M─SO$_4$ asymmetric stretch [141, 143, 145]
	1131 cm^{-1}	ν_3 M─SO$_4$ asymmetric stretch [141, 143, 145]
	1203 cm^{-1}	ν_3 M─SO$_4$ asymmetric stretch [141, 143, 145]
(e) Si-Mod TiO$_2$	1103 cm^{-1}	Si─O symmetric stretch [139, 140]
	1214 cm^{-1}	Si─CH$_2$─ wag [139, 140]
	1302 cm^{-1}	─CH$_2$─ wag [135, 140]
	1329 cm^{-1}	Si─CH scissoring [146]
	1354 cm^{-1}	C─H deformation [139, 140]
	1389 cm^{-1}	─CH$_3$ symmetric deformation [135, 139, 146]
	1411 cm^{-1}	Si─CH$_2$─ deformation [135, 139, 146]
	1471 cm^{-1}	─CH$_2$─ deformation [139, 140]
	1515 cm^{-1}	─NH$_3^+$ deformation [139]
	~1620 cm^{-1}	N─H bend [135, 139]
(f) P-Mod TiO$_2$	~1035 cm^{-1}	M─PO$_4$ [47, 140]

Table 3.1: Observed FTIR vibrational modes and their respective characterization of surface modifications performed on TiO$_2$ substrate shown in figure 3.2.

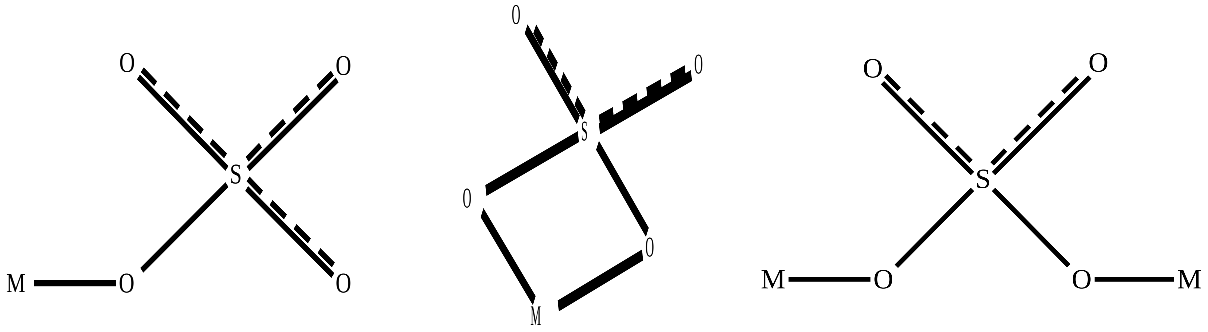

Unidentate

Bidentate

Bridged Bidentate

Figure 3.3: Possible modes of coordination of ligands bound to metal surfaces; modified from ref [141]

assigned to the ─NH_3^+ deformation and N─H bending respectively.[47, 139, 140, 146, 147] The ─NH_3^+ arises as the terminal amine groups are protonated by residual water (~1630 cm^{-1}) that remains present on the surface of the TiO_2 substrate after the low temperature drying step. Prior studies have shown that the silicate species is bound to the surface of single crystal TiO_2 (100) in a bidentate fashion with an unbound hydroxyl and an amine terminated propyl chain.[129, 148]

The phosphate species, shown in spectrum (f), has a lone broad feature centered at ~1035 cm-1. This broad feature (~950 cm^{-1} – 1110 cm^{-1}) is indicative of the PO_4 characteristic vibrational frequencies. It has been shown in previous studies that a broad feature results from highly acidic conditions.[149, 150] As the synthetic conditions become more basic, the four overlapping features (symmetric and asymmetric P─O; symmetric and asymmetric P─OH) become more pronounced within the spectrum.[127] As is the case with many tetrahedral anions such as the free sulfate ion, the free phosphate ion has T_d symmetry that is lowered to either C_{2v} or C_{3v} upon coordination. The phosphate ion binds the TiO_2 substrate in a bidentate fashion indicates C_{2v} symmetry.[127, 141]

3.3.2 XPS Analysis

XPS analysis was performed for further verification of successful surface modification. Figure 3.4 shows the low binding energy region of the spectra for all samples except C-mod TiO_2. The observed electronic transition and their respective characterizations are shown in table 3.2. Peak fitting was utilized when high resolution scans revealed peaks possessing shoulders and/or irregular shapes. A more detailed view of all XPS spectra can be found in the appendix.

Within the graph, spectrum (a) shows pure TiO_2. The main feature at 284.5 eV is attributed to the adventitious carbon as the C-1s peak. The minor peaks found in the same region, 286.5 eV and 288.5 eV, are likely contributions from alcohol and carbonyl containments.[151, 152] The remaining features found at 61.5 eV, 36.5 eV and 21.5 eV are identified as Ti-3s, Ti-3p and O-2s respectively. These three low binding energy features warrant no further mentioning as they are remained relatively unchanged among all samples. The high binding energy features include peaks at 458.1 eV (Ti-2p$_{3/2}$), 463.8 eV (Ti-2p$_{1/2}$) and 564.3 eV (Ti-2s); all of which are consistent with TiO_2.[153-155] The O-1s peaks are found at 529.2 eV (TiO_2), 531.5 eV (TiOH) and 533.1 eV (basic hydroxyl groups or chemisorbed water).[151, 152, 156-158] The binding energies seen in the sample are in good general agreement with the samples in which surface modification was attempted.

Spectrum (b) of figure 3.4 shows the spectrum of B-mod TiO_2. The line profile resembles pure-TiO_2 very closely with the exception of a peak at 400.3 eV which Sargent et al. attributes to trace amounts of N_2 absorbed on the TiO_2 surface.[153] The B-1s feature would be expected at ~188 eV,[25] yet a high resolution scan of this region yielded no evidence of boron being present. With both XPS and FTIR exhibiting no spectroscopic proof of boron present, it was concluded that the attachment of borate to the surface of TiO_2 was unsuccessful.

Line spectrum (c) of figure 3.4 shows the spectrum of S-mod TiO_2. The C-1s peak at 284.3 eV was used as the internal standard for the sample. Sulfur was shown to be present in the sample by the appearance of the S-2s feature located at 233.4 eV. The S-2p peak at 169.3 eV is indicative of the sulfate ion being present as this binding energy is typically that of sulfur that exists in the S^{VI} oxidation state.[159-161] Also, there is a O-1s peak at 532.8 eV that corresponds to that of sulfates.[155]

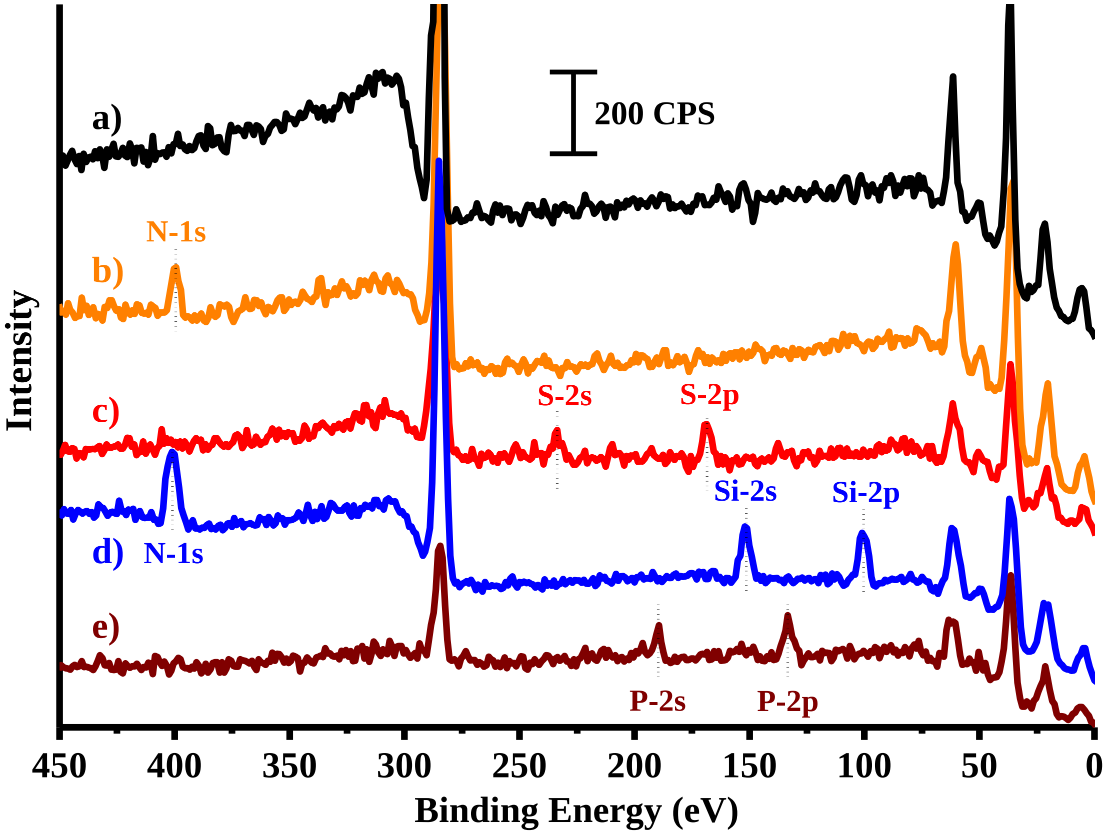

Figure 3.4: XPS analysis of as prepared-TiO_2 after surface modifications were performed: a) pure; b) B-Mod; c) S-Mod; d) Si-Mod; e) P-Mod. All spectra were vertically adjusted for clarity.

	Binding Energy (eV)				
Assignment	**Pure $\mathrm{TiO_2}$**	**B-mod $\mathrm{TiO_2}$**	**S-mod $\mathrm{TiO_2}$**	**P-mod $\mathrm{TiO_2}$**	**Si-mod $\mathrm{TiO_2}$**
O - 2s	21.5	21.5	20.6	21.4	21.0
Ti - 3p$_{3/2}$	36.5	36.3	36.6	36.4	36.5
Ti - 3s	61.5	61.3	61.6	61.4	61.5
C - 1s	284.5, 286.5, 288.5	284.6	284.3, 286.6	284.4, 286.3	284.5, 286.8
Ti - 2p$_{3/2}$	458.1	458.2	458.9, 461.3	457.5, 459.2	457.5, 461.4
Ti - 2p$_{1/2}$	463.8	464.0	464.3, 466.9	460.8, 465.0	463.2, 467.1
O - 1s	529.2, 531.5, 533.1	528.8, 530.0	530.6, 532.8, 534.4	530.5, 531.9	528.6, 532.2, 533.8
Ti - 2s	564.3	563.3	567.5	566.4	567.0
N - 1s	▨	400.3	▨	▨	398.7, 401.3, 403.9
Si-2p	▨	▨	▨	▨	100.8, 103.0
Si-2s	▨	▨	▨	▨	152.5
S-2p	▨	▨	169.3	▨	▨
S-2s	▨	▨	233.4	▨	▨
P-2p	▨	▨	▨	133.2	▨
P-2s	▨	▨	▨	190.6	▨

Table 3.2: Observed XPS transitions and their respective binding energies

Line spectrum (d) of figure 3.4 represents Si-mod TiO_2. The C-1s contains two features. The peak at 284.5 eV is assigned to adventitious carbon and the 286.8 eV peak is attributed to alcohols.[151, 152] There are three N-1s peaks (398.7 eV, 401.3 eV and 403.9 eV) that correspond to NH_2, NH_3^+ and oxidized nitrogen due to surface contaminants.[162-164] As the surface modification procedure utilizes the sol-gel method, residual water that was not completely removed by the drying process interacts with the amine group of the APTES causing the NH_3^+ to be present. Silicon is shown to be present at 152.5 eV (Si-2s) and 101.6 eV (Si-2p). It has been reported in other works that the APTES (see figure 3.1) ligand can bind to the surface hydroxyl groups of metal oxides by either the silicon end or by the terminal amine group.[128, 165, 166] The two silicon features as well as the O-1s feature at 532.2 eV, which corresponds to the Ti─O─Si,[153] confirms surface bonding to TiO_2 via the silane group.[154, 167] It is from this data that the APTES is confirmed to be present as well as its mode of coordination.

The line spectrum (e) of figure 4.4 is that of P-mod TiO_2. Adventitious carbon, the C-1s feature, has a binding energy of 284.4 eV. Phosphorus is determined to be present by the appearance of the P-2s mode at 190.6 eV and the P-2p mode at 133.2 eV.[152] The presence of the O-1s feature at 531.9 eV corresponds to the binding energy of surface hydroxyl groups.[155] Further evidence of the phosphate ion is shown at 530.6 eV which is attributed to the P─O bond.[69]

3.4 Phase Identification

Raman spectroscopy has proven to be a very powerful tool when analyzing nanoparticles. Not only do the three common polymorphs of TiO_2 have a unique representative spectra, amorphous TiO_2 does as well. Figure 3.5 shows the spectra of amorphous, anatase, rutile and a

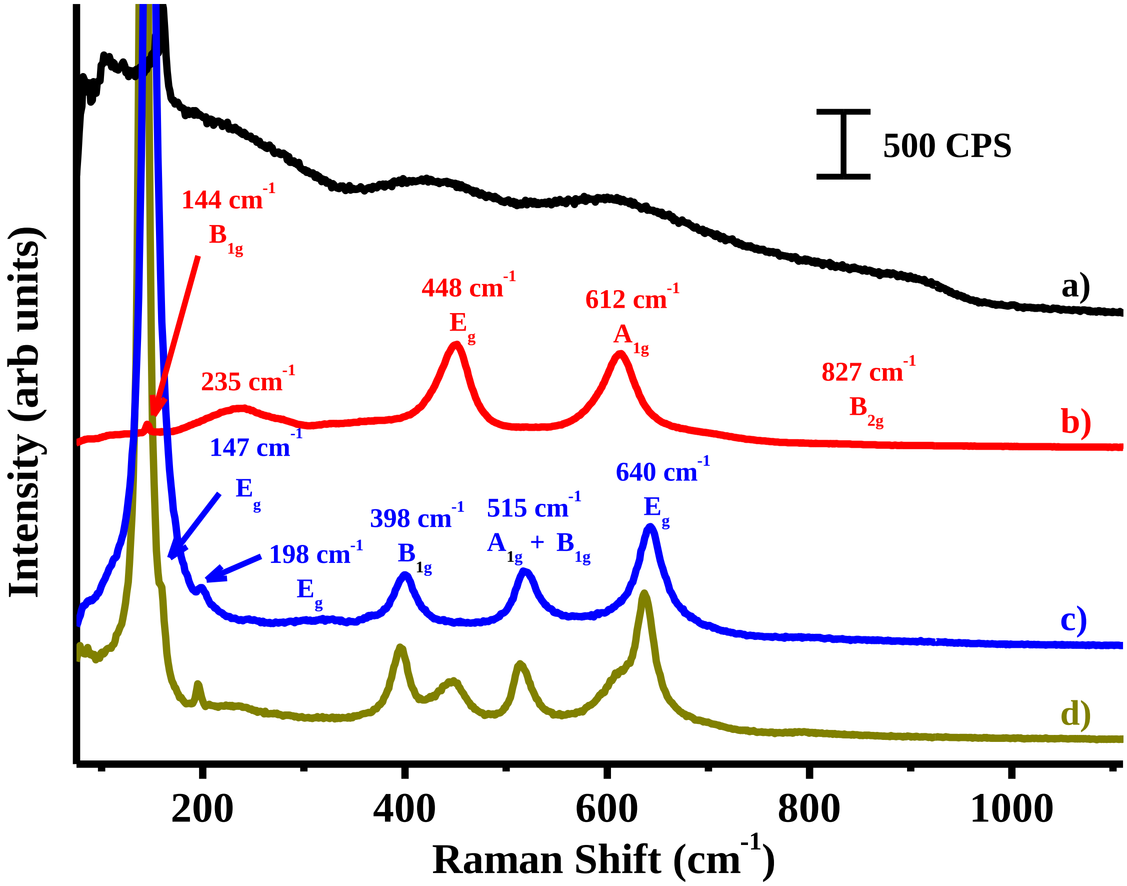

Figure 3.5: Raman spectra of TiO_2 samples: a) amorphous; b) rutile; c) anatase; d) rutile/anatase mixture. Spectra have been vertically adjusted for clarity.

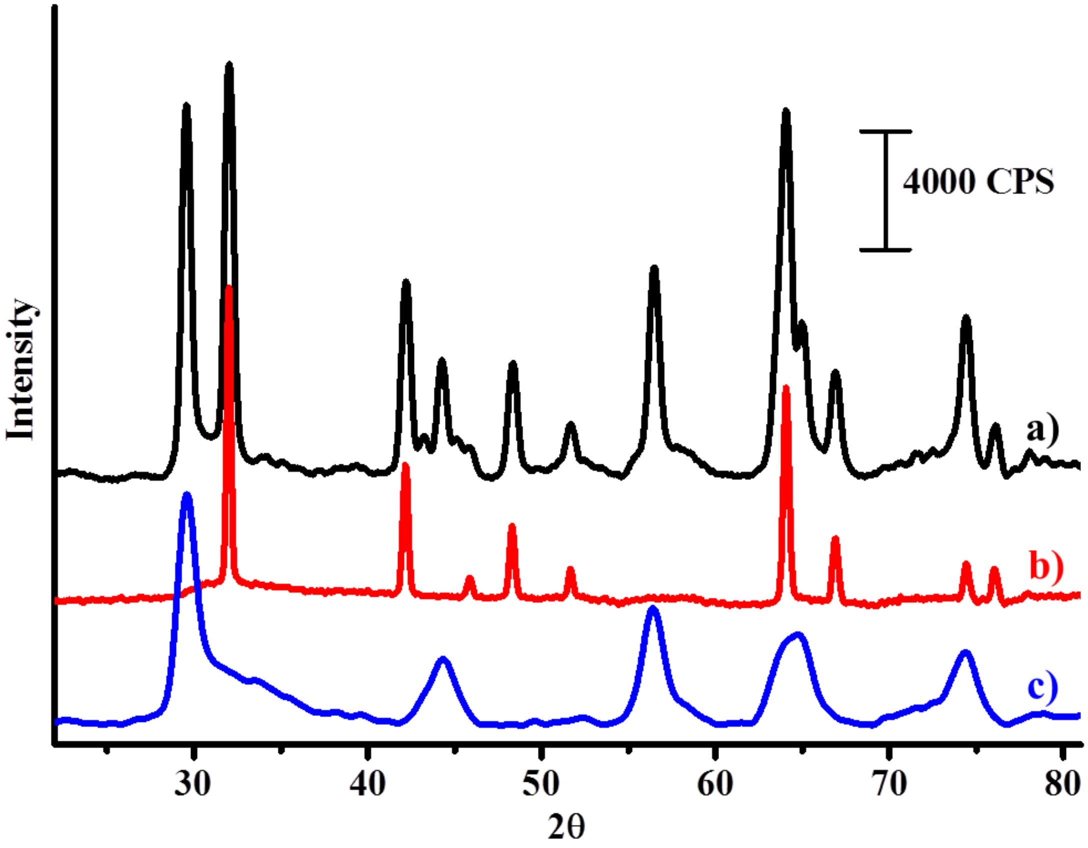

Figure 3.6: XRD spectra of TiO_2 samples: a) reference spectrum of mixed – rutile/anatase; b) rutile; c) anatase. Samples b) and c) were prepared as a part of this work. Spectra have been vertically adjusted for clarity.

mixture of anatase and rutile phases. The vibrational modes and their assignments are also shown. Raman also has the capability to detect a combination of polymorphs that are found within a single sample. XRD has the same capability and has been known as the standard for identifying polymorphs,[95] but the analysis of nanoparticles by this technique has proven a bit problematic as the very small particle sizes causes peak broadening. Because the Bragg diffraction angles (2θ) can be quite similar for polymorphs of the same material, peak broadening can hinder the accuracy of determining peak positions. Decreasing crystallite sizes can cause peak broadening in Raman as well, but the TiO_2 polymorphs have spectra that are distinctively different and the degree of broadening is not nearly as pronounced as in XRD. As crystallite sizes increase and XRD become more useful for analysis, the three most intense peaks in each spectrum will be used to identify the polymorphs present. The spectra shown in figure 3.6 show the diffraction pattern of rutile, anatase and a combination of the two polymorphs. The three most intense modes for anatase are at 29.4°, 44.2° and 56.4°.[168] Alternatively, the three most intense modes for rutile are at 31.9°, 42.1° and 64.0°.[169] The three modes were primarily used to determine the phase present in each sample. Also evident is the peak broadening phenomena that occurs in XRD due differences in crystallite sizes.

3.5 TiO_2 Phase Transition

After TiO_2 particles were synthesized, including surface modified (where applicable), the samples were exposed to several 4 hour heating cycles. Raman, XRD and FTIR analyses were performed after each heating cycle to determine the phase as well as the molecular species present. The literature accepted values for the amorphous to anatase transition (α-A) and the anatase to rutile (A-R) transition is approximately 400 °C and 750 °C when heated for 4 hours.[31]

A heating profile was performed on unmodified (pure) TiO_2 to serve as a control for the changes in phase. Figure 3.7 shows the Raman analysis after each 4-hour annealing stage. Although the synthesis conditions call for the formation of amorphous particles, there is some indication that pure TiO_2 samples did contain a small portion of anatase after drying yet before the first heating cycle. This can be attributed to the drying step. Although the samples are filtered and dried at 60 °C for several hours, the constant input of thermal energy could be responsible for inducing partial crystallization in these samples. As the heating steps continued, the spectra showed the complete transformation from amorphous to that of anatase (α-A) at 400 °C. After each heating cycle, the anatase peaks became more defined and pronounced which suggests an increase in long range order as well as increased average crystallite size.[170] At 650 °C, a very small rutile feature began to appear at 448 cm^{-1} (E_g mode) which indicates that the transformation from anatase to rutile had begun, albeit in the very early stages. After heating at 800 °C, the spectrum shows that there was no anatase remaining and that the sample was now exclusively rutile. Aside from the reduction of features associated with adsorbed water, the FTIR spectra remained essentially unchanged throughout the heating cycles.

The attempts to adsorb borate to the surface of TiO_2 proved unsuccessful as there was no indication in FTIR and XPS of the borate species being present. In addition to this lack of spectroscopic evidence, the Raman spectra (not shown) of the heating profile of the B-Mod TiO_2 samples looked remarkably similar to that of pure TiO_2. The anatase phase was exclusively present at 400 °C. At 650 °C, a mixture of anatase and rutile appears to be present as a small rutile feature appears at 448 cm^{-1} (E_g mode) in the Raman spectrum. The spectrum taken at 800 °C indicated that the sample has been transformed to rutile exclusively.

FTIR spectra, shown in figure 3.7, indicated that the propionic acid species was attached to the surface of TiO_2 in its “as prepared” state. After heating the sample at 400 °C, the wag (1305 cm^{-1}) and deformation (1471 cm^{-1}) modes of the methylene group as well as the symmetric (1435 cm^{-1}) and asymmetric (1521 cm^{-1}) features associated with the carboxylate group were no longer present. Previous work performed by Khlestkin et al. has shown that metal carboxylates usually decompose into the simple gaseous products, carbon dioxide and carbon monoxide, at temperatures in excess of about 330 °C.[171, 172] As thermal decomposition of the carboxylate group would cause the C-Mod TiO_2 to greatly resemble pure TiO_2, the Raman heating profile of C-Mod TiO_2 showed the same general trend as the pure TiO_2. The α-A transition was complete after heating at 400 °C and the A-R transition had begun after heating at 650 °C indicated by the appearance of the E_g mode at 448 cm^{-1}. After the 800 °C heating step, no evidence of the anatase phase was present as the sample contained rutile exclusively.

FTIR and XPS analyses confirmed that the sulfate species successfully adsorbed to the surface of TiO_2. The heating profile of the S-Mod TiO_2 sample showed the same α-A transition as pure TiO_2. The Raman spectra of the “as prepared” sample showed evidence that there was a mixture of amorphous and anatase phase. At 400°C, the α-A transition appears to be complete as the spectrum indicates the presence of anatase only and it would remain as such after the 500 °C heating cycle as well. The FTIR spectra showed that the sulfate functional group was present after the 500 °C heating step. After heating at 650 °C however, the features associated with the sulfate group (1043 cm^{-1}, 1131 cm^{-1} and 1203 cm^{-1}) are no longer present in the FTIR and the Raman spectrum shows that the A-R transition had begun. The decomposition of the sulfate

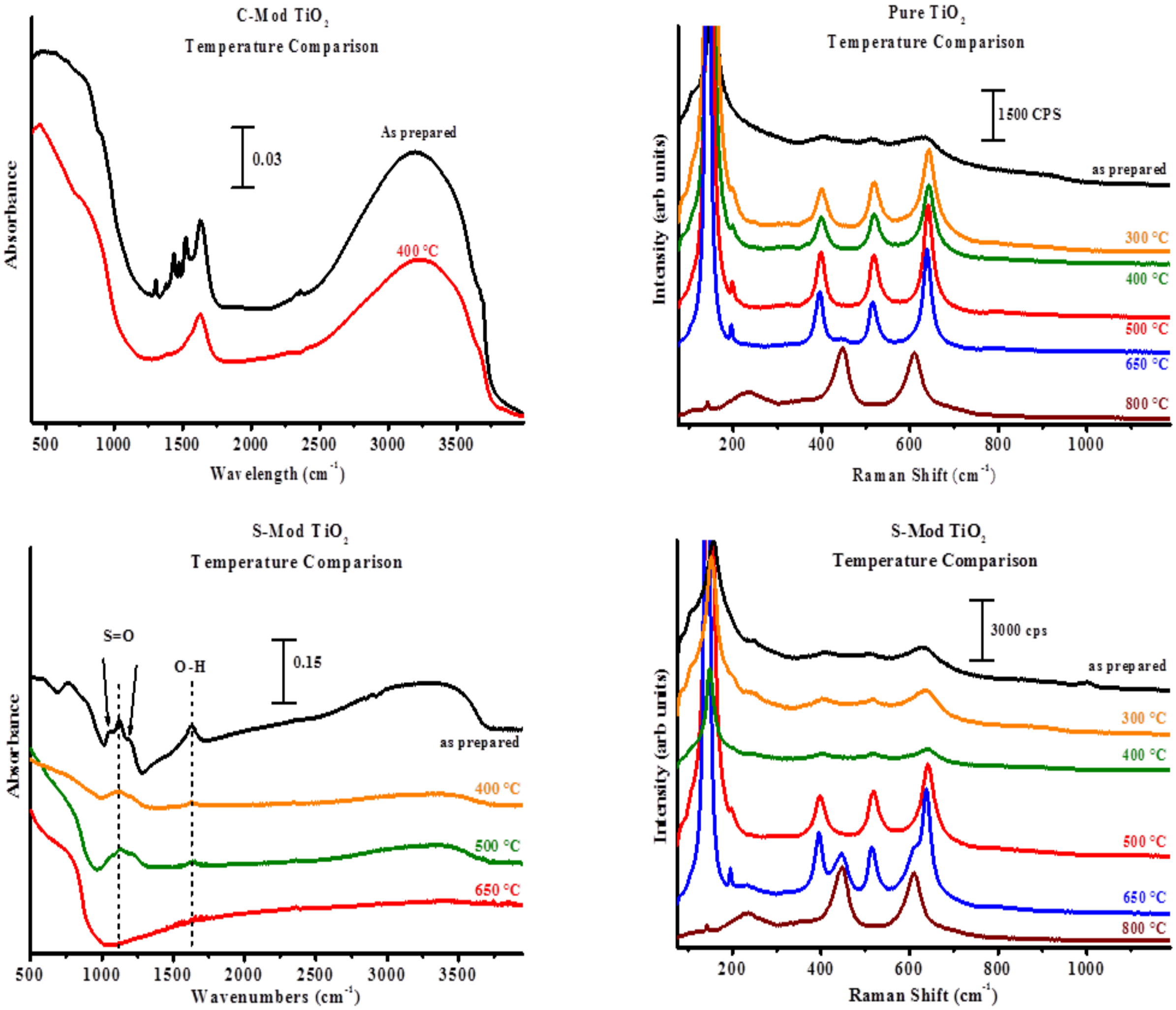

Figure 3.7: FTIR and Raman spectra of Pure, C-Mod and S-Mod TiO_2

occurs during the 650°C heating step which essentially transforms the sample into pure TiO_2 and the heating profile is likewise similar to that of pure TiO_2. It has been shown that various metal sulfates thermally decompose into predominantly SO_3 and O_2 within the temperature ranges of 500°C - 700°C.[173, 174] After the final 800 °C heating step, Raman analysis shows that the sample is entirely converted to rutile.

The presence of the phosphate species was confirmed present by FTIR and XPS analyses. The sample consisted of amorphous TiO_2 with there being no indication of the presence of anatase. The α-A transition occurs after being heated at 400 °C. At 650°C, there is no indication of the A-R transition occurring. FTIR analysis at this temperature shows that the phosphate species, a lone broad feature around 1035 cm^{-1}, is still present. In fact, the phosphate species survives the 800 °C heating cycle. The Raman analysis of the 800 °C heating step shows that the sample is still anatase with no indication of the A-R transition occurring. The continued presence of the anatase phase exclusively after being heated to 800 °C exceeds the accepted literature values for the A-R phase transition temperature as well as the experimental values presented in this work for pure TiO_2.

The Si-Mod TiO_2 sample has the presence of the organosilicate species confirmed by XPS and FTIR. The amine (1620 cm^{-1}), methylene (1302 cm^{-1} and 1471 cm^{-1}), methyl (1389 cm^{-1}) and silicate (1103 cm^{-1}) feature are all present initially in the FTIR spectrum. Two broad features appear after heating to 400 °C, one associated with the silicate feature (~1103 cm^{-1}) and one associated with the deformation of the methylene group in the alkyl chain (1411cm^{-1}). After proceeding to higher heating temperatures, the silicate species remains relatively unchanged whereas the methylene feature further decreases until it is no longer present at 800 °C. The silicate features present in the FTIR is indicative of the formation of a polymeric chain.[128]

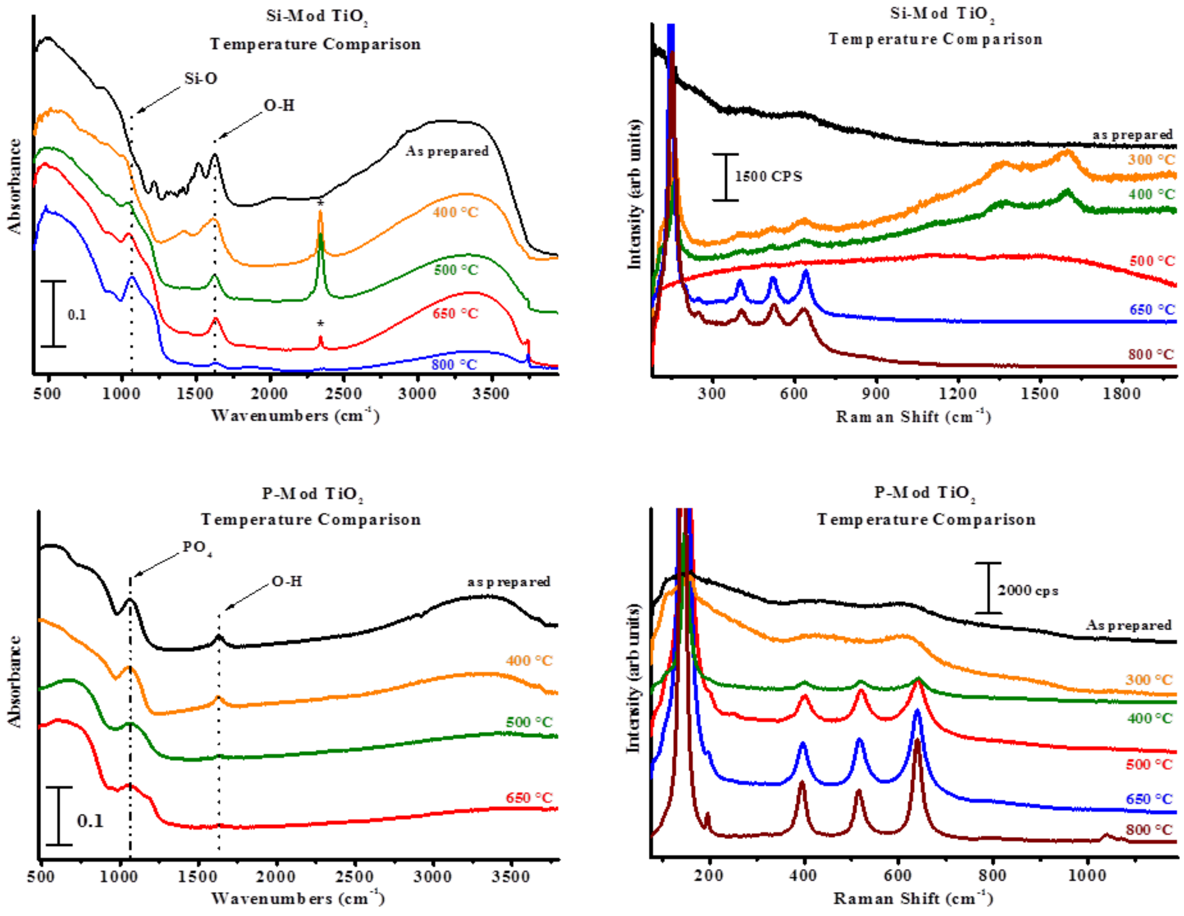

Figure 3.8: FTIR and Raman spectra of Si-Mod and P-Mod TiO_2

The Raman spectrum shows the sample to be amorphous TiO_2. After both the 300 °C and 400 °C heating cycles, the sample converted from amorphous TiO_2 to the anatase phase. The carbonaceous component of the APTES is converted to graphitic carbon as the D (1354 cm^{-1}) and G (1600 cm^{-1}) band appear in the spectra. The D-band of graphene is the primary mode indicative of the planar sp^2 carbons. The G-band is known as the disorder/defect band that represents the breathing mode of the sp^2 carbons rings. The graphene present in this sample has a high degree of disorder when considering the relative intensities of the D-band to the G-band because the intensity of the D-band is directly proportional to the defects in the sample.[175-177] It should also be noted that the samples heated to 300 °C and 400 °C exhibited fluorescence which suggests the formation of a new species post heating. After heating at 500 °C, the species causing fluorescence becomes more prevalent which causes an otherwise uninformative spectrum. The species causing fluorescence was unable to survive the 650 °C heating cycle as the Raman spectrum reveals only the anatase phase. The features associated with graphene are no longer present. The Raman spectrum of the sample heated to 800 °C looked virtually identical to the sample heated to 650 °C in that the sample was exclusively anatase with no indication of rutile being present.

XRD, as shown in figure 3.9, was used to further confirm the TiO_2 phase present at 400 °C and 650 °C. The results are consistent with the Raman spectra. The most intense peak, at 29.4° for anatase and at 31.9° for rutile, was used to determine the phase present since the very small average crystallite sizes caused peak broadening that was most prevalent at larger diffraction angles. Figure 3.9 also shows that at 400 °C, pure and S-Mod samples contain anatase with slightly larger average crystallite sizes than P-Mod and Si-Mod as evident by the more defined peaks. At 650 °C rutile features appear in the pure and S-mod samples.

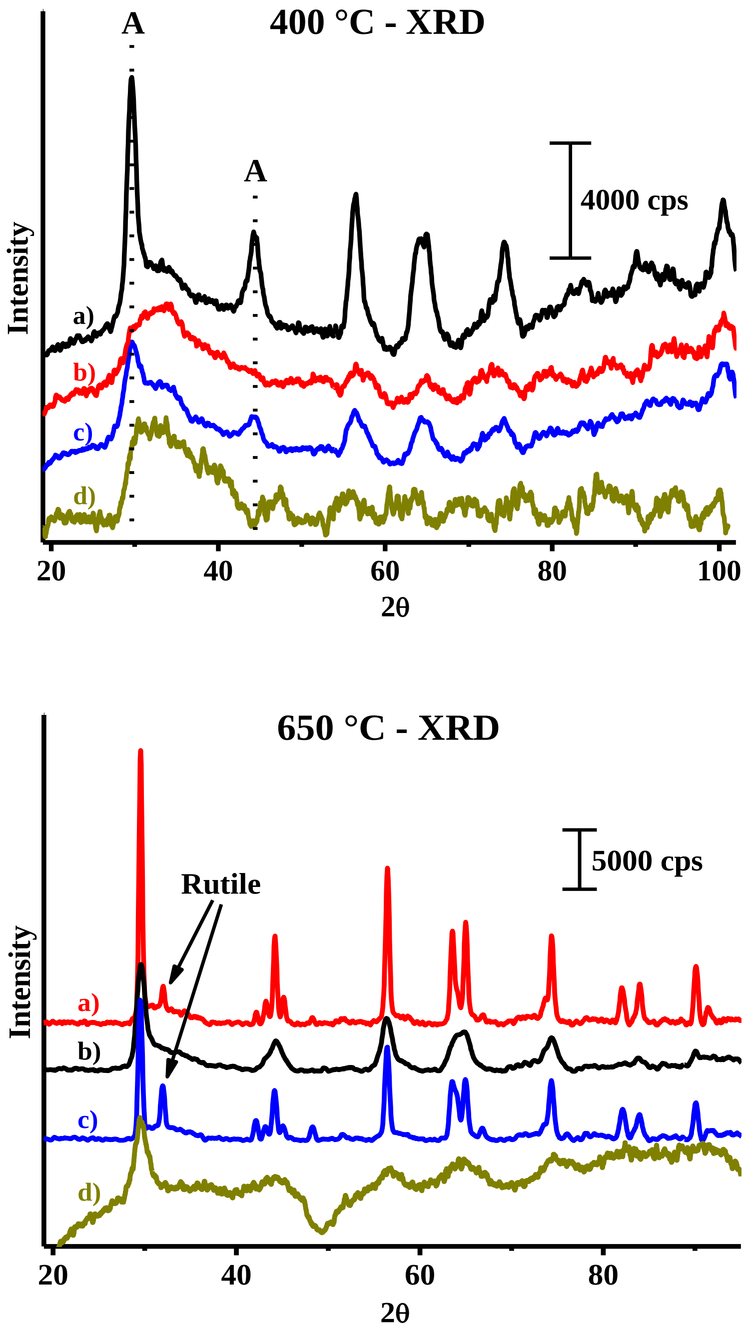

Figure 3.9: XRD of modified TiO_2 at 400 °C and 650 °C. In both spectra, the samples are a) pure; b) P-Mod; c) S-Mod; d) Si-Mod. Average crystallite sizes at 400 °C and 650 °C were determined by Scherrer analysis to be a) 7 nm and 35 nm; b) 2 nm and 8 nm; c) 5 nm and 21 nm; and d) unable to determine

The P-Mod and Si-Mod samples are exclusively anatase with no evidence of rutile being present. All samples experienced particle growth, or sintering, as a result of the high annealing temperatures.

3.6 Energetics of A-R Phase Transition

Although the pure and S-Mod TiO_2 samples began A-R transition around 650 °C and were complete at 800 °C, it can be clearly seen that the A-R transformation was hindered beyond 800 °C for the Si-Mod and P-Mod samples. If an Arrhenius activated process (eq 3.1) is

$$k = \mathrm{A}e^{-\mathrm{Ea}/\mathrm{RT}} \tag{3.1}$$

assumed as well as a first order rate law, approximate activation energies for the samples can be determined as they undergo the A-R transition. In this expression k is the rate, A is the frequency factor, E_a is the activation energy, R is the gas constant and T is the temperature. Table 3.3 shows the temperature, the value of RT and an indication of the phases present as indicated by Raman analysis. No rutile being formed after 4 hours (14,400 seconds) at 500 °C (pure and S-Mod) and 800 °C (Si-Mod and P-Mod) for the respective samples, is an indication of a very slow A-R transition rate. To determine the minimum activation energy required to detect a minimal amount (~ 3-5%) of rutile, a plot of percent transformed as a function of time in seconds was used. From this plot, the E_a required to yield rutile at 650 °C (pure and S-mod) and 800 °C (Si-Mod and P-Mod) was determined to be greater than 91 kJ/mol and 105 kJ/mol respectively.

Anatase to Rutile Transformation						
Temp (°C)	**Temp (K)**	**RT (kJ/mol)**	**Pure**	**S-Mod**	**Si-Mod**	**P-Mod**
27	300	2.5	A	A	A	A
300	573	4.8	A	A	A	A
400	673	5.6	A	A	A	A
500	773	6.4	A	A	A	A
650	923	7.7	A+R	A+R	A	A
800	1073	8.9	R	R	A	A

Table 3.3: Anatase to rutile transformation. (A) is anatase and (R) is rutile

The activation energy of TiO_2 A-R transition has been shown to be particle size dependent.[110] As average crystallite size decreases, the A-R activation energy decreases as well.[178] Smaller crystallite sizes tend to have higher surface areas which generally possess higher surface energy and surface stress energy than larger crystallite sizes with lower surface areas. The tendency of surfaces to achieve the lowest possible surface energy makes it more susceptible to undergo change (lower activation energy). Li et al. determined the activation energies of pure TiO_2 to be 299, 236 and 180 kJ/mol for 23, 17 and 12 nm TiO_2, respectively.[110] The minimum activation energy values determined in this work are consistent with these findings as initial crystallite sizes were all less than 7 nm. Although consistent with previous works, the ~14 kJ/mol difference in activation energies of the samples prepared in this work is a minimum value, so further experimentation would be required to determine the precise values.

3.7 Conclusions

TiO_2 samples were prepared by the sol-gel method and surface modification was attempted with various SMS. Although there was no spectroscopic evidence of successfully adsorbing the borate SMS to the TiO_2 surface, successful surface adsorption was achieved with the carboxylate, sulfate, phosphate and silicate species. After exposing samples to various heating stages, the TiO_2 phase present was observed and compared to that of the unmodified (pure) TiO_2 sample exposed to the same conditions. There were some slight variations in the temperature at which the α-A conversion began throughout the samples which resulted in a mixture of amorphous and anatase until the 400 °C heating step was complete. After heating at this temperature, no amorphous components remained as the sample consisted solely of anatase.

Samples modified with the carboxylate and sulfate species showed no difference in their A-R phase transition temperature to that of pure-TiO_2. The SMS utilized in these two samples were unable to withstand these temperatures needed to induce phase transformation in the TiO_2 crystal. After their desorption due to thermal decomposition, the samples were essentially pure TiO_2 and the corresponding temperature needed to cause the A-R conversion was identical to that required for pure TiO_2.

The samples modified with the phosphate and silicate species showed a noticeable difference in the A-R phase transition temperature. Unlike the C-Mod and S-Mod TiO_2 samples which completely transformed from anatase to rutile at 800 °C, the P-Mod and Si-Mod samples remained in the anatase phase despite being heated beyond this temperature. It was also determined that the phosphate and silicate species remained present on the samples, as indicated by FTIR. The ability of these two SMS to remain present on the surface at these elevated temperatures were shown to hinder the A-R phase transition temperature.

The A-R phase transformation is known to be a reconstruction process.[179, 180] This reconstruction process has been shown to follow the core-shell model in which the initial A-R transformation begins at the surface and propagates throughout the bulk until complete conversion to rutile occurs.[181] The presence of a surface adsorbed species prevents the initiation of the A-R transformation by blocking reconstruction at the surface. The A-R transformation would not be able to occur as long as there is a SMS present.

CHAPTER 4 – PHOTOCATALYTIC PROPERTIES OF BULK AND SURFACE MODIFIED TiO_2

4.1 Introduction

Titanium dioxide (TiO_2) is a common and naturally occurring mineral that has a wide range of applications. The effectiveness of TiO_2 in some applications is highly dependent upon the polymorph used. The most common of these phase-dependent applications is the use of TiO_2 as a photocatalyst. Although three common polymorphs exist, anatase and rutile have shown promise as a photocatalyst. When used as a photocatalyst, the ability of TiO_2 to absorb photons is governed by the bandgap energy.

Surface modification of TiO_2 was discussed extensively in previous chapters (§1.4.4) as it can be used as a way to link other photoactive molecules to the surface of TiO_2. The species that is bound to the surface can provide a conduit for photons to enter its bulk structure after absorbing incident radiation. The surface bound molecule can be specifically chosen to absorb photons possessing energy outside the bandgap energy of TiO_2 which would make for a more versatile photocatalyst than pristine TiO_2.

There has been much work done on increasing TiO_2 photoactivity by modifying the bulk structure (§1.4.3), or doping. The aim of doping, regardless of the dopant, is to change the electronic structure of a photocatalyst, yet maintain the integrity of its crystal structure. This bulk modification can alter the bandgap energy of TiO_2 which will allow it to absorb solar radiation with greater efficiency. Just as the identity of the dopant atoms has varied, so has the method of incorporating the dopant atoms into the TiO_2 matrix. Some preparation methods for doped TiO_2 include hydrothermal,[182-184] chemical reduction,[185] ion-implantation,[186, 187] anodic oxidation,[188] ion-assisted sputtering,[189-192] mechanochemical grinding,[193-195] chemical vapor deposition,[196] oxidative annealing[197] and sol-gel.[198-203] The dopants used are generally classified into three different categories: the noble metals, cationic and anionic.

The noble metals include gold,[204] platinum,[205] palladium[206] and silver.[207-209] This class of dopants are utilized to enhance photocatalytic efficiency due to their Fermi level being lower than that of TiO_2.[210] Upon the excitation of TiO_2, electrons are promoted from the valence band (VB) to the conduction band (CB) and a corresponding hole is left in the VB. The lower Fermi level of noble metals reduces the possibility of electron/hole recombination by receiving the photoexcited electrons from the CB instead of them returning to the VB where recombination with the hole occurs.

Cationic dopants are metals, most commonly transition metals, though some group I and group II metals have been studied. Of the transition metals iron,[211-213] cobalt,[214-217] copper,[218-220] nickel,[221, 222] chromium[223, 224] and vanadium[225-227] are among the most commonly studied. Within the band gap of a semiconductor, metal ions can provide additional energy levels. The additional energy levels provided allow for photons of lower energy to induce charge transfer from the VB to the CB versus the inability to in the unmodified semiconductor. Pristine TiO_2 has a band gap energy that falls in the UV region of the electromagnetic spectrum which only accounts for about 4% of incident sunlight. Visible light however, accounts for a much greater percentage of solar radiation, so the utilization of cationic dopants in TiO_2 allows for visible light photoexcitation.

Anionic dopants that have been studied include boron,[228-230] sulfur,[231, 232] iodine,[233, 234] fluorine,[235-237] carbon,[238-240] nitrogen,[241, 242] and phosphorus.[243, 244] The non-metal atoms mentioned above are usually substitutionally doped in the TiO_2 crystal structure by replacing oxygen. The band gap of TiO_2 is narrowed as the oxygen 2p and dopant p states are mixed which has been shown to make TiO_2 doped with anionic dopants responsive to visible light.[245, 246] Anionic dopants are also of interest because they are reportedly less likely to form recombination centers.[247]

In this work, transition metal atoms were used as dopants for anatase TiO_2. After doping, the samples were then modified by the attaching oxyacids to the surface. The TiO_2 samples, altered by the combination of doping and surface modification, were then photoexcited to see how the photocatalytic activity was affected.

4.2 Doped TiO_2 Synthesis

All TiO_2 samples were prepared by a room temperature sol-gel method that was largely based on work previously performed by Korosi.[248] A modification to this synthetic procedure was made in that solutions containing 3 at. % transition metal dopants were added to produce doped TiO_2. Initial solutions of the each dopant precursor were produced by adding vanadium acetylacetonate, copper (II) chloride and cobalt (II) chloride to absolute ethanol. Each solution was ultrasonicated to ensure complete dissolution of the solid then magnetically stirred for several minutes. To this solution, 14.8 mL of titanium (IV) isopropoxide (Ti-O*i*Pr) was added. After adding, there were no visible signs of TiO_2 formation as the mixture of the solution remained in liquid form. The last step in the formation of doped TiO_2 was the addition of 250 of mL DI water. The addition of water promoted the hydrolysis of Ti-O*i*Pr which resulted in the immediate formation of TiO_2 gel. After stirring for 2 hours, the reactions were considered complete and the collection process was performed as outlined in §2.9 of this work. The collected samples were then annealed at 550 °C for 4 hours to induce crystallization to the anatase phase. After the heat treatment was complete, the samples were analyzed for polymorphic phase and content. Unlike pristine TiO_2 which is a vibrant white, the doped samples possessed a faint color. Vanadium doped TiO_2 (V-TiO_2) was light brown, cobalt doped TiO_2 (Co-TiO_2) was light blue and copper doped TiO_2 (Cu-TiO_2) was light green as shown in figure 4.1.[201, 249]

4.3 Surface Modification of Doped TiO_2

After analysis, two 0.185 g portions of each doped TiO_2 sample was placed in separate flasks where 200 mL of 0.05 M surface modifying species (SMS) was added. To one sample, sulfate was added and to the other phosphate was added as the SMS. The six total samples were identified as the dopant, TiO_2 and the SMS (ie. Co-TiO_2-S is cobalt doped TiO_2 with sulfate attached to the surface). The samples were allowed to magnetically stir at room temperature for 2 h at which point the reaction was considered complete and the collection process began, as previously outlined (see §2.9). After collecting, the samples were analyzed for polymorphic phase and content.

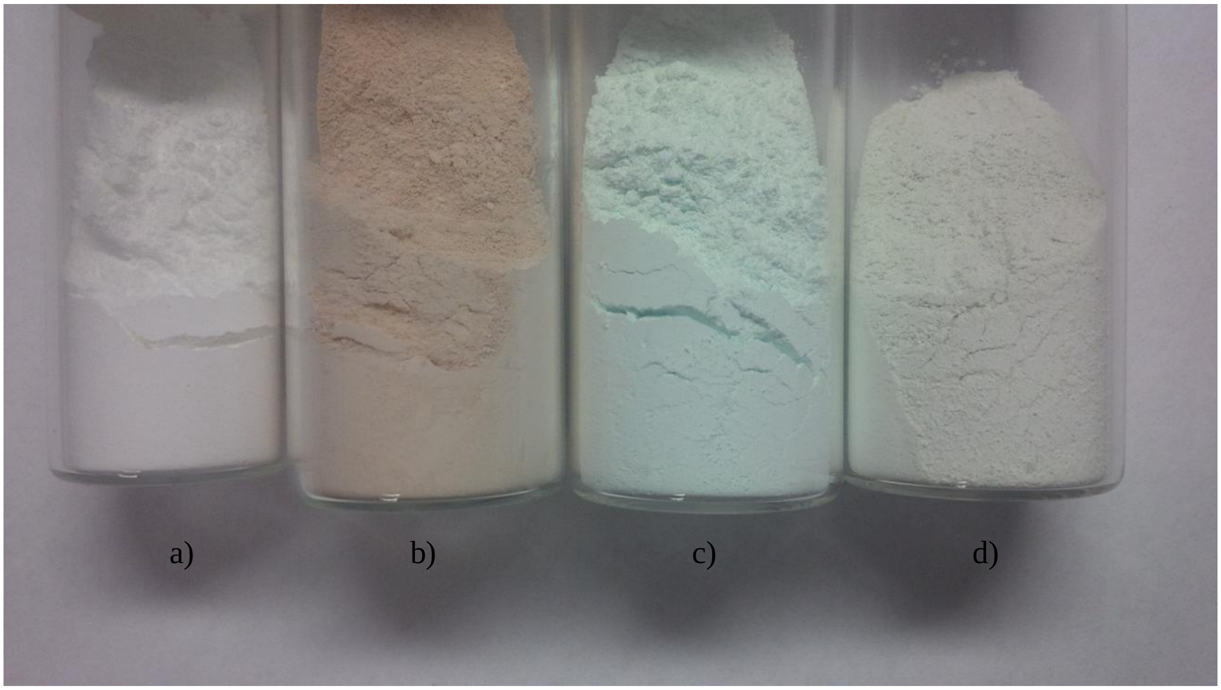

Figure 4.1: As prepared TiO_2 samples: a) pure TiO_2; b) V-TiO_2; c) Co-TiO_2; d) Cu-TiO_2.

4.4 Sample analysis

The samples were analyzed via x-ray diffraction (XRD), Raman spectroscopy (Raman) and diffuse reflectance infrared fourier transform spectroscopy (DRIFTS) for polymorphic phase and content. The analysis of XRD via the Scherrer analysis was used to determine average crystallite size.[93] Ultraviolet-visible spectroscopy (UV-Vis) was also performed to determine the band gap energy of each sample. The TiO_2 samples doped with vanadium, cobalt and copper were denoted as V-TiO_2, Co-TiO_2 and Cu-TiO_2 respectively.

4.4.1 XRD

After synthesis was completed, all samples were analyzed via XRD. This technique was used to confirm the polymorphic phase present as well as to determine if any other oxide samples were present as a result of coprecipitation of dopant atoms. In figure 4.2, the peak positions were indicative of anatase.[168] The peak positions (shown in table 4.1) of the three doped samples were all in good general agreement with the pure sample. Within the spectra of the doped samples however, a slight shift to lower diffraction angles is observed. Work performed by Gonell et al. states that this shift indicates the substitutional doping of metal ions replacing Ti^{4+} ions in the TiO_2 lattice.[250-252] This shift is small, but observable, in the sample containing cobalt but more pronounced in the samples containing copper and vanadium. There was no evidence found in any of the diffraction patterns that corresponded to any of the metals used to dope the TiO_2 samples. Average crystallite size was also determined from the XRD spectra by using the Scherrer analysis (previously detailed in §2.3). From this analysis, the average crystallite size was determined to be 14 nm (pure), 13 nm (cobalt), 13 nm (copper) and 13 nm (vanadium).

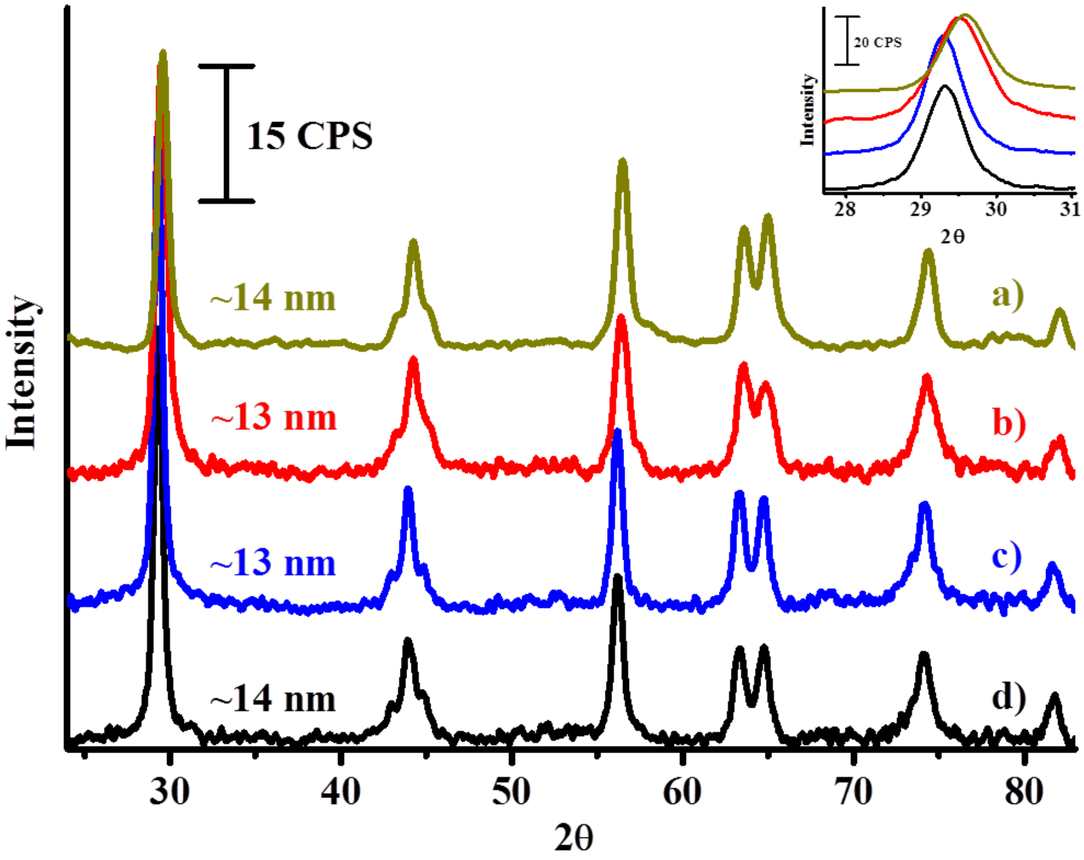

Figure 4.2: Doped TiO_2 samples: a) pure TiO_2; b) Cu-TiO_2; c) Co-TiO_2; d) V-TiO_2. All spectra have been vertically adjusted for clarity. Scherrer analysis was utilized to determine the average crystallite size. [ref. 93]

XRD Analysis (Cobalt kα = 1.78897 Å)						
Sample	**Diffraction Angles (2θ)**					
JCPDS anatase	29.5	44.2	56.5	63.6	65.0	74.4
Pure TiO_2	29.6	44.2	56.5	63.6	65.0	74.4
Cobalt - TiO_2	29.4	44.2	56.4	63.5	64.9	74.3
Copper - TiO_2	29.3	43.9	56.2	63.3	64.7	74.1
Vanadium - TiO_2	29.3	43.9	56.1	63.3	64.7	74.1

Table 4.1: XRD diffraction angles of TiO_2 samples [ref. 168]

4.4.2 UV-Vis

UV-Vis spectroscopy was performed in order to experimentally determine the band gap energy of the pure and doped samples.[97, 98] The band gap energy is extracted from each spectrum shown in figure 4.3. For pure TiO_2 (upper left), the value of 388 nm is consistent with the accepted literature value for anatase TiO_2.[253-256] The V-TiO_2 and Co-TiO_2 samples (upper and lower right respectively) exhibit a widening of the band gap energy as the values are shifted to shorter wavelengths. Cu-TiO_2 displayed a narrowing of the band gap energy and shifted to longer wavelengths. This widening and narrowing of the band gap is commonly referred to as blue and red shifted respectively.

The shift of the band gap to 348 nm in V-TiO_2 corresponds to the substitutional doping of V^{4+} in the TiO_2 lattice.[257-259] The atomic radius of V^{4+} (0.72 Å) is comparable to that of Ti^{4+} (0.75Å) which supports the concept of substitutional doping. Co-TiO_2 exhibited a blue shift of its band gap energy to 370 nm when compared to pure TiO_2. This value is consistent with the work performed by Alamgir et al.[254] Although, Co^{2+} has a slightly larger atomic radius (0.79 Å) than that of Ti^{4+} (0.75 Å), Weng et al. reported that cobalt is substitutionally doped into the TiO_2 lattice as Co^{2+} (low spin state).[10, 249, 260-262] The Cu-TiO_2 sample, found in the lower left of figure 4.3, shows an approximate band gap energy of 407 nm. This value is of slightly longer wavelength (red shifted) than that of pure TiO_2, which is consistent with that reported other works.[219, 263] Copper is substitutionally doped in the TiO_2 lattice as Cu^{2+} despite having a significantly larger ionic radius than Ti^{4+} (0.87 Å and 0.75 Å respectively). The red shift of Cu-TiO_2 band gap can be attributed to the lattice distortion caused by incorporating Cu^{2+} ions.[219]

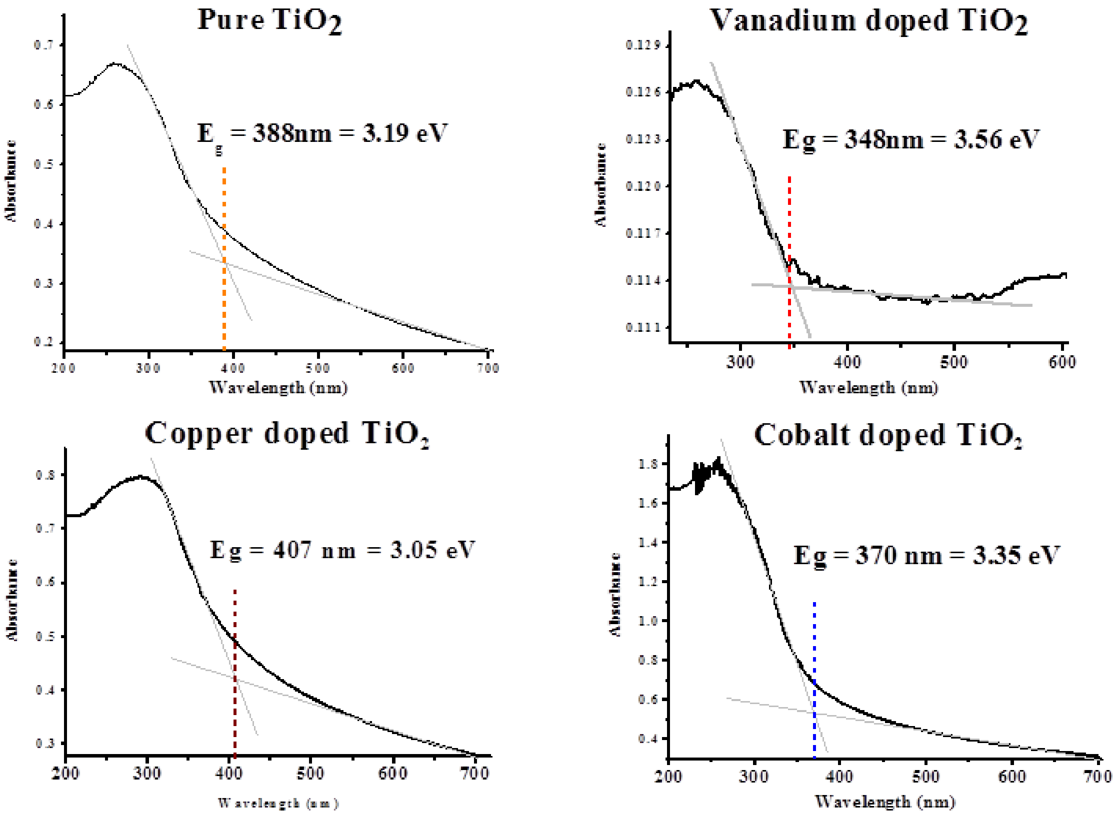

Figure 4.3: UV-Vis spectra of pure and doped TiO_2 samples

4.4.3 FTIR (DRIFTS)

DRIFTS analysis (figure 4.4) was performed to identify the functional groups present. The full FTIR spectrum (upper left and upper right) of pure TiO_2 consist of a broad feature at the low wavenumber region ~500 cm^{-1} – 900 cm^{-1} that is attributed to Ti─O─Ti lattice vibrations.[47, 137] The peak at 1627 cm^{-1} is due to the O─H bending mode of water and/or surface hydroxides. The high wavenumber features, the broad ~2800 cm^{-1} – 3400 cm^{-1}, represent hydrogen bonding from surface absorbed water.[138] The peaks at 3689 cm^{-1} and 3674 cm^{-1} are both assigned to the O─H stretching of hydroxyl groups.[140] The same general line profile was present in all samples that were analyzed. Although vanadium doped samples were synthesized, there was no indication that successful surface modification was achieved so it warrants no further mentioning in this work.

The left center and left lower graphs in figure 4.4 contain the spectra, with deconvoluted features, of copper and cobalt doped TiO_2 with sulfate attached to the surface. The metal doped and surface modified samples will be identified as Cu-TiO_2-S (copper) and Co-TiO_2-S (cobalt). In the left center graph (Cu-TiO_2-S), there are five peaks that are associated with the sulfate species that are bound to the surface. These positions, as identified in the graph (and table 4.2), are 974 cm^{-1}, 1049 cm^{-1}, 1133 cm^{-1}, 1212 cm^{-1} and 1261 cm^{-1} which are consistent with the frequencies observed by Lane et al.[143] It is proposed from the vibrational frequencies that the sulfate species are bound to the surface of Cu-TiO_2 in two different orientations, both bridging bidentate and chelating bidentate. The sulfate feature at 974 cm^{-1} (ν_1) suggests bridging bidentate whereas the highest wavenumber feature at 1261 cm^{-1} (ν_3) is consistent with that observed in chelating bidentate orientation.[141] Although the two aforementioned features are commonly identified as M─SO_4 features, the remaining peaks at 1046 cm^{-1}, 1133 cm^{-1} and 1212

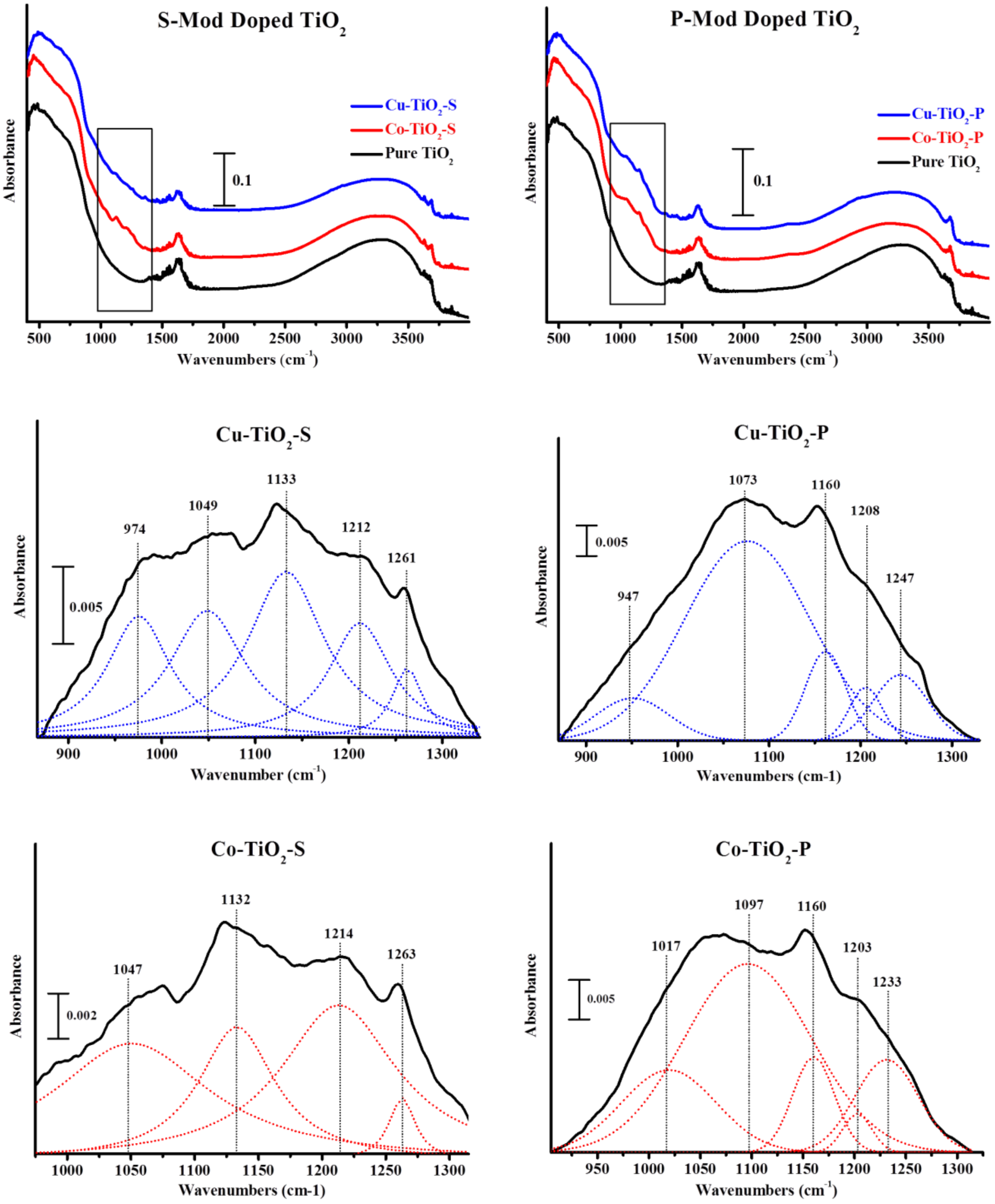

Figure 4.4: DRIFTS analysis of doped samples with surfaces modified by sulfate (upper left) and phosphate (upper right). The middle and lower graphs show the zoomed in region of interest of the corresponding spectra.

FTIR Analysis (Sulfates)

Cu-TiO$_2$-S	Co-TiO$_2$-S	Sulfate[143]	Chelating[141]	Bridging[141]
974 cm^{-1}	–	919 cm^{-1}	–	971 cm^{-1}
1049 cm^{-1}	1047 cm^{-1}	1045 cm^{-1}	1000 cm^{-1}	1035 cm^{-1}
1133 cm^{-1}	1132 cm^{-1}	1183 cm^{-1}	1125 cm^{-1}	1110 cm^{-1}
1212 cm^{-1}	1214 cm^{-1}	1213 cm^{-1}	1160 cm^{-1}	1195 cm^{-1}
1261 cm^{-1}	1263 cm^{-1}	1256 cm^{-1}	1255 cm^{-1}	–

FTIR Analysis (Phosphates)

Cu-TiO$_2$-P	Co-TiO$_2$-P	Phosphate[139, 140]	Chelating[141]	Bridging[141]
947 cm^{-1}	1017 cm^{-1}	960 cm^{-1}	–	972 cm^{-1}
1073 cm^{-1}	1097 cm^{-1}	1075 cm^{-1}	1033 cm^{-1}	1055 cm^{-1}
1160 cm^{-1}	1160 cm^{-1}	1155 cm^{-1}	1145 cm^{-1}	1115 cm^{-1}
1208 cm^{-1}	1203 cm^{-1}	1220 cm^{-1}	1212 cm^{-1}	–
1247 cm^{-1}	1233 cm^{-1}	1235 cm^{-1}	1240 cm^{-1}	–

Table 4.2: DRIFTS analysis of sulfated (upper) and phosphated (lower) doped TiO$_2$ samples.

cm^{-1} correspond to S─O stretching and the S=O symmetric stretch respectively.[264, 265] The Co-TiO_2-S sample (lower left) has sulfate features 1047 cm^{-1}, 1132 cm^{-1}, 1214 cm^{-1} and 1261 cm^{-1}. These features, as well as their vibrational mode assignments, are quite similar to those Cu-TiO_2-S with the exception of lacking the lowest wavenumber feature at 974 cm^{-1} (ν_1). The absence of this feature and the presence of the 1261 cm^{-1} peak suggest that the sulfate species is bound to the surface in chelating bidentate fashion.[141, 266]

The right center and lower right graphs in figure 4.4 contain the spectra of cobalt and copper doped TiO_2 with phosphate attached to the surface. The metal doped and surfaced modified samples will be identified as Cu-TiO_2-P (copper) and Co-TiO_2-P (cobalt) respectively. The spectrum in the right center position (Cu-TiO_2-P) has five features that correspond to the phosphate group and they are located at 947 cm^{-1}, 1073 cm^{-1}, 1160 cm^{-1}, 1208 cm^{-1} and 1247 cm^{-1} (also shown in table 4.2). The 1073 cm^{-1} and 1160 cm^{-1} features are those of the PO_2 symmetric and asymmetric stretches respectively.[126, 140] The peaks at 1212 cm^{-1} and 1261 cm^{-1} is assigned to the P=O group, with the former being of free P=O and the latter being hydrogen bonded.[126, 139, 140] The very low wavenumber and weakly absorbing feature at 947 cm^{-1} is consistent with that of asymmetric P─O─P stretch. The present of this feature suggests that some degree of dimerization of the phosphate occurs once bound to the surface of the substrate.[126] The lower right spectrum of figure 4.4 is that of Co-TiO_2-P. The positions identified are 1017 cm^{-1}, 1097 cm^{-1}, 1160 cm^{-1}, 1203 cm^{-1} and 1233 cm^{-1}. The peak at 1017 cm-1 corresponds to the asymmetric stretch of PO_3.[139] The PO_2 symmetric and asymmetric stretches are indicated by features at 1097 cm^{-1} and 1160 cm^{-1} respectfully. As was the case with the Cu-TiO_2-P sample, the hydrogen bonded P=O stretch (1203 cm^{-1}) and free P=O stretch (1233 cm^{-1}) are also present.[140] In both phosphated samples, the observed vibrational frequencies are slightly higher than phosphate vibrational frequencies found in other phosphate containing complexes which indicates a chelating bidentate bonding orientation.[140, 141, 266]

4.4.4 Raman

Raman analysis was performed to determine the TiO_2 polymorph present as well as any molecular species present. Figure 4.5 shows the Raman spectra of doped and surface modified samples before and after heat treatment. In all graphs, the spectra from top to bottom are: (a) pure TiO_2; (b) Co-TiO_2 and (c) Cu-TiO_2.

The upper graph shows the "as prepared" samples. In this graph all samples are determined to be amorphous TiO_2. The very broad features indicate quite small average crystallite sizes. The lower graphs are that of doped TiO_2 samples that have been annealed at 550 °C for 4 hours with phosphate (lower left) and sulfate (lower right) on the surface. In both graphs, the heat treatment transformed the samples from amorphous to anatase phase. The peak positions of pure TiO_2 are found at 147 cm^{-1} (E_g), 198 cm^{-1} (B_{1g}), 398 cm^{-1} (B_{1g}), 515 cm^{-1} (A_{1g} + B_{1g} combination) and 640 cm^{-1} (E_g). In spectra (b) and (c) the doped and surface modified samples (shown in both of the lower graphs) exhibit peaks that very closely resemble the peak positions of the pure TiO_2. There was no indication of co-crystallization of the cobalt or copper as no features associated with the oxides of these two elements were found in the spectra. Also, there were no features associated with the surface bound phosphate and sulfate species. It is suggested that the very intense features associated with the TiO_2 vibrational modes simply leave the lesser intense surface adsorbed, sulfate and phosphate, species buried within the baseline.

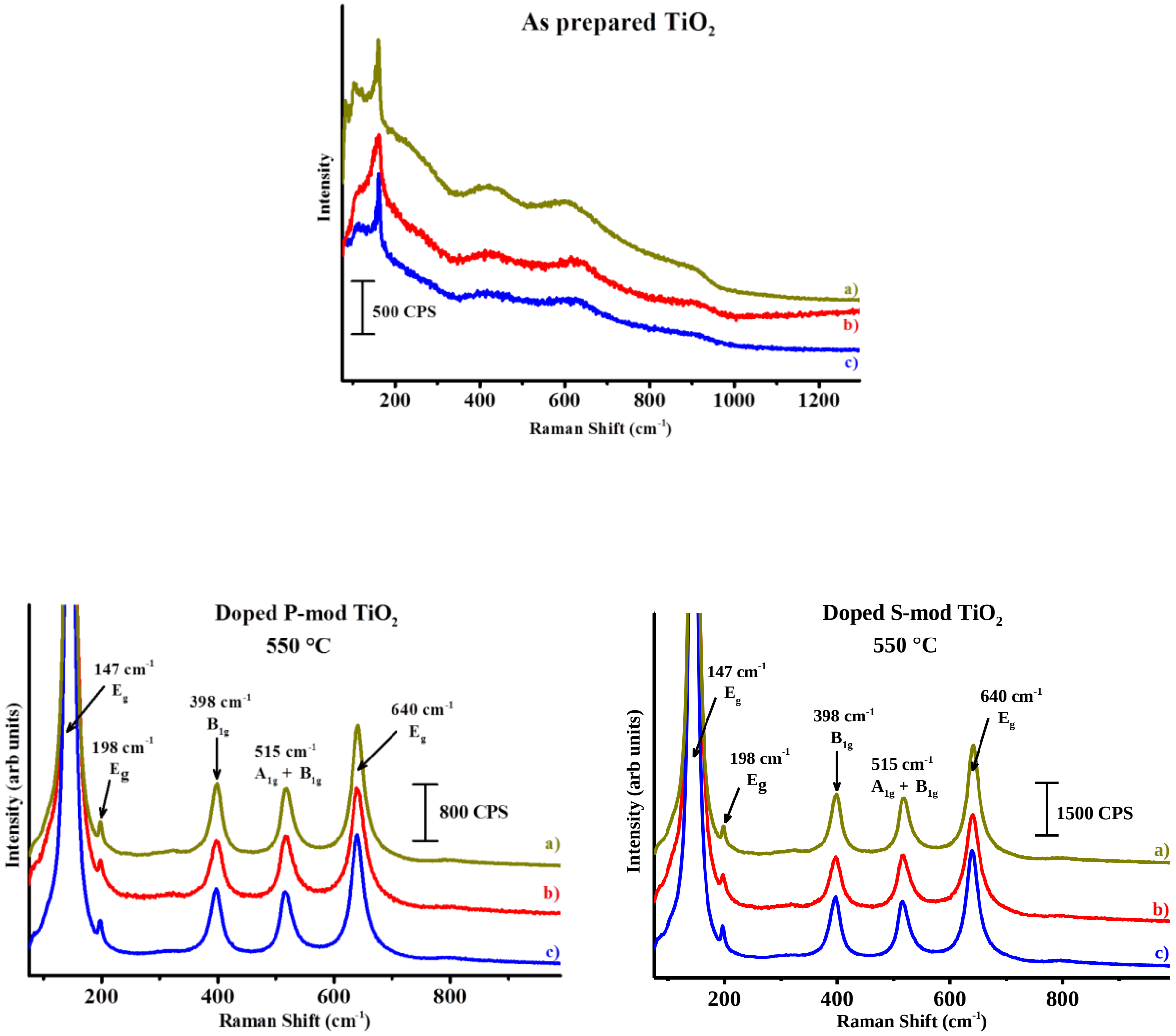

Figure 4.5: Raman analysis of doped samples. The top graph is for “as prepared” samples. The lower graphs are after annealing at 500 °C for 4 hours with surfaces modified by phosphate (lower left) and sulfate (lower right). In all graphs, the samples are: a) Pure TiO_2 b) Co-TiO_2; c) Cu-TiO_2.

4.5 Photodegradation of Methylene Blue

The photoactivity of the samples was tested by monitoring the degradation of methylene blue (MB). Photocatalytic experiments were carried out by adding 2.0 mg of each TiO_2 sample to 16 mL of a MB aqueous solution (3.1×10^{-5} M). The samples were each placed in a quartz test tube and sonicated for 10 minutes to ensure complete MB coverage on TiO_2. After sonicating, the samples were covered and left undisturbed for 30 minutes. After this, the samples were placed in the rotating sample holder of the photochemical reaction chamber and irradiated with UV light. All samples were analyzed under the same reaction conditions at the following irradiation times: 0, 15, 30, 45, 60, 80, 115 and 160 minutes. After each irradiation cycle, solution was transferred by pipette to a quartz cuvette for analysis. The solutions were placed back into the quart test tubes after analysis for further irradiation.

Several samples were analyzed to determine how modifications, bulk and surface, to the TiO_2 photocatalysis would affect the photocatalytic degradation of MB. The samples tested were pure TiO_2, surface modified TiO_2, doped TiO_2 and a combination of the two types of modifications. Sulfate and phosphate (TiO_2-S and TiO_2-P) were the SMS used and cobalt and copper were the dopants used (Co-TiO_2 and Cu-TiO_2). The samples modified in combination were identified as Co-TiO_2-S, Co-TiO_2-P, Cu-TiO_2-S and Cu-TiO_2-P.

As the UV-Vis analysis of MB was conducted, the absorbance at 664 nm was measured. The electronic transition at 664 nm corresponds to the $n \rightarrow \pi^*$ electronic transition.[267] Since the initial concentration (c) and initial absorbance (A) values of MB are known, Beer's Law can be

$$A = \varepsilon bc \tag{4.1}$$

utilized to determine MB molar absorptivity (ε_{664nm}) via equation 4.1. In this work, the quartz cuvette used during UV-Vis analysis had a path length (b) of 1 cm and the initial concentration (c) of the MB was 3.1 x 10^{-5} M. Once the molar absorptivity is known for a sample, the absorbance values determined by UV-Vis analysis of that sample can be used to determine the corresponding analyte (MB) concentration. After completing the UV-Vis analysis, a comparative analysis of the activity of the samples was made by calculating the rate constant (k) for each sample. In order to determine the pseudo first order rate constant (k), a plot the absorbance values (λ=664 nm) vs.

$$\frac{C}{C_0} = e^{-kt} \tag{4.2}$$

irradiation times for each sample was fit to an exponential decay function (equation 4.2). In this equation, C is the concentration of MB at a given time and C_0 is the initial concentration of MB.

4.6 Photocatalytic Activity of TiO_2 Samples

Figure 4.6 shows the normalized spectra for all TiO_2 samples analyzed. It can be clearly seen in the analysis of all samples that the peak located at 664nm blue shifted as the time increased which indicates that the MB is being degraded by the demethylation pathway (see §1.5). The various intermediates produced during MB demethylation have electronic transitions of decreasing wavelengths, from 664 nm – 599 nm, until complete decomposition.[90, 268] Although there can be competing decomposition processes occurring, without further analysis, the demethylation pathway is likely dominant route taken.[269] It can also be seen in most samples

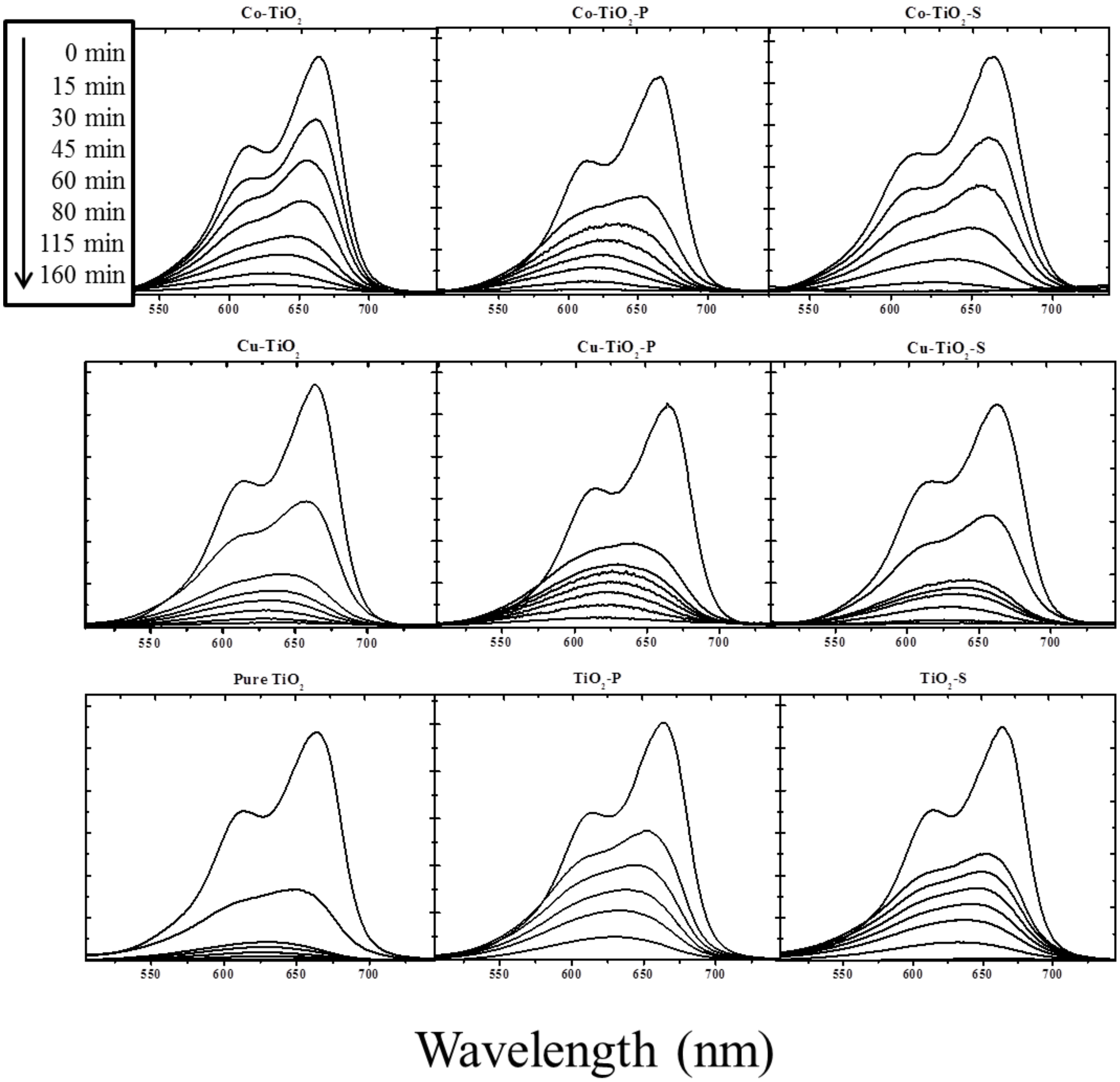

Figure 4.6: Normalized UV-Vis spectra of the photocatalytic degradation of MB over various TiO_2 samples.

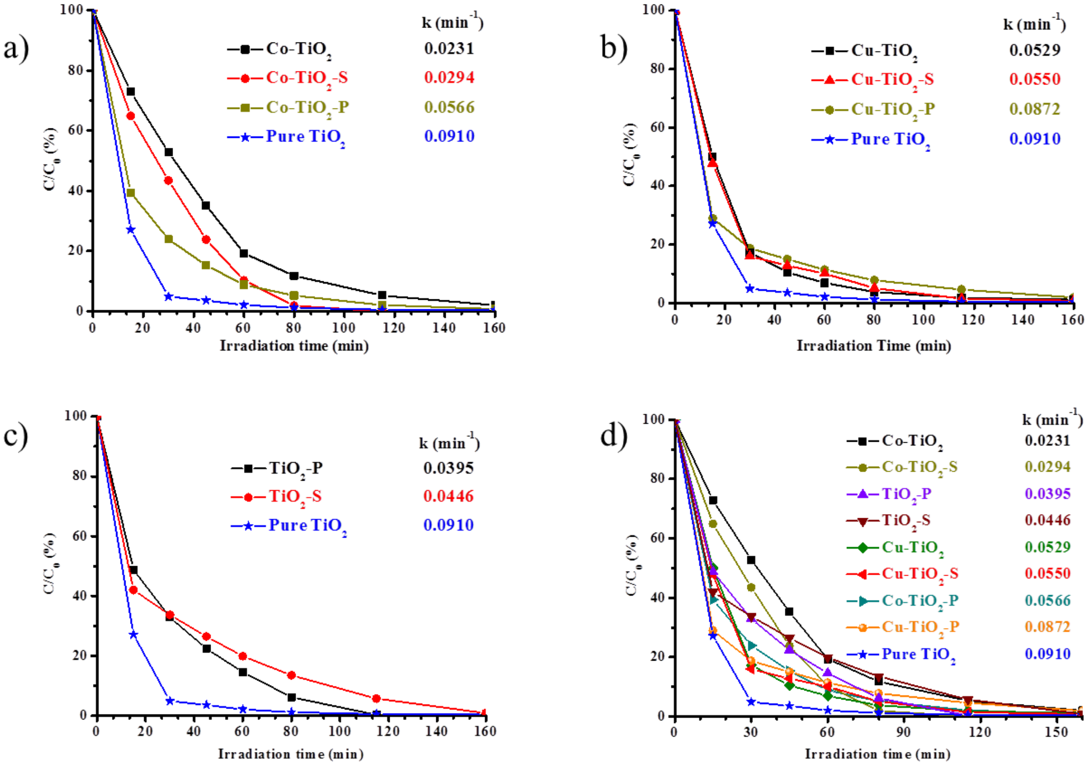

Figure 4.7: Photodecomposition rates of MB for: a) cobalt doped samples; b) copper doped samples; c) surface modified samples; d) all samples. Pure TiO$_2$ was included in all graphs.

that the majority of the MB absorbance values are significantly decreased within the first 30 minutes of exposure.

The rates of decomposition, listed in increasing order within each graph, are shown in figure 4.7. For comparative purposes, pure TiO_2 has been included in all the graphs. In figure 4.7 (a), the cobalt doped samples are shown. As a group, the cobalt doped samples showed the lowest overall activity. The copper doped samples, shown in 4.7 (b), have the highest overall activity. The samples with the surface modifications only, figure 4.7 (c), have rates that lie between the two previously mentioned groups. The rates of all samples are collectively shown in figure 4.7 (d). None of the samples analyzed possessed a higher activity than pure TiO_2. Of the doped samples, those with surfaces modified by the phosphate group showed a higher activity than those with sulfated surfaces.

The inferior activity of both Co-TiO_2 and Cu-TiO_2 when compared to pure TiO_2 can be attributed to parameters such as surface area, bulk defects, oxygen vacancies and the ability to create hydroxyl radicals.[219] Also, for a given metal, there is also an optimal amount of loading that is required to maximize photoactivity.[270, 271] When introduced into the bulk of a semiconductor, cationic metal dopants can increase photoactivity by trapping electrons in the conduction band (CB) and holes in the valence band (VB) which potentially leads to the formation of hydroxyl radicals (from surface adsorbed water) and superoxide radicals (from surface adsorbed O_2) respectively. If dopant concentrations are too high, the excess sites may exist as a recombination centers due to the proximity to other trapping sites which would decrease activity.[264] In principle, Cu-TiO_2 would have a greater number of oxygen vacancies than Co-TiO_2 because of Cu^{2+} larger atomic radius which causes a greater perturbation of the TiO_2 bulk structure.

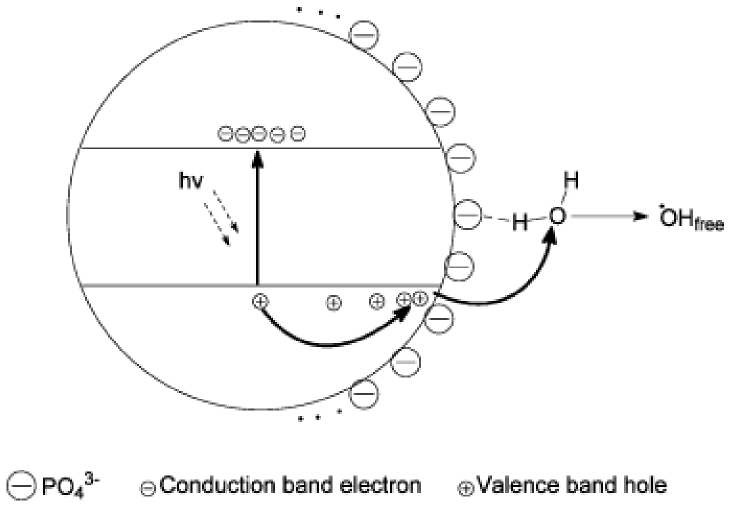

Figure 4.8: Reaction mechanism of photocatalytic degradation of surface modified TiO_2. Reproduced from ref. [276]

As for surface modification, acido ligands like sulfate and phosphate ions have relatively high symmetry in their free states. When coordinated to metals however, their symmetry is lowered based on the method of coordination.[141] Bidentate acido ligands, whether bridging or chelating, cause oxygen atoms to be in an electron deficient state. This electron deficient state is capable of trapping electrons which prevents recombination of electron/hole pairs generated by photoexcitation, thus increasing photocatalytic efficiency.[47, 264, 272] This seem to be validated by the data as the surface modified samples, whether doped or not, appear to generally have a higher degradation rate than samples with no surface modifications. The phosphate species shows a slight higher activity than the sulfated species. This could be due to bond strength. Surface reactions are what drive these catalytic systems[273] and both phosphates and sulfates readily accept surface protons with their exposed oxygen atoms. Although phosphates tend to be more strongly bound to TiO_2 than sulfates,[274, 275] they share a common reaction mechanism as shown in figure 4.8. This cartoon illustrates how the photogenerated hole in the valence band is electrostatically drawn to the particle interface by the surface adsorbed phosphate group. The surface bound phosphates freely facilitate the charge transfer of the hole to surface adsorbed water which produces hydroxyl groups.[276] Phosphates have shown the ability to be resistant to redox reactions as they have been effectively used as coupling agents, or anchoring groups, between TiO_2 and various chromophores in other works.[277, 278]

4.7 Conclusions

The samples utilized in this work were prepared very similarly to that of Mugundan and Tseng. The surface area determined in their studies were approximately 20-30 m^2/g, and the average crystallite sizes determined in this work matched very closely to the average crystallite sizes given in their works.[214, 270, 271]

It is well known that making modifications to TiO_2, whether doping or surface modifying, can affect photocatalytic activity. These modifications often affect the surface area which has been suggested to be one of the most important factors when analyzing photoactivity.[90, 279] When these two modifications are performed in combination, a totally different activity is observed. Doping TiO_2 appears to have a greater effect of photoactivity because it largely determines the bandgap energy. Analysis of the eight modified samples tested determined that the four most active samples were doped. The surface modified only samples were immediately behind with two of the three cobalt doped samples being the least active. The two most active modified samples were doped and had phosphates attached to the surface. It is believed that the combination of both the dopant atoms and surface adsorbed species augment each other to reduce electron/hole recombination which further enhances the photoefficiency. Although surface adsorbed species occupy surface sites, the oxygen substituents still allow for hydrogen bonding which is a necessary for the production of reactive oxygen species.

CHAPTER 5 - RAMAN SPECTROSCOPY ANALYSIS OF EL NIÑO IMPACT ON MOLLUSK BIOMINERALIZATION

5.1 Introduction

As previously mentioned in this dissertation, Raman spectroscopy can be a powerful tool when used to differentiate polymorphic phases. While XRD has been traditionally known as the standard for phase identification, Raman analysis proves advantageous to XRD in this work because of the coupled confocal microscope that allows for multiple points of analysis in micrometer increments along the cross-section of a biological/geological sample.

The samples used in this study were three mollusk seashells from the species *Trachycardium procerum,* a large infaunal cardioidean bivalve mollusk. (Note: infaunal refers to animal life associated with the sea floors/beds while cardioidean is associated with the taxonomy of saltwater clams.) These samples, from a group captured live in November 1984, survived the El Niño event of 1982-83 which is widely considered the strongest of the 20th century.[280] These small marine invertebrates, as well as many similar organisms, build up protective exoskeletons over time via mineralization that is governed by biological processes.[281] It is proposed that the shell's microstructure, which can be analyzed by Raman spectroscopy, shows variations that correspond to rapid environmental fluctuations to climate change, such as an El Niño event. If proven true, the Raman analysis of the microstructure of bivalve shells in conjunction with other currently used analysis methods such as isotope and radiocarbon data as well as trace element composition/ratio could potentially become a valuable tool in determining historical climate trends.[282]

5.2 Biomineralization

When solid structures are formed and integrated into biological systems upon interacting with essential elements from the local environment, a separate field of science known as biomineralization is introduced. Biomineralization, as defined by Mann, is the study of the formation, structure and properties of inorganic solids deposited in biological systems.[283] This process is versatile in that large and small as well as hard and soft inorganic-organic hybrid structures can be produced. Calcium carbonate, calcium phosphate, silica and iron oxides are among the many types of molecules that result from biomineralization. These materials are significant to many areas of science and have garnered much attention in recent years as a result. Biologist can gain insight into evolutionary changes from the fossil records that often remain embedded as calcification occurs after millions of years. Chemists study these materials to develop a better understanding of the interaction between inorganic atoms and extended organic networks. Materials engineers tend to use these materials as templates when designing new composites aimed at serving a particular function. As is the case with this study, geologist can use the microstructure of these materials to generate historical climate trends.

5.3 Calcium Carbonate

Living organisms require a number of essential elements for life. Of these elements, calcium is known as the most common and widespread among skeletal structures (bones, teeth, shells, etc.). Two calcium compounds, calcium carbonate and calcium phosphate, are among the most recognized in biomineralized samples as they possess high lattice energies and low solubilities which lends to their thermodynamic stability in most biological environments.[283] Calcium carbonate, the focus of this work, exists in the form of six different polymorphs: calcite, aragonite, vaterite, calcium carbonate monohydrate, calcium carbonate, hexahydrate and amorphous calcium carbonate. Of these phases, aragonite and calcite are predominately used as biominerals due their thermodynamic stability. Their crystal structures can be seen in figure 5.1.[284] There are cases where both polymorphs exhibit common functionalities such as exoskeleton and protection, yet there are some variations as calcite aids in optical imaging and mechanical strength while aragonite plays a role in reproduction, buoyancy and gravity receptors.[283]

5.4 El Niño Phenomenon

The natural phenomenon known as El Niño generally refers to equatorial pacific water temperatures. As shown in figure 5.2, El Niño is mainly characterized by unusually warm ocean temperatures; unlike La Niña which refers to unusually cool ocean temperatures.[285] During normal, non-El Niño conditions, warmer surface water is ushered westward by trade winds blowing from east to west. The water surface has been measured as much as 0.5 meters higher in the western pacific than the eastern side as a result of this action. As the eastern surface waters

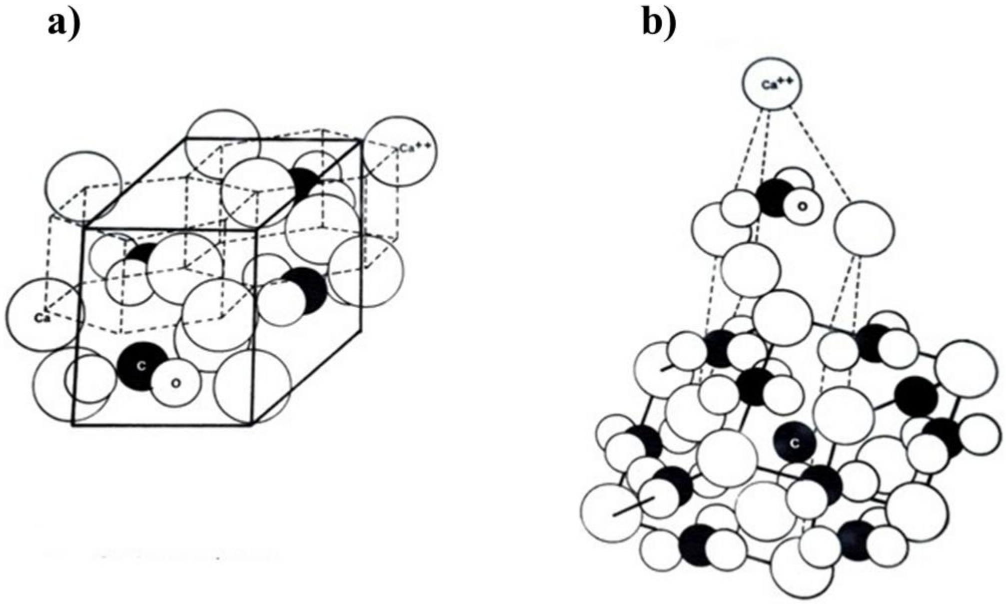

Figure 5.1: Two most prevalent calcium carbonate phases as observed in biomineralized samples: a) calcite and b) aragonite; modified from ref. [284]

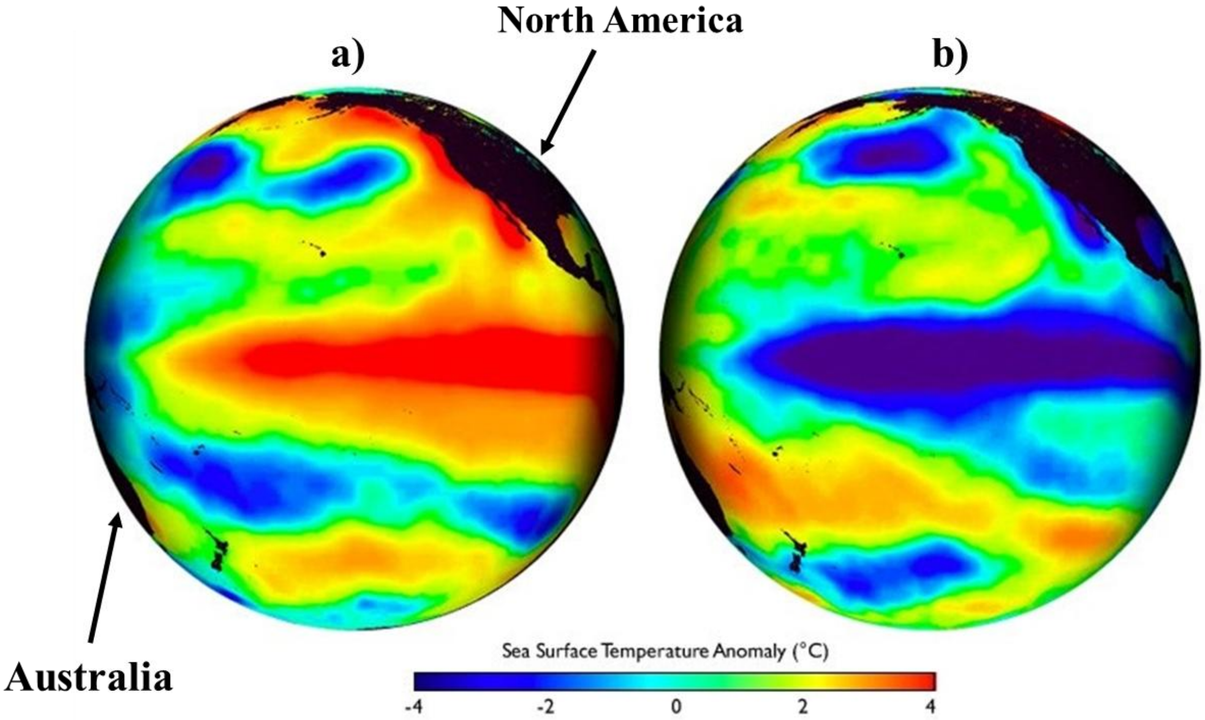

Figure 5.2: Cartoon depicting the pacific ocean and the general temperature deviation from averages during a) El Niño conditions and b) La Niña conditions; modified from ref. [285]

are displaced westward, the upwelling of cooler water from the greater depths reaching the surface brings with it an abundance of nutrients that are essential to many diverse marine ecosystems. The cooler nutrient-rich water bolsters marine productivity, including marine fisheries that are a major part of regional economic stability. As rainfall is predominately found in rising air above the warmest water, normal non-El Niño conditions causes a rainy western Pacific and a relatively dry eastern Pacific.[286]

As El Niño conditions occur, the upwelling of cooler nutrient-rich water in the eastern pacific is greatly reduced due to decreased trade winds that normally displace surface water towards that west. The resulting warmer nutrient-poor water remains in the eastern pacific and seriously impacts the lower food chain's productivity, and this subsequently impacts the upper food chain. The cooler waters of the western pacific deter rainfall and often leads to drought conditions. As the atmospheric heat and warmer water temperatures are displaced, large scale changes in jet streams, or global atmospheric circulation, occur. As these changes occur, weather anomalies and uncommon climatic conditions can arise in regions far away from the equatorial pacific areas.

For the purposes of this work, it is worth noting that the El Niño conditions of 1982-1983 was widely acknowledged as the most prominent of the twentieth century until superseded by the 1997 occurrence. During the 1982-1983 occurrence, the maximum sea surface temperature (SST) reached as high as 10 °C above the average.[287]

5.5 Experimental Methods

The shell samples used in this experiment were collected by commercial divers off the coast of Peru in November 1984. There were three different specimens used in this study with the shell labeled as 2TP4-2 served as the reference. Sample 2TP4-2 was previously subjected to a battery of test that allows for the boundaries within the shell structure to correspond with the onset of El Niño conditions with a high degree of certainty.[288] The three "zones" analyzed on the samples correspond to before, during and after the El Niño event of 1982-1983. For a complete synopsis of background information and other characterization methods, see the work published by Perez-Huerta, et al.[281]

Aside from the previously mentioned reference sample, two other samples were analyzed via Raman spectroscopy in this work, 2TP4-3 and 2TP4-4. The samples were individually prepared for analysis by washing with ultrapure water then air-dried. Samples were then embedded and polished and taken for Raman analysis.[281] Once received, no further preparations were need for analysis via Raman spectroscopy. The Jobin Yvon LabRam HR800UV confocal microscope was used to perform the analysis. The system utilized an Ar-ion laser with an excitation of 514 nm (green) and a 50x objective lens.

5.6 Microstructure Characterization

Both shells were analyzed along the cross-section independently in each of the three zones as shown in figure 5.3. The three zones that appear within the images correspond to before (a), during (b) and after (c) the 1982-1983 El Niño events. Both samples appear to be the aragonite polymorph of calcium carbonate as determined by the second of the two low

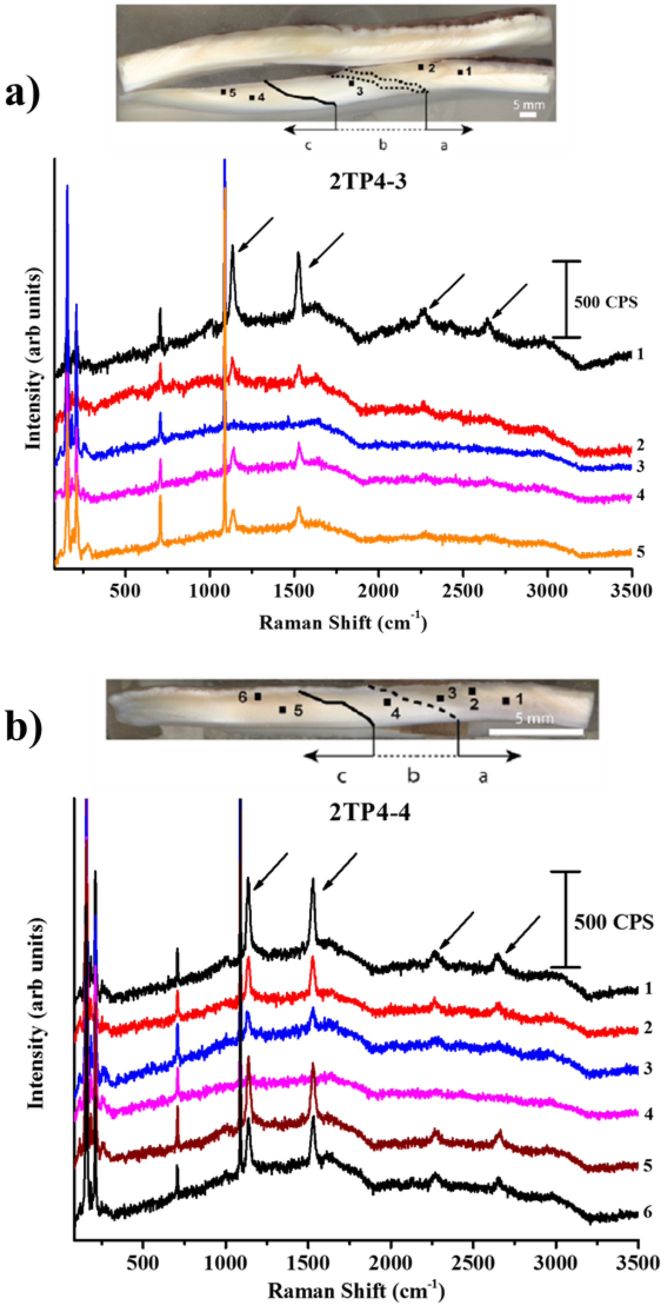

Figure 5.3: Raman analysis of calcium carbonate bivalve shells a) 2TP4-3 and b) 2TP4-4 before, during and after (shown as a, b and c respectively in the inset images) the 1982-1983 El Niño conditions. Features identified by arrows are indicative of organic polyene molecules that are associated with pigment-protein complexes, 1135 cm^{-1}, 1523 cm^{-1}, 2270 cm^{-1} and 2645 cm^{-1}. These organic features disappear during the El Niño event but are present both before and after the maximum SST. Reproduced with permission from ref. [281]

Raman Analysis		
Raman Shift (cm^{-1})	**Literature Value (cm^{-1})**	**Band Assignment**
161	158.0	CO_3^{-2} lattice mode[289]
284	283.0	$CO3^{-2}$ lattice mode[289]
707	713.0	ν_4 (CO_3^{-2}) antisymmetric bend[290]
1088	1089.0	ν_1 (CO_3^{-2}) symmetric stretch[291]
1135	1135.0	ν_1 C-C single bond[292, 293]
1523	1519.0	ν_1 C=C double bond[292, 293]
2266	2270.0	ν_2 overtone band[292, 293]

Table 5.1: Observed Raman vibrational modes and their respective characterizations of samples 2TP4-3 and 2TP4-4

wavenumber features (161 cm^{-1} and 284 cm^{-1}) which are carbonate lattice vibrations (see table 5.2).[289] The features at 707 cm^{-1} and 1089 cm^{-1} are assigned as carbonate antisymmetric bend and symmetric stretch modes respectively.[290, 291] The remaining features, identified by arrows in figure 5.3, are related to polyene molecules that are linked with carbonate biomineral structures and are known as chromo-proteins, or pigment-protein complexes.[293-295] As shown in the inset images of figure 5.3, these peaks are present in the zones corresponding to a) before and c) after the El Niño events but disappear during the maximum SST. The vibrational modes assigned to the peaks are as follows: 1135 cm-1 (ν_1 C-C single bond); 1523 cm-1 (ν_1 C=C double bond); 2270 cm-1 (ν_2 overtone band); and 2645 cm-1 (ν_1 and ν_2 combination band).[292, 293]

5.7 Discussion and Conclusions

The calcium carbonate phase of the shells appeared to remain consistent throughout the lifetime of this El Nino event. The organic content did not remain consistent throughout however. It is well known that the abundance and availability of lipids, proteins, carbohydrates, trace elements, etc… all play a role in the formation of biominerals. In this specific case, it is evident that the El Nino event did not prevent the growth of the shell, but it did change the growth mechanism and the content of the calcium carbonate shell. Other analysis methods in this work aimed to address this question as electron probe mapping and laser ablation inductively-coupled mass spectrometry was used to try to determine the location, atomic content as well as atomic percentages of trace elements present.

Raman microscopy alone is sufficient for shell analysis for the purpose determining the polymorph present, but it can only suggest the possible mechanism in which the organisms construct their shells. Some studies suggest that amorphous calcium carbonate (ACC) plays a role in precipitating crystals, but Raman analysis uncovered no ACC anywhere along the sample.[296] Because ACC has a separate and distinct structure than other calcium carbonate phases, Raman microscopy can be used to thoroughly examine the shell in micrometer increments in hopes of detecting small amounts of another phase of the material. Only after a very detailed analysis of the organism's immediate environment before, during and after an El Nino event can a determination of the mechanism of bivalve mollusk be concluded.

The versatility of Raman microscopy allows the point by point analysis of a sample without complicated sample preparation methods. By using the coupled confocal microscope, sample analysis was able to occur along the transition zones where there was a clear visible change in the microstructure of the shell. Phase content could be extracted fairly quickly and accurately. While the intense laser beam from the Raman's excitation source can be destructive, the calcium carbonate shells as well as their sample housing handled the beam without problems.

CHAPTER 6 - CONCLUSIONS

6.1 This Work

The work presented in this dissertation describes how making modifications to the surface of TiO_2 can provide polymorph stability and potentially enhance its photocatalytic activity. TiO_2 and the materials utilized to make the modifications are fairly low cost and non-toxic.

6.1.1 Synthesis

There are many synthetic routes available to produce TiO_2. The sol-gel method was utilized in this work because it allows for the most flexibility with respect to many of the reaction parameters. The room temperature, ambient atmosphere and aqueous based reactions allowed for the simplicity of synthesizing, waste disposal and sample handling. The use of titanium alkoxides was preferred over other titanium precursors. Titanium (IV) isopropoxide proved to possess the best combination of cost efficiency and stability in ambient conditions.

When utilizing a sol-gel method, aging time can make a significant difference in the product obtained. As the sample is allowed to age in the reaction mixture, a combination of amorphous, anatase and brookite TiO_2 has been shown to result. Samples have proven to be shelf stable and retain their polymorphic phase as long as they were properly dried, sealed in an air tight container and kept away from any heat sources.

6.1.2 TiO_2 Phase Transition

It has been demonstrated in this work that surface modification of TiO_2 with phosphate and silicate species increased the TiO_2 PTT beyond the literature accepted values of pure TiO_2. The carboxylate and sulfate species appeared to have no effect on PTT. The extent to which the temperature of the surface modified samples can be elevated before undergoing an irreversible change was dependent upon the thermal stability of the surface adsorbate. TiO_2 phase transformation is a reconstructive process in which both surface and bulk atoms rearrange themselves. The structural changes that result include alterations of the lattice parameters as well as the density of the unit cells.

6.1.3 Photocatalytic Activity

The purpose of the photocatalytic study in this work was to determine if applying two different commonly used modification methods to TiO_2 would affect its photocatalytic activity. While there was no definitive trend, the data did suggest that the activity was different from the activity of TiO_2 with a single modification or no modification at all. Most studies performed on doped TiO_2 samples are aimed at utilizing visible light as the excitation source unlike the UV light source used in this work.

In this work, as many as possible experimental conditions were kept uniform as to try to make a comparative analysis of the activity of the samples. While many of the experimental parameters were not tailored for optimal photoefficiency, a general idea of the effect of dual modifications of the samples was desired. Typically, reaction conditions such as dopant concentration, pH of the reaction solution, TiO_2 particle size, annealing temperature, synthesis reaction time, catalyst loading and initial dye concentration are all meticulously determined before comparing its activity to other high activity pure TiO_2 samples (ie. Degussa P25).

The general conclusion gathered from this work is that the photoactivity follows the general trend (from greatest to least) of doped and surface modified, doped, then surface modified. The surface area, within a 10 m^2/g range, was estimated by matching sample's synthesis and preparation conditions with experiments perform by other researchers.

6.1.4 Raman Analysis of Biomineralization

Raman spectroscopy was used to analyze various reconstruction processes in the seashell of mollusk. The ability of Raman to detect various polymorphs associated with calcium carbonate proved invaluable in this work. Rapid environmental changes induce changes in the amorphous calcium carbonate microstructure of the shells. The ability of Raman to analyze the centimeter sized samples in micrometer increments allowed for the thorough analysis of each sample. By analyzing the microstructure of fossilized and recent samples before, during and after a known El Nino event, a historical record of rapid environmental changes can be determined.

6.2 Future Works

6.2.1 Temperature Programmed Desorption

The surface modified TiO_2 samples had their phase transition temperature (PTT) altered by surface adsorbed species. Samples that could survive the elevated temperature that is required for phase transition proved to be the ones that increased TiO_2 PTT. Temperature programmed desorption would be advantageous because it would give a more precise determination of the temperature at which the surface adsorbed species is desorbed.

6.2.2 Differential Scanning Calorimetry

In this work, XRD was used to give a general range of the PTT for TiO_2. A more precise method of determining the PTT is to use differential scanning calorimetry (DSC). This technique measures the heat flow of a sample as a function temperature. As phase transitions occur, there is an exotherm in the DSC spectrum. The area under this exothermic peak can be used to determine the degree of crystallization of the sample. DSC analysis can also be used to determine the energy difference associated with the change in A-R phase transition. DSC studies were attempted in this work, but neither the system nor the sampling equipment were equipped to accommodate the temperatures needed for this work.

6.2.3 Kinetics of Surface Modified TiO_2 Phase Transition

Detailed experiments regarding the kinetics of the A-R phase transition needs to be performed. The ability of surface modifications to hinder A-R phase transition also means that the energetics involved in the reaction changes. A series of experiments that monitors the percentage of anatase to rutile as the samples are annealed both above and below the phase transition temperature would allow for the determination of the activation energy of the various samples (via the Arrhenius equation). Due to average crystallite sizes, Raman analysis would be far superior to XRD for determining both quantitatively and qualitatively the phase of TiO_2 present. From a known mixture of anatase and rutile, integration of the area under the most intense Raman features of each phase would allow for the determination of the ratio of anatase to rutile present.

6.2.4 Synthesis of Mixed Brookite-Anatase TiO_2

The synthesis of doped TiO_2 via a sol-gel method was shown to produce a mixture of mostly amorphous and trace amounts of anatase phases when the reaction synthesis was performed in a continuous fashion (as described in §4.2). When the reaction was allowed to age (left in solution phase without stirring) for ~ 48 hours, a mixture of brookite and anatase phases resulted. Raman analysis showed the presence of brookite and anatase in the as prepared sample (as shown in figure 6.1). After heating to 400 °C, the more pronounced Raman features observed indicated that the average crystallite sizes increased as well as the degree of crystallinity. XRD analysis needs to be performed to determine the percent composition of brookite to anatase. Scherrer analysis can also be applied to XRD analysis to determine average crystallite sizes. Further experimentation is needed to determine what contribution aging time and metal cations play in the stabilization of brookite in a synthetic procedure not normally known for producing this polymorph.[104-106]

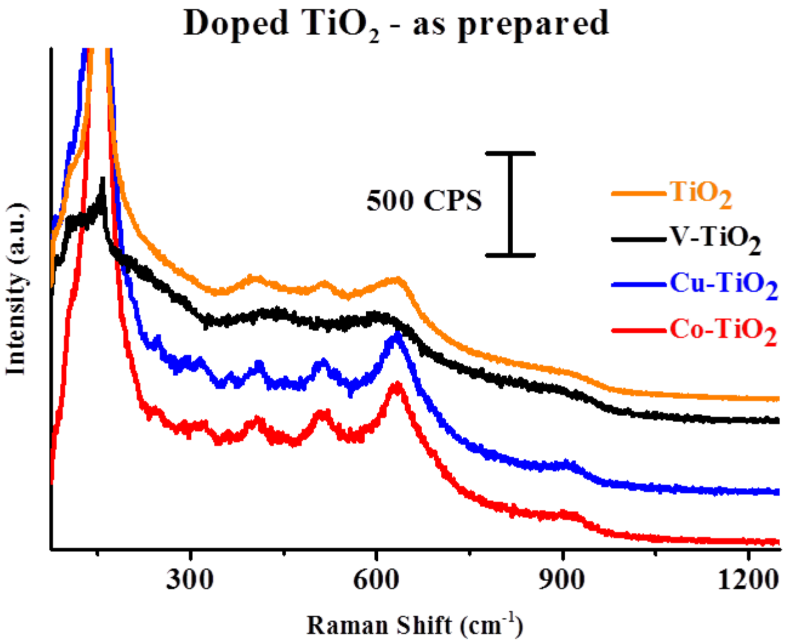

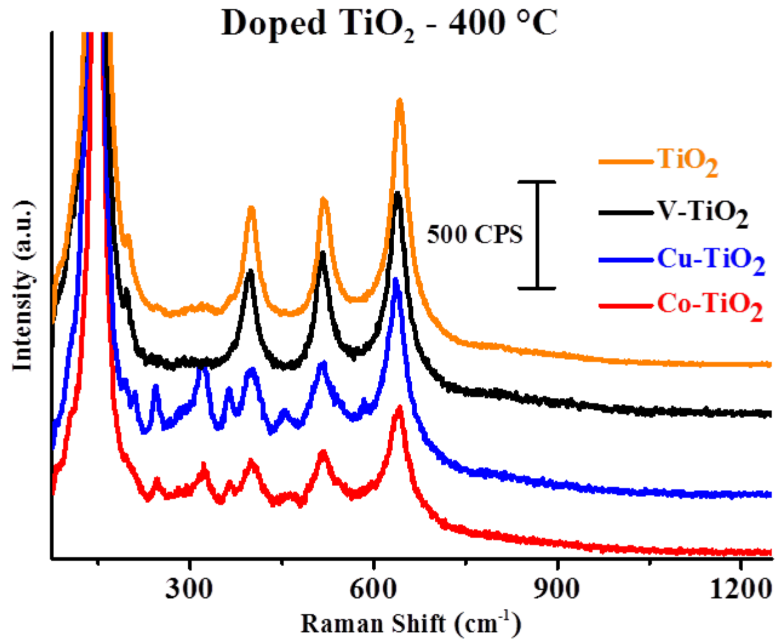

Figure 6.1: Raman analysis of as prepared (upper) and 400 °C (lower) TiO_2 produced via a sol-gel method. In both graphs, pure TiO_2 and V-TiO_2 contained pure anatase whereas Cu-TiO_2 and Co-TiO_2 produced a brookite/anatase mixture.

6.2.5 BET Studies

A major factor when examining the photocatalytic behavior of a photocatalytic system is the surface area. When considering that reactions occur at surfaces, the greater the surface area the higher activity the particle tends to have. The surface area of a sample is the main property that allows one to make the comparison between the efficiency of various photocatalysts.

6.2.6 Point of Zero Charge

In solution the surface of TiO_2 particles has exposed oxygens that can be protonated. The pH value at which surface charge of the particles is zero is known as the point of zero charge (PZC). If the TiO_2 surface has a charge, it will exhibit electrostatic interactions with other charged particles as well as any other species in solution such as analyte molecules. It is important to determine the PZC so that accurate pH values of TiO_2 solutions can be obtained.

6.2.7 Mass Spectrometry

In order to better understand the photocatalytic induced degradation of molecular dyes, some type of mass spectrometry analysis would be required. For this experiment qualitative analysis would be more important than quantitative analysis. As the rather large molecular dyes are degraded by photons, the byproducts produced will give insight into the reaction mechanism responsible for degradation.

6.2.8 Optimal Conditions for Photocatalytic Degradation

In this work, there were four different TiO_2 samples that had the combination of bulk and surface modifications. For each sample, the optimal conditions for photocatalytic degradation would need to be determined. These reaction conditions (as mentioned in §6.1.3) are dopant concentration, pH of reaction solution, TiO_2 particle size, catalyst loading and initial dye concentration. TiO_2 samples are normally doped with the intention of shifting the band gap energy to the visible range. Given such, the utilization of doped samples suggests that a visible excitation source be used to determine the long term viability of these dual modified particles.

6.2.9 Other Target Molecules

This work focused solely on MB as the analyte molecule. MB has been well studied and its degradation pathways are well known. There are many other analyte molecules such as cresol red, methyl orange, and 4-chlorophenol that have been used in literature. The structural differences in these analytes would prevent the photoactivity of a specific TiO_2 sample from being the same from analyte to analyte.[297]

REFERENCES

1. McCrone, W. C., 1500 Forgeries. *The Microscope* **1990,** *38*, 289-298.

2. Fitzhugh, E. W., *Artists' Pigments: A Handbook of Their History and Characteristics*. 3 ed.; National Gallery of Art: Oxford, 1997; Vol. 3, p 295-355.

3. Margerison, T., The Future of Titanium. *New Sci.* **1958,** *4* (82), 156-158.

4. Fujishima, A. and Honda, K., Electrochemical Photolysis of Water at a Semiconductor Electrode. *Nature* **1972,** *238* (5358), 37-38.

5. Price, D., Energy and human evolution. *Population and Environ.* **1995,** *16* (4), 301-319.

6. Fichman, B. T., Monthly Energy Review July 2015. U. S. D. o. Energy, Ed. U.S. Energy Information Administration: 2015.

7. Morton, O., Solar energy: A new day dawning?: Silicon Valley sunrise. *Nature* **2006,** *443* (7107), 19-22.

8. Wayne, C. E. and Wayne, R. P., *Photochemistry*. Oxford University Press: New York, 1996; p 1-88.

9. Nakamoto, K., *Infrared and Raman Spectra of Inorganic and Coordination Compounds Part A: Theory and Applications in Inorganic Chemistry*. 5th ed.; John Wiley & Sons, Inc.: New York, 1997; p 387.

10. Huheey, J. E.; Keiter, E. A.; et al., *Inorganic Chemistry: Principles of Structure and Reactivity*. 4th ed.; HarperCollins College Publishers: New York, 1993; p 964.

11. Semiconductors/What is a semiconductor. http://en.wikibooks.org/wiki/Semiconductors/What_is_a_Semiconductor (accessed Janurary 17, 2014).

12. Reference Solar Spectral irradiance: ASTM G-173. http://rredc.nrel.gov/solar/spectra/am1.5/ASTMG173/ASTMG173.html (accessed March 27, 2014).

13. Dupont© Titanium Technologies. http://www2.dupont.com/Titanium_Technologies/en_US/ (accessed March 27, 2013).

14. Weir, A.; Westerhoff, P.; et al., Titanium Dioxide Nanoparticles in Food and Personal Care Products. *Environ. Sci. Technol.* **2012,** *46* (4), 2242-2250.

15. ICIS. Titanium Dioxide (TiO_2) Uses and Market Data 2010. http://www.icis.com/Articles/2007/11/07/9076546/titanium-dioxide-tio2-uses-and-market-data.html (accessed March 27, 2013).

16. Abundance in Earth's Crust of the Elements 2010. http://www.periodictable.com/Properties/A/CrustAbundance.v.log.wt.html (accessed March 28, 2013).

17. Blake, D. M.; Maness, P.-C.; et al., Application of the Photocatalytic Chemistry of Titanium Dioxide to Disinfection and the Killing of Cancer Cells. *Sep. Purif. Rev.* **1999,** *28* (1), 1-50.

18. Abbaszadegan, M.; Hasan, M. N.; et al., The disinfection efficacy of a point-of-use water treatment system against bacterial, viral and protozoan waterborne pathogens. *Water Res.* **1997,** *31* (3), 574-582.

19. Sung, W.; Tsai, T.; et al., Removal of Indoor Airborne Bacteria by Nano- as Photocatalyst: Feasibility Study in Museum and Nursing Institutions. *J. Environ. Eng.* **2011,** *137* (3), 163-170.

20. Fujishima, A.; Rao, T. N.; et al., Titanium dioxide photocatalysis. *J. Photochem. Photobio., C* **2000,** *1* (1), 1-21.

21. Ganesh, V. A.; Raut, H. K.; et al., A review on self-cleaning coatings. *J. Mater. Chem.* **2011,** *21* (41), 16304-16322.

22. Augugliaro, V.; Camera-Roda, G.; et al., Heterogeneous Photocatalysis and Photoelectrocatalysis: From Unselective Abatement of Noxious Species to Selective Production of High-Value Chemicals. *J. Phys. Chem. Lett.* **2015,** *6* (10), 1968-1981.

23. Carre, A.; Roger, F.; et al., Study of acid/base properties of oxide, oxide glass, and glass-ceramic surfaces. *J. Colloid Interface Sci.* **1992,** *154* (1), 174-183.

24. Kikuchi, Y.; Sunada, K.; et al., Photocatalytic bactericidal effect of TiO_2 thin films: dynamic view of the active oxygen species responsible for the effect. *J. Photochem. Photobio., A* **1997,** *106* (1-3), 51-56.

25. Smart, L. and Moore, E., *Solid State Chemistry*. Chapman & Hall: London, 1992; p 292.

26. Dubrovinskaia, N. A.; Dubrovinsky, L. S.; et al., Experimental and Theoretical Identification of a New High-Pressure TiO_2 Polymorph. *Phys. Rev. Lett.* **2001,** *87* (27), 275501.

27. Diebold, U., The surface science of titanium dioxide. *Surf. Sci. Rep.* **2003,** *48* (5-8), 53-229.

28. Woodley, S. M. and Catlow, C. R. A., Structure prediction of titania phases: Implementation of Darwinian versus Lamarckian concepts in an Evolutionary Algorithm. *Comput. Mater. Sci.* **2009,** *45* (1), 84-95.

29. Grant, F. A., Properties of Rutile (Titanium Dioxide). *Rev. Mod. Phys.* **1959,** *31* (3), 646-674.

30. Lee, B. I.; Wang, X.; et al., Synthesis of brookite TiO_2 nanoparticles by ambient condition sol process. *Mater. Lett.* **2006,** *60* (9-10), 1179-1183.

31. Balachandran, U. and Eror, N. G., Raman spectra of titanium dioxide. *J. Solid State Chem.* **1982,** *42* (3), 276-282.

32. Orendorz, A.; Brodyanski, A.; et al., Structural transformations in nanocrystalline anatase TiO_2 films upon annealing in air. *Surf. Sci.* **2006,** *600* (18), 4347-4351.

33. Ambrus, Z.; Mogyorósi, K.; et al., Low temperature synthesis, characterization and substrate-dependent photocatalytic activity of nanocrystalline TiO_2 with tailor-made rutile to anatase ratio. *Appl. Catal., A* **2008,** *340* (2), 153-161.

34. Egerton, T., The Influence of Surface Alumina and Silica on the Photocatalytic Degradation of Organic Pollutants. *Catalysts* **2013,** *3* (1), 338.

35. Sun, J.; Gao, L.; et al., Synthesizing and Comparing the Photocatalytic Properties of High Surface Area Rutile and Anatase Titania Nanoparticles. *J. Am. Ceram. Soc.* **2003,** *86* (10), 1677-1682.

36. Perera, S. and Gillan, E. G., A facile solvothermal route to photocatalytically active nanocrystalline anatase TiO_2 from peroxide precursors. *Solid State Sci.* **2008,** *10* (7), 864-872.

37. Titanium Tetrachloride Production by the Chloride Ilmenite Process. United States Environmental Protection Agency, Office of Solid Waste: 1995.

38. Bradley, D. C.; Chatterjee, A. K.; et al., Sexavalent compounds of uranium-I: Uranyl alkoxides and uranium hexa-alkoxides. *J. Inorg. Nucl. Chem.* **1959,** *12* (1-2), 71-78.

39. Bradley, D. C.; Thornton, P.; et al., 33 - ZIRCONIUM AND HAFNIUM. In *The Chemistry of Titanium, Zirconium and Hafnium*, Pergamon: 1973; pp 419-490.

40. Martin, R. L. and Winter, G., The association of n-tetra-alkoxy- and n-alkoxy-chloroderivatives of titanium. *J. Chem. Soc.* **1961,** (0), 2947-2957.

41. Yoldas, B. E., Modification of polymer-gel structures. *J. Non-Cryst. Solids* **1984,** *63* (1-2), 145-154.

42. Yoldas, B. E., Hydrolysis of titanium alkoxide and effects of hydrolytic polycondensation parameters. *J. Mater. Sci.* **1986,** *21* (3), 1087-1092.

43. Yoldas, B. E., Introduction and effect of structural variations in inorganic polymers and glass networks. *J. Non-Cryst. Solids* **1982,** *51* (1), 105-121.

44. Nikkanen, J.-P.; Kanerva, T.; et al., The effect of acidity in low-temperature synthesis of titanium dioxide. *J. Cryst. Growth* **2007,** *304* (1), 179-183.

45. Tian, G.; Fu, H.; et al., Synthesis and photocatalytic activity of stable nanocrystalline TiO_2 with high crystallinity and large surface area. *J. Hazard. Mater.* **2009,** *161* (2-3), 1122-1130.

46. Wang, Z.-c.; Chen, J.-f.; et al., Preparation of nanocrystalline TiO_2 powders at near room temperature from peroxo-polytitanic acid gel. *Mater. Lett.* **2000,** *43* (3), 87-90.

47. Ramadan, A. R.; Yacoub, N.; et al., The effect of phosphate anions on surface and acidic properties of TiO_2 hydrolyzed from titanium ethoxide. *Colloids Surf., A* **2009,** *352* (1-3), 118-125.

48. Aarik, J.; Aidla, A.; et al., Characterization of titanium dioxide atomic layer growth from titanium ethoxide and water. *Thin Solid Films* **2000,** *370* (1-2), 163-172.

49. Kim, C.-S.; Kwon, I.-M.; et al., Synthesis and particle size effect on the phase transformation of nanocrystalline TiO_2. *Mater. Sci. Eng., C* **2007,** *27* (5-8), 1343-1346.

50. Svadlak, D.; Shanelova, J.; et al., Nanocrystallization of anatase in amorphous TiO_2. *Thermochim. Acta* **2004,** *414* (2), 137-143.

51. Gribb, A. and Banfield, J., Particle size effects on transformation kinetics and phase stability in nanocrystalline TiO_2. *Am. Mineral.* **1997,** *82*, 717-728.

52. Hench, L. L. and West, J. K., The sol-gel process. *Chem. Rev.* **1990,** *90* (1), 33-72.

53. Zaban, A.; Aruna, S. T.; et al., The Effect of the Preparation Condition of TiO_2 Colloids on Their Surface Structures. *J. Phys. Chem. B* **2000,** *104* (17), 4130-4133.

54. Dunphy Guzman, K. A.; Finnegan, M. P.; et al., Influence of Surface Potential on Aggregation and Transport of Titania Nanoparticles. *Environ. Sci. Technol.* **2006,** *40* (24), 7688-7693.

55. Pettibone, J. M.; Cwiertny, D. M.; et al., Adsorption of Organic Acids on TiO_2 Nanoparticles: Effects of pH, Nanoparticle Size, and Nanoparticle Aggregation. *Langmuir* **2008,** *24* (13), 6659-6667.

56. Li, J.-G.; Ishigaki, T.; et al., Anatase, Brookite, and Rutile Nanocrystals via Redox Reactions under Mild Hydrothermal Conditions: Phase-Selective Synthesis and Physicochemical Properties. *J. Phys. Chem. C* **2007,** *111* (13), 4969-4976.

57. Reyes-Coronado, D.; Rodriguez-Gattorno, G.; et al., Phase-pure TiO_2 nanoparticles: anatase, brookite and rutile. *Nanotechnology* **2008,** *19* (14), 145605.

58. Anajafi, Z.; Marandi, M.; et al., Hydrothermal synthesis of TiO_2 nanocrystals in different basic pHs and their applications in dye sensitized solar cells. *Phys. E (Amsterdam, Neth.)* **2015,** *70*, 113-120.

59. Wang, D.; Yu, R.; et al., Hydrothermal Synthesis and Characterization of a Novel One-Dimensional Titanium Glycolate Complex Single Crystal: $Ti(OCH_2CH_2O)_2$. *Chem. Mater.* **1999,** *11* (8), 2008-2012.

60. Li, Q.; Liu, B.; et al., Ethylene glycol-mediated synthesis of nanoporous anatase TiO_2 rods and rutile TiO_2 self-assembly chrysanthemums. *J. Alloys Compd.* **2009,** *471* (1-2), 477-480.

61. Yang, H. G.; Liu, G.; et al., Solvothermal Synthesis and Photoreactivity of Anatase TiO_2 Nanosheets with Dominant {001} Facets. *J. Am. Chem. Soc.* **2009,** *131* (11), 4078-4083.

62. Li, T.; Tian, B.; et al., Facile Tailoring of Anatase TiO_2 Morphology by Use of H_2O_2: From Microflowers with Dominant {101} Facets to Microspheres with Exposed {001} Facets. *Ind. Eng. Chem. Res.* **2013,** *52* (20), 6704-6712.

63. Chang, S.-m. and Liu, W.-s., The roles of surface-doped metal ions (V, Mn, Fe, Cu, Ce, and W) in the interfacial behavior of TiO_2 photocatalysts. *Appl. Catal., B* **2014,** *156-157* (0), 466-475.

64. Zhao, W.; Chen, C.; et al., Photodegradation of Sulforhodamine-B Dye in Platinized Titania Dispersions under Visible Light Irradiation: Influence of Platinum as a Functional Co-catalyst. *J. Phys. Chem. B* **2002,** *106* (19), 5022-5028.

65. Wu, J. C. S. and Cheng, Y.-T., In situ FTIR study of photocatalytic NO reaction on photocatalysts under UV irradiation. *J. Catal.* **2006,** *237* (2), 393-404.

66. Zaleska, A., Doped-TiO_2: A Review. *Recent Pat. Eng.* **2008,** *2*, 157-164.

67. Yu, Y.-Y. and Gong, X.-Q., Unique adsorption behaviors of carboxylic acids at rutile TiO_2(110). *Surf. Sci.* **2015,** *641*, 82-90.

68. Wang, X.; Zhao, H.; et al., Visible light photoelectrocatalysis with salicylic acid-modified TiO_2 nanotube array electrode for p-nitrophenol degradation. *J. Hazard. Mater.* **2009,** *166* (1), 547-552.

69. Yu, J. C.; Zhang, L.; et al., Synthesis and Characterization of Phosphated Mesoporous Titanium Dioxide with High Photocatalytic Activity. *Chem. Mater.* **2003,** *15* (11), 2280-2286.

70. Diebold, U. and Madey, T. E., Supression of electron-induced positive ion emission by a molecular overlayer: Ion-molecule charge exchange at a surface. *Phys. Rev. Lett.* **1994,** *72* (7), 1116-1119.

71. Warburton, D. R.; Purdie, D.; et al., NEXAFS fingerprinting of TiO_2(110)-SO_2. *Surf. Sci.* **1992,** *269/270*, 305-309.

72. Hiroshi Onishi and Ken-ichi Fukui and Yasuhiro, I., Space-Correlation Analysis of Formate Ions Adsorbed on TiO_2 (110). *Jpn. J. Appl. Phys.* **1999,** *38* (6S), 3830.

73. Vogtenhuber, D.; Podloucky, R.; et al., Ab initio and experimental studies of chlorine adsorption on the rutile TiO_2 (110) surface. *Phys. Rev. B: Condens. Matter Mater. Phys.* **2002,** *65* (12), 125411.

74. Gerischer, H.; Michel-Beyerle, M. E.; et al., Sensitization of charge injection into semiconductors with large band gap. *Electrochim. Acta* **1968,** *13* (6), 1509-1515.

75. Duonghond, D.; Serpone, N.; et al., Integrated Systems for Water Cleavage by Visible Light; Sensitization of TiO_2 Particles by Surface Derivatization with Ruthenium Complexes. *Helv. Chim. Acta* **1984,** *67* (4), 1012-1018.

76. Desilvestro, J.; Grätzel, M.; et al., Highly efficient sensitization of titanium dioxide. *J. Am. Chem. Soc.* **1985,** *107* (10), 2988-2990.

77. O'Regan, B. and Grätzel, M., A low-cost, high-efficiency solar cell based on dye-sensitized colloidal TiO_2 films. *Nature* **1991,** *353* (6346), 737-740.

78. Nazeeruddin, M. K.; Kay, A.; et al., Conversion of light to electricity by cis-X_2bis(2,2'-bipyridyl-4,4'-dicarboxylate)ruthenium(II) charge-transfer sensitizers (X = Cl^-, Br^-, I^-, CN^-, and SCN^-) on nanocrystalline titanium dioxide electrodes. *J. Am. Chem. Soc.* **1993,** *115* (14), 6382-6390.

79. Benkö, G.; Kallioinen, J.; et al., Photoinduced Ultrafast Dye-to-Semiconductor Electron Injection from Nonthermalized and Thermalized Donor States. *J. Am. Chem. Soc.* **2002,** *124* (3), 489-493.

80. Nazeeruddin, M. K.; Péchy, P.; et al., Engineering of Efficient Panchromatic Sensitizers for Nanocrystalline TiO_2-Based Solar Cells. *J. Am. Chem. Soc.* **2001,** *123* (8), 1613-1624.

81. Grätzel, M., Dye-sensitized solar cells. *J. Photochem. Photobio., C* **2003,** *4* (2), 145-153.

82. Adeloye, A. and Ajibade, P., Towards the Development of Functionalized PolypyridineLigands for Ru(II) Complexes as Photosensitizers in Dye-Sensitized Solar Cells (DSSCs). *Molecules* **2014,** *19* (8), 12421.

83. Kanna, M. and Wongnawa, S., Mixed amorphous and nanocrystalline TiO_2 powders prepared by sol-gel method: Characterization and photocatalytic study. *Mater. Chem. Phys.* **2008,** *110* (1), 166-175.

84. Korosi, L.; Papp, S.; et al., Surface and Bulk Composition, Structure, and Photocatalytic Activity of Phosphate-Modified TiO_2. *Chem. Mater.* **2007,** *19* (19), 4811-4819.

85. Xie, H.; Zhang, Q.; et al., Thermal analysis on nanosized TiO_2 prepared by hydrolysis. *Thermochim. Acta* **2002,** *381* (1), 45-48.

86. Zhang, T.; Oyama, T.; et al., Photooxidative N-demethylation of methylene blue in aqueous TiO_2 dispersions under UV irradiation. *J. Photochem. Photobio., A* **2001,** *140* (2), 163-172.

87. Houas, A.; Lachheb, H.; et al., Photocatalytic degradation pathway of methylene blue in water. *Appl. Catal., B* **2001,** *31* (2), 145-157.

88. Yu, Z. and Chuang, S. S. C., Probing Methylene Blue Photocatalytic Degradation by Adsorbed Ethanol with In Situ IR. *J. Phys. Chem. C* **2007,** *111* (37), 13813-13820.

89. Yu, Z. and Chuang, S. S. C., In situ IR study of adsorbed species and photogenerated electrons during photocatalytic oxidation of ethanol on TiO_2. *J. Catal.* **2007,** *246* (1), 118-126.

90. Brauer, J. The Effect of Fluoride on The Crystallinity and Photoactivity of TiO_2. Ph.D., The University of Alabama, Tuscaloosa, 2012.

91. Laserna, J. J. An Introduction to Raman Spectroscopy: Introduction and Basic Principles 2005. http://www.spectroscopynow.com/details/education/sepspec1882education/An-Introduction-to-Raman-Spectroscopy-Introduction-and-Basic-Principles.html?&tzcheck=1 (accessed September 4, 2014).

92. Raman, C. V. and Krishnan, K. S., The Optical Analogue of the Compton Effect. *Nature* **1928,** *121*, 711.

93. Scherrer, P., Bestimmung der Gröβe und der inneren Struktur von Kolloidteilchen mittels Röntgenstrahlen. *Gottinger Nachrichten Gesell* **1918,** *2*, 98-100.

94. Gouadec, G. n. l. and Colomban, P., Raman Spectroscopy of nanomaterials: How spectra relate to disorder, particle size and mechanical properties. *Prog. Cryst. Growth Charact. Mater.* **2007,** *53* (1), 1-56.

95. Loridant, S.; Lucazeau, G.; et al., A high-pressure Raman and X-ray diffraction study of the perovskite $SrCeO_3$. *J. Phys. Chem. Solids* **2002,** *63* (11), 1983-1992.

96. Gouadec, G. and Colomban, P., Raman Spectroscopy of nanomaterials: How spectra relate to disorder, particle size and mechanical properties. *Prog. Cryst. Growth Charact. Mater.* **2007,** *53* (1), 1-56.

97. Ghobadi, N., Band gap determination using absorption spectrum fitting procedure. *Int. Nano Lett.* **2013,** *3* (1), 2.

98. Shimadzu, UV-3600 Plus UV-VIS-NIR Spectrophotometer. 2015.

99. Watts, J. F. and Wolstenholme, J., *An Introduction to Surface Analysis by XPS and AES*. John Wiley & Sons Ltd: West Sussex, 2003; p 212.

100. Hu, Y.; Tsai, H. L.; et al., Phase transformation of precipitated TiO_2 nanoparticles. *Mater. Sci. Eng., A* **2003,** *344* (1-2), 209-214.

101. Huberty, J. and Xu, H., Kinetics study on phase transformation from titania polymorph brookite to rutile. *J. Solid State Chem.* **2008,** *181* (3), 508-514.

102. Li, J.-G. and Ishigaki, T., Brookite → rutile phase transformation of TiO_2 studied with monodispersed particles. *Acta Mater.* **2004,** *52* (17), 5143-5150.

103. Jamieson, J. C. and Olinger, B., Pressure-temperature studies of anatase, brookite, rutile, and TiO_2(II): A Discussion. *Am. Mineral.* **1969,** *54,* 1477-1481.

104. Wang, Q.; Chen, X.; et al., Synergistic photosensitized removal of Cr(VI) and Rhodamine B dye on amorphous TiO_2 under visible light irradiation. *J. Hazard. Mater.* **2013,** *246-247*, 135-144.

105. Li, Z.; Zhu, Y.; et al., Size-controlled synthesis of dispersed equiaxed amorphous TiO_2 nanoparticles. *Ceram. Int.* **2015,** *41* (7), 9057-9062.

106. Yanagisawa, K. and Ovenstone, J., Crystallization of Anatase from Amorphous Titania Using the Hydrothermal Technique: Effects of Starting Material and Temperature. *J. Phys. Chem. B* **1999,** *103* (37), 7781-7787.

107. Isley, S. L. and Penn, R. L., Relative Brookite and Anatase Content in Sol-Gel-Synthesized Titanium Dioxide Nanoparticles. *J. Phys. Chem. B* **2006,** *110* (31), 15134-15139.

108. Koelsch, M.; Cassaignon, S.; et al., Synthesis of nanometric TiO_2 in aqueous solution by soft chemistry: obtaining of anatase, brookite and rutile with controlled shapes. *MRS Online Proceedings Library* **2004,** *822*, 79.

109. Zhang, Q. H.; Gao, L.; et al., Preparation and characterization of nanosized TiO_2 powders from aqueous $TiCl_4$ solution. *Nanostruct. Mater.* **1999,** *11* (8), 1293-1300.

110. Li, W.; Ni, C.; et al., Size dependence of thermal stability of TiO_2 nanoparticles. *J. Appl. Phys.* **2004,** *96* (11), 6663-6668.

111. Barnard, A. S. and Zapol, P., Effects of particle morphology and surface hydrogenation on the phase stability of TiO_2. *Phys. Rev. B: Condens. Matter Mater. Phys.* **2004,** *70* (23), 235403.

112. Barnard, A. S. and Curtiss, L. A., Prediction of TiO_2 Nanoparticle Phase and Shape Transitions Controlled by Surface Chemistry. *Nano Lett.* **2005,** *5* (7), 1261-1266.

113. Reidy, D. J.; Holmes, J. D.; et al., The critical size mechanism for the anatase to rutile transformation in TiO_2 and doped-TiO_2. *J. Eur. Ceram. Soc.* **2006,** *26* (9), 1527-1534.

114. Shannon, R. D. and Pask, J. A., Kinetics of the Anatase-Rutile Transformation. *J. Am. Ceram. Soc.* **1965,** *48* (8), 391-398.

115. Kumar, K. N. P.; Keizer, K.; et al., Stabilization of the porous texture of nanostructured titanic by avoiding a phase transformation. *J. Mater. Sci. Lett.* **1994,** *13* (1), 59-61.

116. Penn, R. L. and Banfield, J. F., Formation of rutile nuclei at anatase {112} twin interfaces and the phase transformation mechanism in nanocrystalline titania. *Am. Mineral.* **1999,** *84,* 871-876.

117. Rothschild, A.; Levakov, A.; et al., Surface photovoltage spectroscopy study of reduced and oxidized nanocrystalline TiO_2 films. *Surf. Sci.* **2003,** *532-535*, 456-460.

118. Dohnálek, Z.; Kim, J.; et al., Physisorption of N_2, O_2, and CO on Fully Oxidized TiO_2(110). *J. Phys. Chem. B* **2006,** *110* (12), 6229-6235.

119. Sorescu, D. C.; Rusu, C. N.; et al., Adsorption of NO on the TiO_2(110) Surface: An Experimental and Theoretical Study. *J. Phys. Chem. B* **2000,** *104* (18), 4408-4417.

120. Onishi, H.; Aruga, T.; et al., Adsorption of CH_3OH, HCOOH and SO_2 on TiO_2(110) and stepped TiO_2(441) surfaces. *Surf. Sci.* **1988,** *193* (1-2), 33-46.

121. Raza, H.; Harte, S. P.; et al., NEXAFS studies of the reaction of SO_2 with TiO_2(100)-(1 Ã— 1) and -(1 Ã— 3). *Surf. Sci.* **1996,** *366* (3), 519-530.

122. Diebold, U.; Hebenstreit, W.; et al., High Transient Mobility of Chlorine on TiO_2(110): Evidence for ``Cannon-Ball" Trajectories of Hot Adsorbates. *Phys. Rev. Lett.* **1998,** *81* (2), 405-408.

123. Gamble, L.; Jung, L. S.; et al., Decomposition and protonation of surface ethoxys on TiO_2(110). *Surf. Sci.* **1996,** *348* (1-2), 1-16.

124. Deng, X.; Yue, Y.; et al., Gas-phase photo-oxidation of organic compounds over nanosized TiO_2 photocatalysts by various preparations. *Appl. Catal., B* **2002,** *39* (2), 135-147.

125. Zhang, Q.; Gao, L.; et al., Effect of hydrolysis conditions on morphology and crystallization of nanosized TiO_2 powder. *J. Eur. Ceram. Soc.* **2000,** *20* (12), 2153-2158.

126. Gong, W., A real time in situ ATR-FTIR spectroscopic study of linear phosphate adsorption on titania surfaces. *Int. J. Miner. Process.* **2001,** *63* (3), 147-165.

127. Connor, P. A. and McQuillan, A. J., Phosphate Adsorption onto TiO_2 from Aqueous Solutions: An in Situ Internal Reflection Infrared Spectroscopic Study. *Langmuir* **1999,** *15* (8), 2916-2921.

128. Cheng, F.; Sajedin, S. M.; et al., UV-stable paper coated with APTES-modified P25 TiO_2 nanoparticles. *Carbohydr. Polym.* **2014,** *114* (0), 246-252.

129. Gamble, L.; Jung, L. S.; et al., Interaction of Silane Coupling Agents with the TiO_2(110) Surface. *Langmuir* **1995,** *11* (11), 4505-4514.

130. Pazokifard, S.; Farrokhpay, S.; et al., Surface treatment of TiO_2 nanoparticles via sol-gel method: Effect of silane type on hydrophobicity of the nanoparticles. *Prog. Org. Coat.* **2015,** *87*, 36-44.

131. Rahal, R.; Annani, F.; et al., Surface modification of titanium oxide nanoparticles with chelating molecules: New recognition devices for controlling the selectivity towards lanthanides ionic separation. *Sep. Purif. Technol.* **2015,** *147*, 220-226.

132. Shun-Xing, L.; Feng-Ying, Z.; et al., Surface modification of nanometer size TiO_2 with salicylic acid for photocatalytic degradation of 4-nitrophenol. *J. Hazard. Mater.* **2006,** *135* (1-3), 431-436.

133. Skubal, L. R.; Meshkov, N. K.; et al., Cadmium removal from water using thiolactic acid-modified titanium dioxide nanoparticles. *J. Photochem. Photobio., A* **2002,** *148* (1-3), 393-397.

134. Korosi, L. and Dekany, I., Preparation and investigation of structural and photocatalytic properties of phosphate modified titanium dioxide. *Colloids Surf., A* **2006,** *280* (1-3), 146-154.

135. Peña-Alonso, R.; Rubio, F.; et al., Study of the hydrolysis and condensation of γ-Aminopropyltriethoxysilane by FT-IR spectroscopy. *J. Mater. Sci.* **2007,** *42* (2), 595-603.

136. Hurwitz, F. I.; Heimann, P. J.; et al., Polymeric Routes to Silicon Carbide and Silicon Oxycarbide CMC. In *Proceedings of the 15th Annual Conference on Composites and Advanced Ceramic Materials: Ceramic Engineering and Science Proceedings*, John Wiley & Sons, Inc.: 2008; pp 1292-1303.

137. Watson, S.; Beydoun, D.; et al., Preparation of nanosized crystalline TiO_2 particles at low temperature for photocatalysis. *J. Nanopart. Res.* **2004,** *6* (2), 193-207.

138. Hair, M. L. and Tripp, C. P., Alkylchlorosilane reactions at the silica surface. *Colloids Surf., A* **1995,** *105* (1), 95-103.

139. Colthup, N. B.; Wiberley, S. E.; et al., *Introduction to Infrared and Raman Spectroscopy*. Academic Press: New York, 1964; p 191-298.

140. Bellamy, L. J., *The Infra-red Spectra of Complex Molecules*. Chapman and Hall Ltd.: London, 1975; Vol. 3, p 13-60.

141. Nakamoto, K., *Infrared and Raman Spectra of Inorganic and Coordination Compounds Part B: Applications in Coordination, Organometallic, and Bioinorganic Chemistry*. 5th ed.; John Wiley & Sons, Inc.: New York, 1997; p 385.

142. Barraclough, C. G. and Tobe, M. L., 380. The preparation and properties of chelated sulphatobis-(ethylenediamine)cobalt(III) salts. *J. Chem. Soc.* **1961,** (0), 1993-1996.

143. Lane, M. D., Mid-infrared emission spectroscopy of sulfate and sulfate-bearing minerals. *Am. Mineral.* **2007,** *92*, 1-18.

144. Eskenazi, R.; Raskovan, J.; et al., Sulphato complexes of palladium (II). *J. Inorg. Nucl. Chem.* **1966,** *28* (2), 521-526.

145. Barraclough, C. G. and Tobe, M. L., The preparation and properties of chelated sulphatobis-(ethylenediamine)cobalt(III) salts. *J. Chem. Soc.* **1961,** (0), 1993-1996.

146. Yang, S.-q.; Yuan, P.; et al., Effect of reaction temperature on grafting of γ-aminopropyl triethoxysilane (APTES) onto kaolinite. *Appl. Clay Sci.* **2012,** *62-63* (0), 8-14.

147. Yuan, W. and van Ooij, W. J., Characterization of Organofunctional Silane Films on Zinc Substrates. *J. Colloid Interface Sci.* **1997,** *185* (1), 197-209.

148. Gamble, L.; Henderson, M. A.; et al., Organofunctionalization of TiO_2(110): (3,3,3-Trifluoropropyl)trimethoxysilane Adsorption. *J. Phys. Chem. B* **1998,** *102* (23), 4536-4543.

149. Zheng, T.-T.; Sun, Z.-X.; et al., Sorption of phosphate onto mesoporous γ-alumina studied with in-situ ATR-FTIR spectroscopy. *Chem. Cent. J.* **2012,** *6* (1), 1-10.

150. Xu, N.; Yin, H.; et al., Mechanisms of phosphate retention by calcite: effects of magnesium and pH. *J. Soils Sediments* **2014,** *14* (3), 495-503.

151. Smith, N. A.; Antoun, G. G.; et al., Improved adhesion between nickel-titanium shape memory alloy and a polymer matrix via silane coupling agents. *Composites, Part A* **2004,** *35* (11), 1307-1312.

152. Viornery, C.; Chevolot, Y.; et al., Surface Modification of Titanium with Phosphonic Acid To Improve Bone Bonding: Characterization by XPS and ToF-SIMS. *Langmuir* **2002,** *18* (7), 2582-2589.

153. Sargeant, T. D.; Rao, M. S.; et al., Covalent functionalization of NiTi surfaces with bioactive peptide amphiphile nanofibers. *Biomaterials* **2008,** *29* (8), 1085-1098.

154. Song, Y.-Y.; Hildebrand, H.; et al., Optimized monolayer grafting of 3-aminopropyltriethoxysilane onto amorphous, anatase and rutile TiO_2. *Surf. Sci.* **2010,** *604* (3-4), 346-353.

155. Moulder, J. F.; Stickle, W. F.; et al., *Handbook of X-ray Photoelectron Spectroscopy*. Physical Electronics Inc.: Eden Prairie, 1995; p 261.

156. Xiao, S.-J.; Textor, M.; et al., Covalent Attachment of Cell-Adhesive, (Arg-Gly-Asp)-Containing Peptides to Titanium Surfaces. *Langmuir* **1998,** *14* (19), 5507-5516.

157. Sham, T. K. and Lazarus, M. S., X-ray photoelectron spectroscopy (XPS) studies of clean and hydrated TiO_2 (rutile) surfaces. *Chem. Phys. Lett.* **1979,** *68* (2-3), 426-432.

158. Hanawa, T.; Hiromoto, S.; et al., Characterization of the surface oxide film of a Co-Cr-Mo alloy after being located in quasi-biological environments using XPS. *Appl. Surf. Sci.* **2001,** *183* (1-2), 68-75.

159. Topalian, Z.; Niklasson, G. A.; et al., Spectroscopic Study of the Photofixation of SO_2 on Anatase TiO_2 Thin Films and Their Oleophobic Properties. *ACS Appl. Mater. Interfaces* **2012,** *4* (2), 672-679.

160. Chen, J. P. and Yang, R. T., Selective Catalytic Reduction of NO with NH_3 on SO_4^{-2}/TiO_2 Superacid Catalyst. *J. Catal.* **1993,** *139* (1), 277-288.

161. Dominguez, A. M.; Zarate, A.; et al., Sol-gel iron complex catalysts supported on TiO_2 for ethylene polymerization. *J. Mol. Catal. A: Chem.* **2004,** *207* (2), 155-161.

162. Morant, C.; Torres, R.; et al., Characterization of Nitrogen-Doped Carbon Nanotubes by Atomic Force Microscopy, X-ray Photoelectron Spectroscopy and X-ray Absorption Near Edge Spectroscopy. *J. Nanosci. Nanotechnol.* **2009,** *9* (6), 3633-3638.

163. Lopez-Salas, N.; Gutierrez, M. C.; et al., Nitrogen-doped carbons prepared from eutectic mixtures as metal-free oxygen reduction catalysts. *J. Mater. Chem. A* **2016,** *4* (2), 478-488.

164. Komatsu, T., Bulk synthesis and characterization of graphite-like B-C-N and B-C-N heterodiamond compounds. *J. Mater. Chem.* **2004,** *14* (2), 221-227.

165. Kallury, K. M. R.; Macdonald, P. M.; et al., Effect of Surface Water and Base Catalysis on the Silanization of Silica by (Aminopropyl)alkoxysilanes Studied by X-ray Photoelectron Spectroscopy and 13C Cross-Polarization/Magic Angle Spinning Nuclear Magnetic Resonance. *Langmuir* **1994,** *10* (2), 492-499.

166. Martin, H. J.; Schulz, K. H.; et al., An XPS study on the attachment of triethoxsilylbutyraldehyde to two titanium surfaces as a way to bond chitosan. *Appl. Surf. Sci.* **2008,** *254* (15), 4599-4605.

167. Kishor, R. and Ghoshal, A. K., APTES grafted ordered mesoporous silica KIT-6 for CO_2 adsorption. *Chem. Eng. J.* **2015,** *262* (0), 882-890.

168. Anatase - JDPDS card # 84-1286. The International Centre for Diffraction Data: 2000.

169. Rutile - JDPDS card # 87-0920. The International Centre for Diffraction Data: 2000.

170. dos Santos, D. R. and Torriani, I. L., Crystallite size determination in μc-Ge films by x-ray diffraction and Raman line profile analysis. *Solid State Commun.* **1993,** *85* (4), 307-310.

171. Galwey, A. K. and Brown, M. E., *Thermal Decomposition of Ionic Solids: Chemical Properties and Reactivities of Ionic Crystalline Phases*. Elsevier Science: 1999.

172. Khlestkin, R. N.; Khlestkina, V. L.; et al., Thermal stability of carboxylate salts. *React. Kinet. Catal. Lett.* **1981,** *17* (3-4), 391-392.

173. Mu, J. and Perlmutter, D. D., Thermal decomposition of inorganic sulfates and their hydrates. *Ind. Eng. Chem. Process Des. Dev.* **1981,** *20* (4), 640-646.

174. Hastie, J. W.; Hildenbrand, D. L.; et al., Mechanistic Aspects of Metal Sulfate Decomposition Processes. In *Materials Chemistry at High Temperatures*, Humana Press: 1990; Vol. 1, pp 427-440.

175. Rao, R.; Podila, R.; et al., Effects of Layer Stacking on the Combination Raman Modes in Graphene. *ACS Nano* **2011,** *5* (3), 1594-1599.

176. Hodkiewicz, J. *Characterizing Graphene with Raman Spectroscopy*; 51946; Thermofisher Scientific: 2010.

177. Sato, K.; Park, J. S.; et al., Raman spectra of out-of-plane phonons in bilayer graphene. *Phys. Rev. B: Condens. Matter Mater. Phys.* **2011,** *84* (3), 035419.

178. Ranade, M. R.; Navrotsky, A.; et al., Energetics of nanocrystalline TiO_2. *Proc. Natl. Acad. Sci. U. S. A.* **2002,** *99* (suppl. 2), 6476-6481.

179. Buerger, *Phase Transformations in Solids*. John Wiley: New York, 1951.

180. Yoganarasimhan, S. R. and Rao, C. N. R., Mechanism of crystal structure transformations. Part 3.-Factors affecting the anatase-rutile transformation. *Trans. Faraday Soc.* **1962,** *58* (0), 1579-1589.

181. Ma, J.-S.; Wen, M.-C.; et al., Reaction mechanism and kinetics analysis of the phase transformation of TiO_2 from the anatase phase to the rutile phase. *J. Mater. Sci.: Mater. Electron.* **2013,** *24* (7), 2506-2512.

182. Zhu, J.; Zheng, W.; et al., Characterization of Fe-TiO_2 photocatalysts synthesized by hydrothermal method and their photocatalytic reactivity for photodegradation of XRG dye diluted in water. *J. Mol. Catal. A: Chem.* **2004,** *216* (1), 35-43.

183. Lin, H.-y. and Shih, C.-y., Efficient one-pot microwave-assisted hydrothermal synthesis of M (M = Cr, Ni, Cu, Nb) and nitrogen co-doped TiO_2 for hydrogen production by photocatalytic water splitting. *J. Mol. Catal. A: Chem.* **2016,** *411*, 128-137.

184. Chen, Y.; Wang, J.; et al., Microwave-assisted hydrothermal synthesis of Au/TiO_2/SBA-15 for enhanced visible-light photoactivity. *Mater. Lett.* **2015,** *159*, 131-134.

185. Zhang, F.; Pi, Y.; et al., Unexpected Selective Photocatalytic Reduction of Nitrite to Nitrogen on Silver-Doped Titanium Dioxide. *J. Phys. Chem. C* **2007,** *111* (9), 3756-3761.

186. Anpo, M., Use of visible light. Second-generation titanium oxide photocatalysts prepared by the application of an advanced metal ion-implantation method. *Pure Appl. Chem.* **2000,** *72* (9), 1787-1792.

187. Yamashita, H.; Harada, M.; et al., Degradation of propanol diluted in water under visible light irradiation using metal ion-implanted titanium dioxide photocatalysts. *J. Photochem. Photobio., A* **2002,** *148* (1-3), 257-261.

188. Momeni, M. M. and Ghayeb, Y., Photoelectrochemical water splitting on chromium-doped titanium dioxide nanotube photoanodes prepared by single-step anodizing. *J. Alloys Compd.* **2015,** *637*, 393-400.

189. Asahi, R.; Morikawa, T.; et al., Visible-Light Photocatalysis in Nitrogen-Doped Tiatnium Oxides. *Science* **2001,** *293*, 269-271.

190. Chiu, S.-M.; Chen, Z.-S.; et al., Photocatalytic activity of doped TiO_2 coatings prepared by sputtering deposition. *Journal of Materials Processing Technology* **2007,** *192-193*, 60-67.

191. Zhang, W.; Zhu, S.; et al., Photocatalytic Zn-doped TiO_2 films prepared by DC reactive magnetron sputtering. *Vacuum* **2007,** *82* (3), 328-335.

192. Lee, S.-H.; Yamasue, E.; et al., Preparation of N-Doped TiO_x Films as Photocatalyst Using Reactive Sputtering with Dry Air. *Mater. Trans.* **2009,** *50* (7), 1802-1811.

193. Maparu, A. K.; Ganvir, V.; et al., Titania nanofluids with improved photocatalytic activity under visible light. *Colloids Surf., A* **2015,** *482*, 345-352.

194. Kang, I.-C.; Zhang, Q.; et al., Synthesis of nitrogen doped TiO_2 by grinding in gaseous NH_3. *J. Photochem. Photobio., A* **2007,** *189* (2-3), 232-238.

195. Tran, T. M. N.; Quach, T. H. Y.; et al., Synthesis of vanadium-modified rutile TiO_2 nanoparticle by reactive grinding method and its photocatalytic activity under solar light at room temperature. *Adv. Nat. Sci.: Nanosci. Nanotechnol.* **2013,** *4* (3), 035010.

196. Bessergenev, V. G.; Mateus, M. C.; et al., TiO_2:(Fe, S) Thin Films Prepared from Complex Precursors by CVD, Physical Chemical Properties, and Photocatalysis. *Int. J. Photoenergy* **2012,** *2012*, 12.

197. Umebayashi, T.; Yamaki, T.; et al., Band gap narrowing of titanium dioxide by sulfur doping. *Appl. Phys. Lett.* **2002,** *81* (3), 454-456.

198. Loganathan, K.; Bommusamy, P.; et al., The Syntheses, Characterizations, and Photocatalytic Activities of Silver, Platinum, and Gold Doped TiO_2 Nanoparticles. *Environ. Eng. Res.* **2011,** *16* (2), 81-90.

199. Wu, J. C. S. and Chen, C.-H., A visible-light response vanadium-doped titania nanocatalyst by sol-gel method. *J. Photochem. Photobio., A* **2004,** *163* (3), 509-515.

200. Wilke, K. and Breuer, H. D., The influence of transition metal doping on the physical and photocatalytic properties of titania. *J. Photochem. Photobio., A* **1999,** *121* (1), 49-53.

201. Kernazhitsky, L.; Shymanovska, V.; et al., A comparative study of optical absorption and photocatalytic properties of nanocrystalline single-phase anatase and rutile TiO_2 doped with transition metal cations. *J. Solid State Chem.* **2013,** *198* (0), 511-519.

202. Duta, M.; Predoana, L.; et al., Nb-doped TiO_2 sol-gel films for CO sensing applications. *Mater. Sci. Semicond. Process.* **2016,** *42, Part 3*, 397-404.

203. Crisan, M.; Raileanu, M.; et al., Sol-gel iron-doped TiO_2 nanopowders with photocatalytic activity. *Appl. Catal., A* **2015,** *504*, 130-142.

204. Thomas, A. G.; Flavell, W. R.; et al., Adsorption of phenylalanine on single crystal rutile TiO_2(110) surface. *Surf. Sci.* **2007,** *601* (18), 3828-3832.

205. Hu, Y.; Song, X.; et al., Enhanced photocatalytic activity of Pt-doped TiO_2 for NO_x oxidation both under UV and visible light irradiation: A synergistic effect of lattice Pt^{4+} and surface PtO. *Chem. Eng. J.* **2015,** *274*, 102-112.

206. Riyapan, S.; Boonyongmaneerat, Y.; et al., Effect of surface Ti^{3+} on the sol-gel derived TiO_2 in the selective acetylene hydrogenation on Pd/TiO_2 catalysts. *Catal. Today* **2015,** *245*, 134-138.

207. Davis, Z. D. and Tatarchuk, B. J., Understanding the dispersion of Ag on high surface area TiO_2 supports using XPS intensity ratios. *Appl. Surf. Sci.* **2015,** *353*, 679-685.

208. Lee, M. S.; Hong, S.-S.; et al., Synthesis of photocatalytic nanosized TiO_2-Ag particles with sol-gel method using reduction agent. *J. Mol. Catal. A: Chem.* **2005,** *242* (1-2), 135-140.

209. Garcia-Serrano, J.; Gomez-Hernandez, E.; et al., Effect of Ag doping on the crystallization and phase transition of TiO_2 nanoparticles. *Curr. Appl. Phys.* **2009,** *9* (5), 1097-1105.

210. Gupta, S. M. and Tripathi, M., A review of TiO_2 nanoparticles. *Chin. Sci. Bull.* **2011,** *56* (16), 1639-1657.

211. Sayyar, Z.; Akbar Babaluo, A.; et al., Kinetic study of formic acid degradation by Fe^{3+} doped TiO_2 self-cleaning nanostructure surfaces prepared by cold spray. *Appl. Surf. Sci.* **2015,** *335*, 1-10.

212. Ohno, T.; Higo, T.; et al., Dependence of photocatalytic activity on aspect ratio of a brookite TiO_2 nanorod and drastic improvement in visible light responsibility of a brookite TiO_2 nanorod by site-selective modification of Fe^{3+} on exposed faces. *J. Mol. Catal. A: Chem.* **2015,** *396*, 261-267.

213. Lee, T.-h.; Ryu, H.; et al., Photoelectrochemical properties of iron (III)-doped TiO_2 nanorods. *Ceram. Int.* **2015,** *41* (6), 7582-7589.

214. Mugundan, S.; Rajamannan, B.; et al., Synthesis and characterization of undoped and cobalt-doped TiO_2 nanoparticles via sol-gel technique. *Appl. Nanosci.* **2014**, 1-8.

215. Yang, J.; Cui, S.; et al., The photocatalytic dehalogenation of chlorophenols and bromophenols by cobalt doped nano TiO2. *J. Mol. Catal. A: Chem.* **2014,** (0).

216. Chen, Q.; Ji, F.; et al., Synergistic effect of bifunctional Co-TiO_2 catalyst on degradation of Rhodamine B: Fenton-photo hybrid process. *Chem. Eng. J.* **2013,** *229* (0), 57-65.

217. Ganesh, I.; Gupta, A. K.; et al., Preparation and characterization of Co-doped TiO_2 materials for solar light induced current and photocatalytic applications. *Mater. Chem. Phys.* **2012,** *135* (1), 220-234.

218. Obregón, S.; Muñoz-Batista, M. J.; et al., Cu-TiO_2 systems for the photocatalytic H_2 production: Influence of structural and surface support features. *Appl. Catal., B* **2015,** *179*, 468-478.

219. Ako, R. T.; Ekanayake, P.; et al., Evaluation of surface energy state distribution and bulk defect concentration in DSSC photoanodes based on Sn, Fe, and Cu doped TiO_2. *Appl. Surf. Sci.* **2015,** *351*, 950-961.

220. Biyoghe Bi Ndong, L.; Ibondou, M. P.; et al., Enhanced Photocatalytic Activity of TiO_2 Nanosheets by Doping with Cu for Chlorinated Solvent Pollutants Degradation. *Ind. Eng. Chem. Res.* **2014,** *53* (4), 1368-1376.

221. Sharma, S. D.; Singh, D.; et al., Sol-gel-derived super-hydrophilic nickel doped TiO_2 film as active photo-catalyst. *Appl. Catal., A* **2006,** *314* (1), 40-46.

222. Min, O. M.; Ong, S.-A.; et al., Effects of Synthesis Ni Doped TiO_2 on Photocatalytic Degradation Process. *Adv. Environ. Biol.* **2014,** *8* (9), 501-503.

223. Kernazhitsky, L.; Shymanovska, V.; et al., Photoluminescence of Cr-doped TiO_2 induced by intense UV laser excitation. *J. Lumin.* **2015,** *166*, 253-258.

224. Osterwalder, J.; Droubay, T.; et al., Growth of Cr-doped TiO_2 films in the rutile and anatase structures by oxygen plasma assisted molecular beam epitaxy. *Thin Solid Films* **2005,** *484* (1-2), 289-298.

225. Roncari, E.; Galassi, C.; et al., Vanadium-doped TiO_2 catalysts. A unifying picture of powders and suspensions. *Colloids Surf., A* **1996,** *117* (3), 267-272.

226. Haber, J.; Nowak, P.; et al., Charge Transfer in Photocatalytic Systems: V and Mo Doped TiO_2/Ti Electrodes. *Catal. Lett.* **2008,** *126* (1), 43-48.

227. Lu, D.; Zhao, B.; et al., Facile one-pot fabrication and high photocatalytic performance of vanadium doped TiO_2-based nanosheets for visible-light-driven degradation of RhB or Cr(VI). *Appl. Surf. Sci.* **2015,** *359*, 435-448.

228. Quiñones, D. H.; Rey, A.; et al., Boron doped TiO_2 catalysts for photocatalytic ozonation of aqueous mixtures of common pesticides: Diuron, o-phenylphenol, MCPA and terbuthylazine. *Appl. Catal., B* **2015,** *178*, 74-81.

229. Siuzdak, K.; Szkoda, M.; et al., Thin layer of ordered boron-doped TiO_2 nanotubes fabricated in a novel type of electrolyte and characterized by remarkably improved photoactivity. *Appl. Surf. Sci.* **2015,** *357, Part A*, 942-950.

230. Szkoda, M.; Siuzdak, K.; et al., Facile preparation of extremely photoactive boron-doped TiO_2 nanotubes arrays. *Electrochem. Commun.* **2015,** *60*, 212-215.

231. McManamon, C.; O'Connell, J.; et al., A facile route to synthesis of S-doped TiO_2 nanoparticles for photocatalytic activity. *J. Mol. Catal. A: Chem.* **2015,** *406*, 51-57.

232. Han, C.; Andersen, J.; et al., The effect of solvent in the sol-gel synthesis of visible light-activated, sulfur-doped TiO_2 nanostructured porous films for water treatment. *Catal. Today* **2014,** *224*, 132-139.

233. Kuo, C.-Y. and Hsiao, H.-M., Preparation of iodine doped titanium dioxide to photodegrade aqueous bisphenol A under visible light. *Process Saf. Environ. Prot.* **2015,** *95*, 265-270.

234. Veréb, G.; Manczinger, L.; et al., Highly efficient bacteria inactivation and phenol degradation by visible light irradiated iodine doped TiO_2. *Appl. Catal., B* **2013,** *129*, 194-201.

235. Yang, Z.; Tang, X.; et al., Enhanced performance of dye-sensitized solar cells with fluorine doped nanocrystalline TiO_2 as photoanode. *Electrochim. Acta* **2015,** *186*, 151-156.

236. Dozzi, M. V.; Zuliani, A.; et al., Photocatalytic activity of one step flame-made fluorine doped TiO_2. *Appl. Catal., A* **2015**.

237. Umadevi, M.; Sangari, M.; et al., Enhanced photocatalytic, antimicrobial activity and photovoltaic characteristics of fluorine doped TiO_2 synthesized under ultrasound irradiation. *J. Fluorine Chem.* **2013,** *156*, 209-213.

238. Sullivan, J. A.; Neville, E. M.; et al., Routes to visible light active C-doped TiO_2 photocatalysts using carbon atoms from the Ti precursors. *J. Photochem. Photobio., A* **2014,** *289*, 60-65.

239. Zhao, C.; Liu, L.; et al., Synthesis of Carbon-TiO_2 Nanocomposites with Enhanced Reversible Capacity and Cyclic Performance as Anodes for Lithium-Ion Batteries. *Electrochim. Acta* **2015,** *155*, 288-296.

240. Slimen, H.; Lachheb, H.; et al., The effect of calcination atmosphere on the structure and photoactivity of TiO_2 synthesized through an unconventional doping using activated carbon. *J. Environ. Chem. Eng.* **2015,** *3* (2), 922-929.

241. Vaiano, V.; Sacco, O.; et al., Nanostructured N-doped TiO_2 coated on glass spheres for the photocatalytic removal of organic dyes under UV or visible light irradiation. *Appl. Catal., B* **2015,** *170-171*, 153-161.

242. Li, H.; Hao, Y.; et al., A systematic study on visible-light N-doped TiO_2 photocatalyst obtained from ethylenediamine by sol-gel method. *Appl. Surf. Sci.* **2015,** *344*, 112-118.

243. Iwase, M.; Yamada, K.; et al., Visible-light photocatalysis with phosphorus-doped titanium(IV) oxide particles prepared using a phosphide compound. *Appl. Catal., B* **2013,** *132-133*, 39-44.

244. Han, Z.; Wang, J.; et al., Phosphorus doped TiO_2 as oxygen sensor with low operating temperature and sensing mechanism. *Appl. Surf. Sci.* **2013,** *273*, 349-356.

245. Diwald, O.; Thompson, T. L.; et al., The Effect of Nitrogen Ion Implantation on the Photoactivity of TiO_2 Rutile Single Crystals. *J. Phys. Chem. B* **2004,** *108* (1), 52-57.

246. Ao, Y.; Xu, J.; et al., A one-pot method to prepare N-doped titania hollow spheres with high photocatalytic activity under visible light. *Appl. Surf. Sci.* **2010,** *256* (9), 2754-2758.

247. Ni, M.; Leung, M. K. H.; et al., A review and recent developments in photocatalytic water-splitting using for hydrogen production. *Renewable Sustainable Energy Rev.* **2007,** *11* (3), 401-425.

248. Körösi, L.; Papp, S.; et al., Surface and Bulk Composition, Structure, and Photocatalytic Activity of Phosphate-Modified TiO_2. *Chem. Mater.* **2007,** *19* (19), 4811-4819.

249. Choi, J.; Park, H.; et al., Effects of Single Metal-Ion Doping on the Visible-Light Photoreactivity of TiO_2. *J. Phys. Chem. C* **2009,** *114* (2), 783-792.

250. Gonell, F.; Puga, A. V.; et al., Copper-doped titania photocatalysts for simultaneous reduction of CO_2 and production of H_2 from aqueous sulfide. *Appl. Catal., B* **2016,** *180*, 263-270.

251. Karmakar, R.; Neogi, S. K.; et al., Structural; morphological; optical and magnetic properties of Mn doped ferromagnetic ZnO thin film. *Appl. Surf. Sci.* **2012,** *263*, 671-677.

252. Munir, S.; Shah, S. M.; et al., Effect of carrier concentration on the optical band gap of TiO_2 nanoparticles. *Mater. Des.* **2016,** *92*, 64-72.

253. Ahmad, H.; Kamarudin, S. K.; et al., Hydrogen from photo-catalytic water splitting process: A review. *Renewable Sustainable Energy Rev.* **2015,** *43*, 599-610.

254. Alamgir; Khan, W.; et al., Formation of self-assembled spherical-flower like nanostructures of cobalt doped anatase TiO_2 and its optical band-gap. *Mater. Lett.* **2014,** *133*, 28-31.

255. Tang, H.; Prasad, K.; et al., Electrical and optical properties of TiO_2 anatase thin films. *J. Appl. Phys.* **1994,** *75* (4), 2042-2047.

256. Litter, M. I., Heterogeneous photocatalysis: Transition metal ions in photocatalytic systems. *Appl. Catal., B* **1999,** *23* (2-3), 89-114.

257. Choi, W.; Termin, A.; et al., The Role of Metal Ion Dopants in Quantum-Sized TiO_2: Correlation between Photoreactivity and Charge Carrier Recombination Dynamics. *J. Phys. Chem.* **1994,** *98* (51), 13669-13679.

258. Zhao, G.; Kozuka, H.; et al., Sol-gel preparation of $Ti_{1-x}V_xO_2$ solid solution film electrodes with conspicuous photoresponse in the visible region. *Thin Solid Films* **1999,** *339* (1-2), 123-128.

259. Kemp, T. J. and McIntyre, R. A., Transition metal-doped titanium(IV) dioxide: Characterisation and influence on photodegradation of poly(vinyl chloride). *Polym. Degrad. Stab.* **2006,** *91* (1), 165-194.

260. Weng, H.; Yang, X.; et al., Electronic structure and optical properties of the Co-doped anatase TiO_2 studied from first principles. *Phys. Rev. B: Condens. Matter Mater. Phys.* **2004,** *69* (12), 125219.

261. Cotton, F. A.; Wilkinson, G.; et al., *Basic Inorganic Chemistry*. 3rd ed.; John Wiley & Sons, Inc.: New York, 1995; p 838.

262. Shannon, R., Revised effective ionic radii and systematic studies of interatomic distances in halides and chalcogenides. *Acta Crystallogr., Sect. A: Found. Adv.* **1976,** *32* (5), 751-767.

263. Choudhury, B.; Dey, M.; et al., Shallow and deep trap emission and luminescence quenching of TiO_2 nanoparticles on Cu doping. *Appl. Nanosci.* **2014,** *4* (4), 499-506.

264. Yang, Y.; Zhong, H.; et al., Single-step preparation, characterization and photocatalytic mechanism of mesoporous Fe-doped sulfated titania. *Surf. Sci.* **2011,** *605* (13-14), 1281-1286.

265. Sun, D.; Wang, K.; et al., Synthesis and photocatalytic activity of sulfate modified Nd-doped TiO_2 under visible light irradiation. *J. Rare Earths* **2015,** *33* (5), 491-497.

266. Lincoln, S. F. and Stranks, D. R., Phosphato complexes of cobalt(III). I. General structural and hydrolytic properties. *Aust. J. Chem.* **1968,** *21* (1), 37-56.

267. Heger, D.; Jirkovsk, J.; et al., Aggregation of Methylene Blue in Frozen Aqueous Solutions Studied by Absorption Spectroscopy. *J. Phys. Chem. A* **2005,** *109* (30), 6702-6709.

268. Sohrabnezhad, S., Study of catalytic reduction and photodegradation of methylene blue by heterogeneous catalyst. *Spectrochim. Acta, Part A* **2011,** *81* (1), 228-235.

269. Qu, P.; Zhao, J.; et al., TiO_2-assisted photodegradation of dyes: A study of two competitive primary processes in the degradation of RB in an aqueous TiO_2 colloidal solution. *J. Mol. Catal. A: Chem.* **1998,** *129* (2-3), 257-268.

270. Tseng, I. H.; Chang, W.-C.; et al., Photoreduction of CO_2 using sol-gel derived titania and titania-supported copper catalysts. *Appl. Catal., B* **2002,** *37* (1), 37-48.

271. Tseng, I. H.; Wu, J. C. S.; et al., Effects of sol-gel procedures on the photocatalysis of Cu/TiO_2 in CO_2 photoreduction. *J. Catal.* **2004,** *221* (2), 432-440.

272. Liu, Y.; Liu, J.; et al., Simple fabrication and photocatalytic activity of S-doped TiO_2 under low power LED visible light irradiation. *Ceram. Int.* **2009,** *35* (8), 3061-3065.

273. Fujishima, A.; Zhang, X.; et al., TiO_2 photocatalysis and related surface phenomena. *Surf. Sci. Rep.* **2008,** *63* (12), 515-582.

274. Darkins, R.; Sushko, M. L.; et al., Adhesion of Sodium Dodecyl Sulfate Surfactant Monolayers with TiO2 (Rutile and Anatase) Surfaces. *Langmuir* **2013,** *29* (37), 11609-11614.

275. Tielens, F.; Gervais, C.; et al., Characterization of Phosphate Species on Hydrated Anatase TiO_2 Surfaces. *Langmuir* **2015,** *32* (4), 997-1008.

276. Zhao, D.; Chen, C.; et al., Surface Modification of TiO by Phosphate: Effect on Photocatalytic Activity and Mechanism Implication. *J. Phys. Chem. C* **2008,** *115* (15), 5993-6001.

277. Bae, E.; Choi, W.; et al., Effects of Surface Anchoring Groups (Carboxylate vs Phosphonate) in Ruthenium-Complex-Sensitized TiO_2 on Visible Light Reactivity in Aqueous Suspensions. *J. Phys. Chem. B* **2004,** *108* (37), 14093-14101.

278. Ernstorfer, R.; Gundlach, L.; et al., Role of Molecular Anchor Groups in Molecule-to-Semiconductor Electron Transfer. *J. Phys. Chem. B* **2006,** *110* (50), 25383-25391.

279. Mao, L.; Li, Q.; et al., Synthesis of nanocrystalline TiO_2 with high photoactivity and large specific surface area by sol-gel method. *Mater. Res. Bull.* **2005,** *40* (2), 201-208.

280. McPhaden, M. J. El Niño Theme Page. (accessed Nov 2012).

281. Perez-Huerta, A.; Etayo-Cadavid, M. F.; et al., El Nino Impact on Mollusk Biomineralization-Implications for Trace Element Proxy Reconstructions and the Paleo-Archeological Record. *PLoS One* **2013,** *8* (2), e54274.

282. Rollins, H. B.; Sandweiss, D. H.; et al., Effect of the 1982 - 1983 El Niño on bivalve mollusks. *Nat. Geogr. Res.* **1986,** *2*, 106-112.

283. Mann, S., *Biomineralization: Principles and Concepts in Bioinorganic Materials Chemistry*. Oxford Univeristy Press: Bristol, **2001**; p 191.

284. Trust, T. W. P. C. S. http://www.pengellytrust.org/museum/aragonite/images/aragonite_crystalline_structure.gif (accessed Sep. 16, 2014).

285. Fiondella, F. Eight Misconceptions About El Niño (and La Niña). http://iri.columbia.edu/news/eight-misconceptions-about-el-nino/ (accessed Dec. 12, 2014).

286. McPhaden, M. J. What is an El Nino? http://www.pmel.noaa.gov/tao/elnino/el-nino-story.html (accessed Nov 2012).

287. Barber, R. T. and Chavez, F. P., Biological Consequences of El Niño. *Science* **1983,** *222* (4629), 1203-1210.

288. Andrus, C.; Hodgins, G.; et al., Molluscan radiocarbon as a proxy for El Niño-related upwelling variation in Peru. *Spec. Pap. - Geol. Soc. Am.* **2005,** *395* (13-20).

289. Rutt, H. N. and Nicola, J. H., Raman spectra of carbonates of calcite structure. *J. Phys. C: Solid State Phys.* **1974,** *7* (24), 4522.

290. Edwards, H. G. M.; Villar, S. E. J.; et al., FT-Raman spectroscopic study of calcium-rich and magnesium-rich carbonate minerals. *Spectrochim. Acta, Part A* **2005,** *61* (10), 2273-2280.

291. Hild, S.; Marti, O.; et al., Spatial distribution of calcite and amorphous calcium carbonate in the cuticle of the terrestrial crustaceans Porcellio scaber and Armadillidium vulgare. *J. Struct. Biol.* **2008,** *163* (1), 100-108.

292. dePaula, S. M.; Huila, M. F. G.; et al., Confocal Raman and electronic microscopy studies on the topotactic conversion of calcium carbonate from Pomacea lineate shells into hydroxyapatite bioceramic materials in phosphate media. *Micron* **2010,** *41* (8), 983-989.

293. Soldati, A. L.; Jacob, D. E.; et al., Micro-Raman spectroscopy of pigments contained in different calcium carbonate polymorphs from freshwater cultured pearls. *J. Raman Spectrosc.* **2008,** *39* (4), 525-536.

294. Cusack, M.; Curry, G.; et al., An intracrystalline chromoprotein from red brachiopod shells: Implications for the process of biomineralization. *Comparative Biochemistry and Physiology Part B: Comparative Biochemistry* **1992,** *102* (1), 93-95.

295. Bandaranayake, W. M., The nature and role of pigments of marine invertebrates. *Nat. Prod. Rep.* **2006,** *23* (2), 223-255.

296. Addadi, L.; Joester, D.; et al., Mollusk Shell Formation: A Source of New Concepts for Understanding Biomineralization Processes. *Chemistry – A European Journal* **2006,** *12* (4), 980-987.

297. Shuler, S. F. Dendrimer-Mediated Formation of Cobalt Nanoparticles via Ultraviolet Irradiation. Ph.D., The University of Alabama, Tuscaloosa, 2008.

APPENDIX

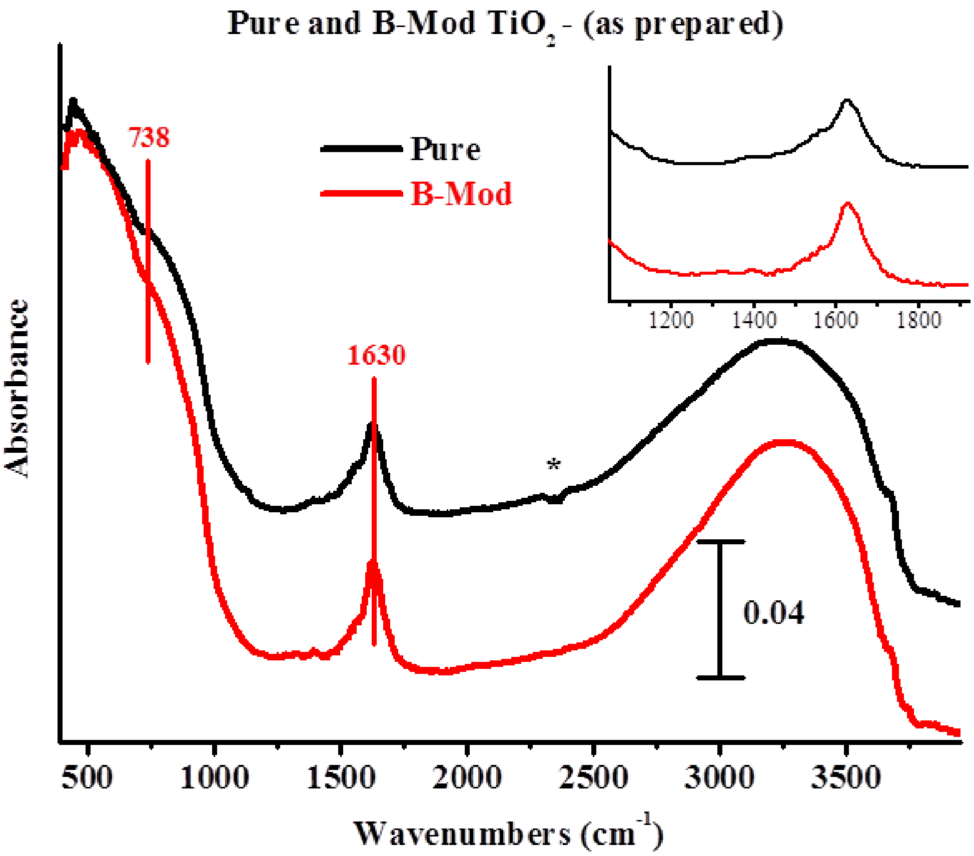

Figure A.1: FTIR of Pure and B-Mod TiO_2

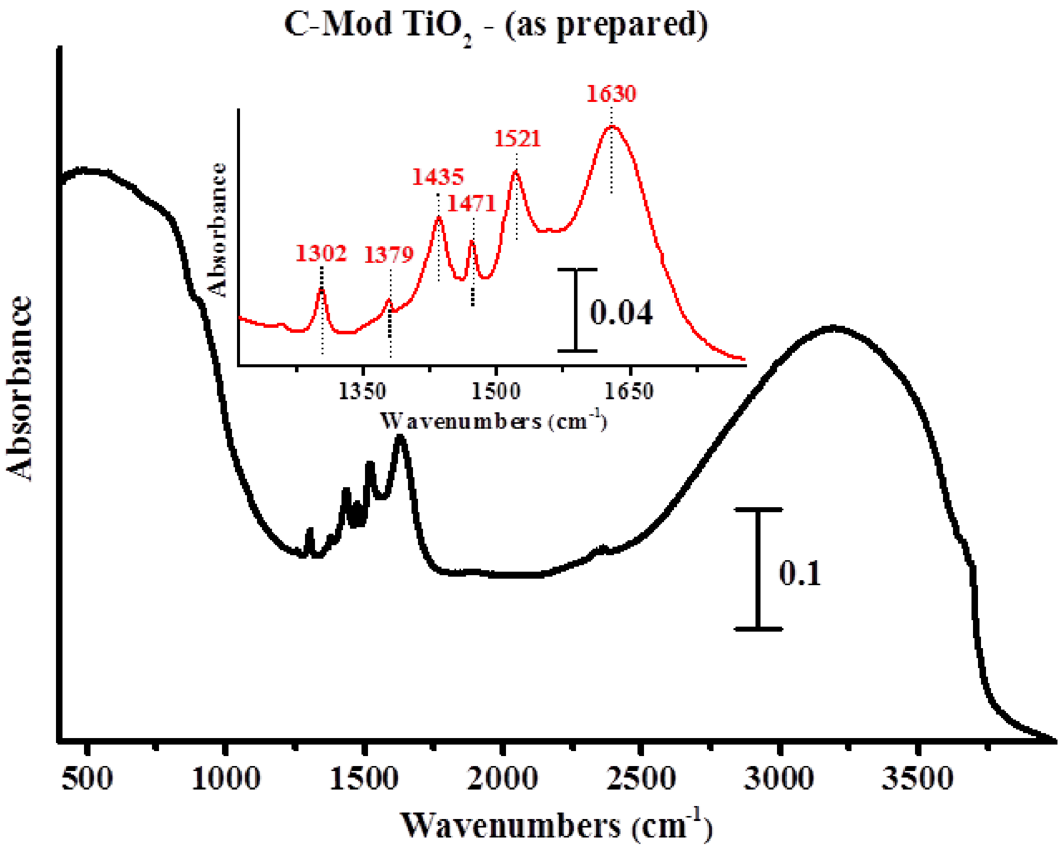

Figure A.2: FTIR of C-Mod TiO$_2$

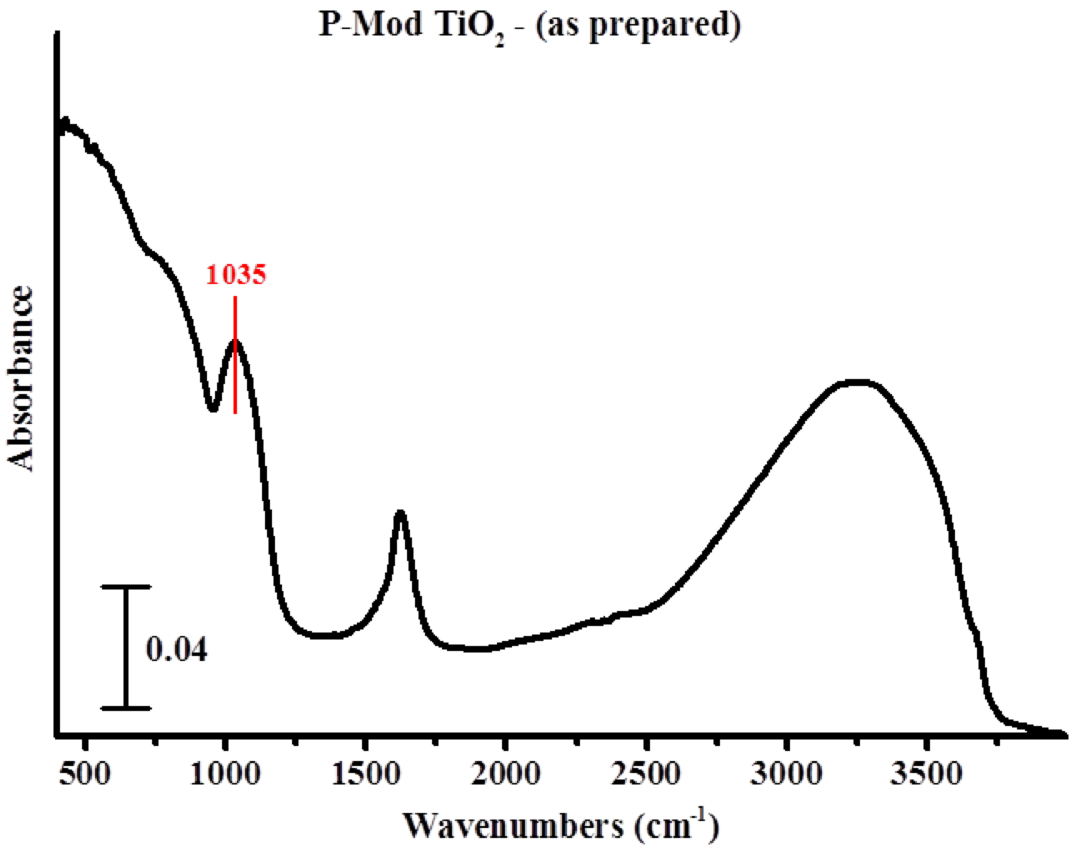

Figure A.3: FTIR of P-Mod TiO$_2$

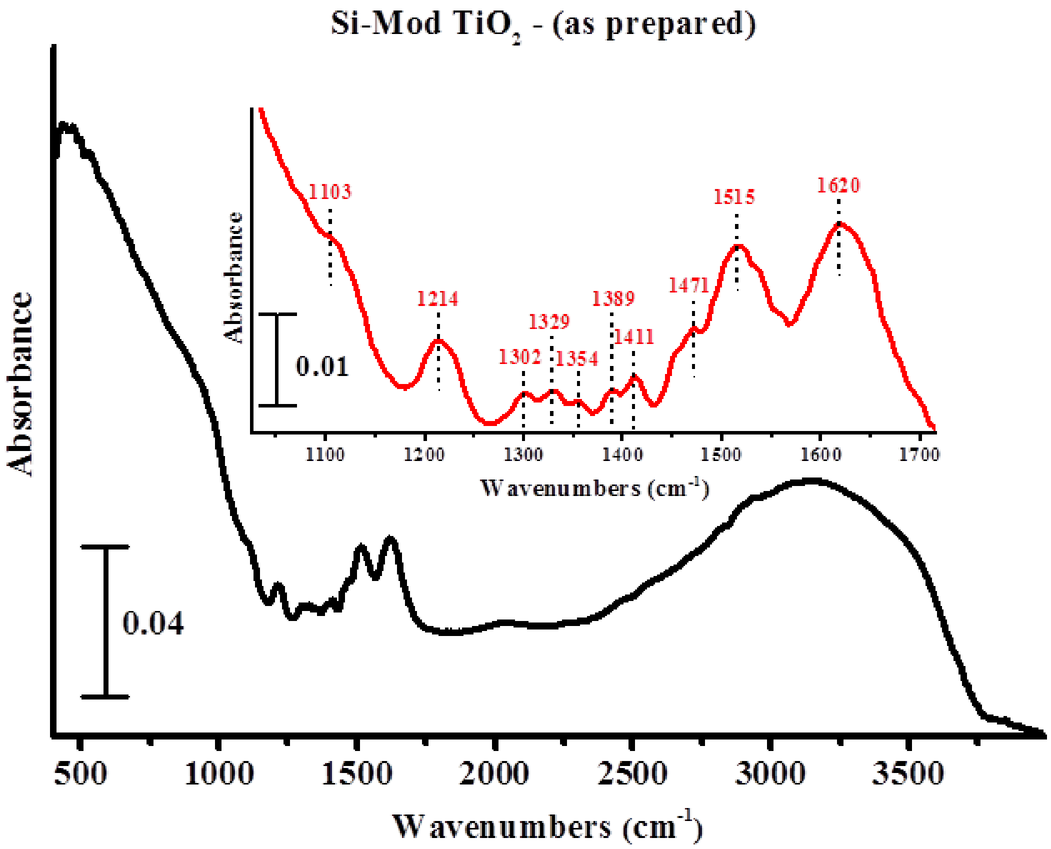

Figure A.4: FTIR of Si-Mod TiO_2

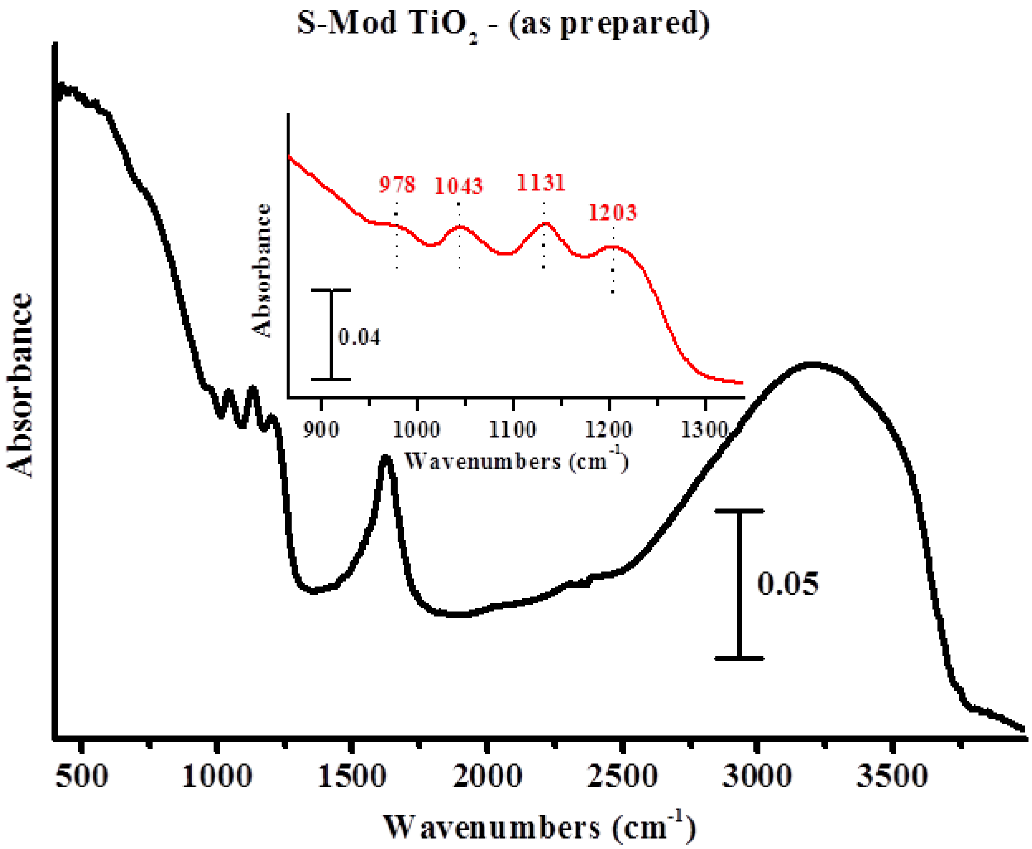

Figure A.5: FTIR of S-Mod TiO_2

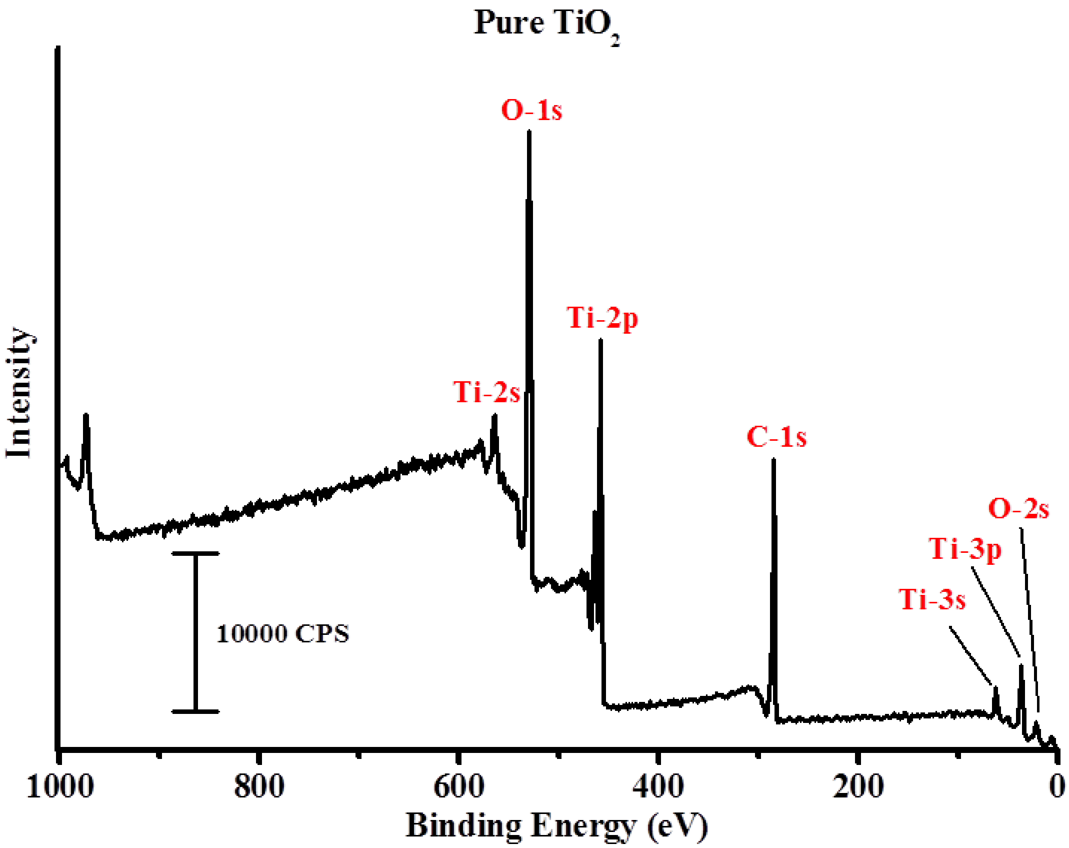

Figure A.6: XPS of Pure TiO$_2$

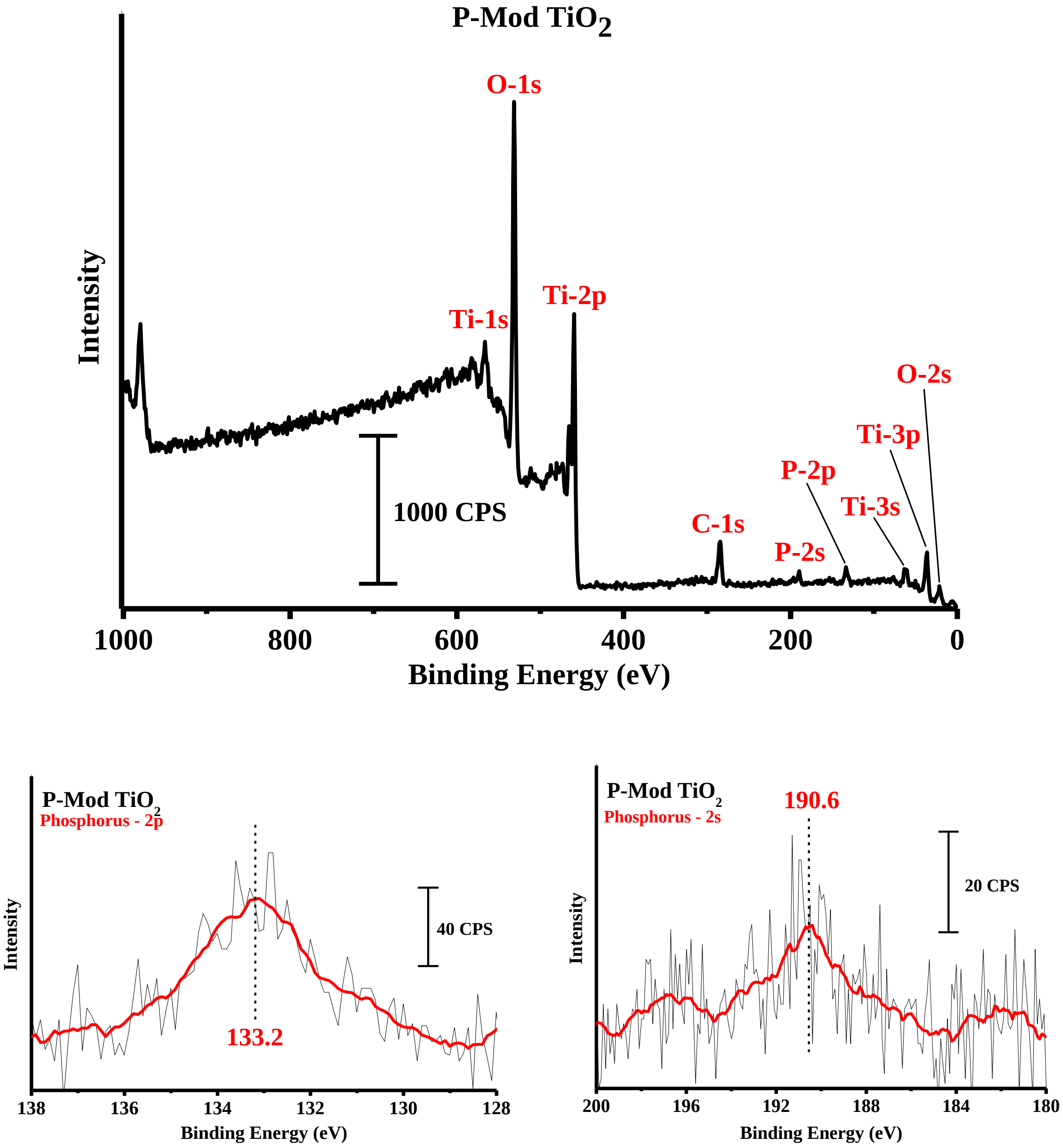

Figure A.7: XPS of P-Mod TiO_2

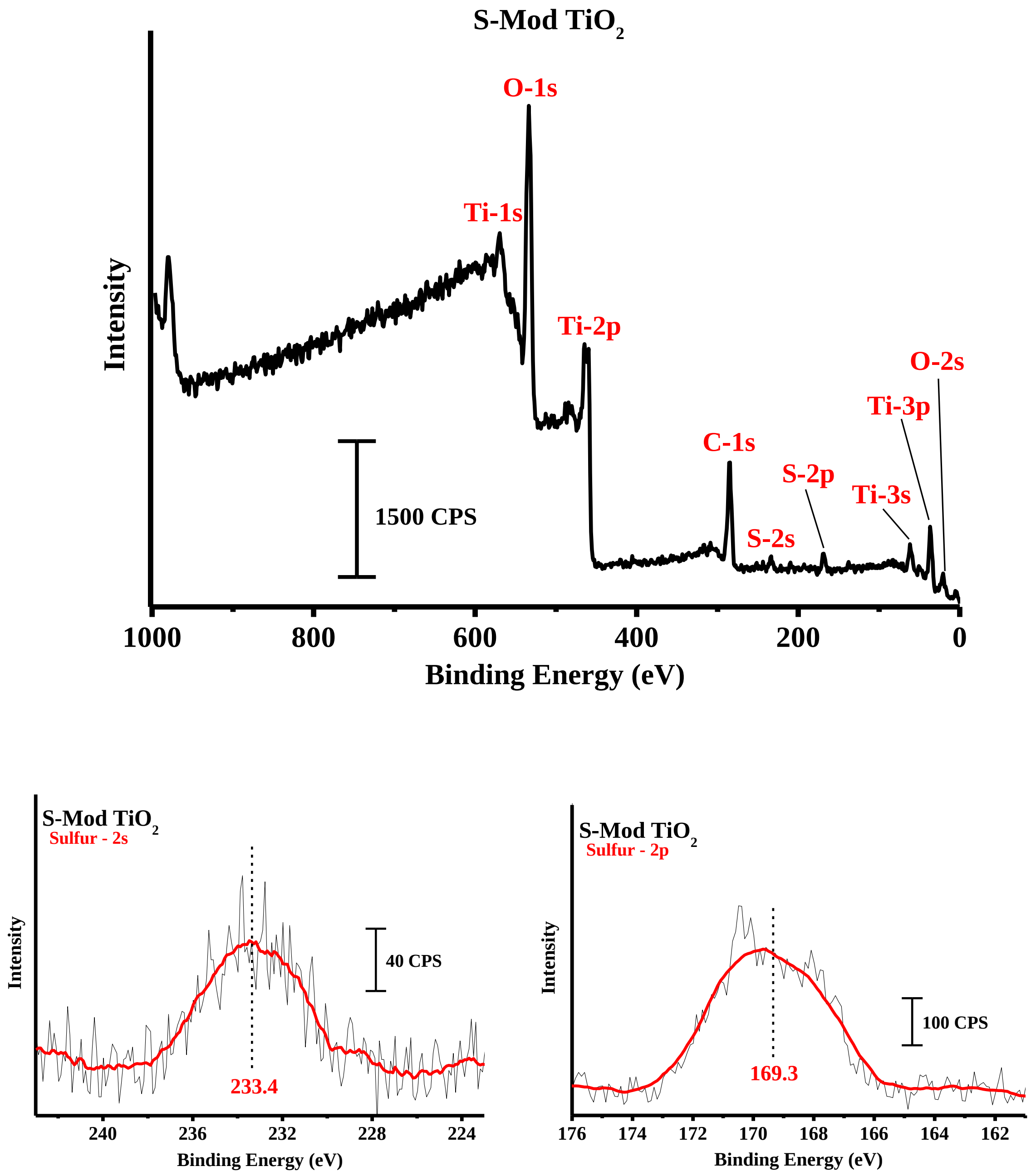

Figure A.8: XPS of S-Mod TiO_2

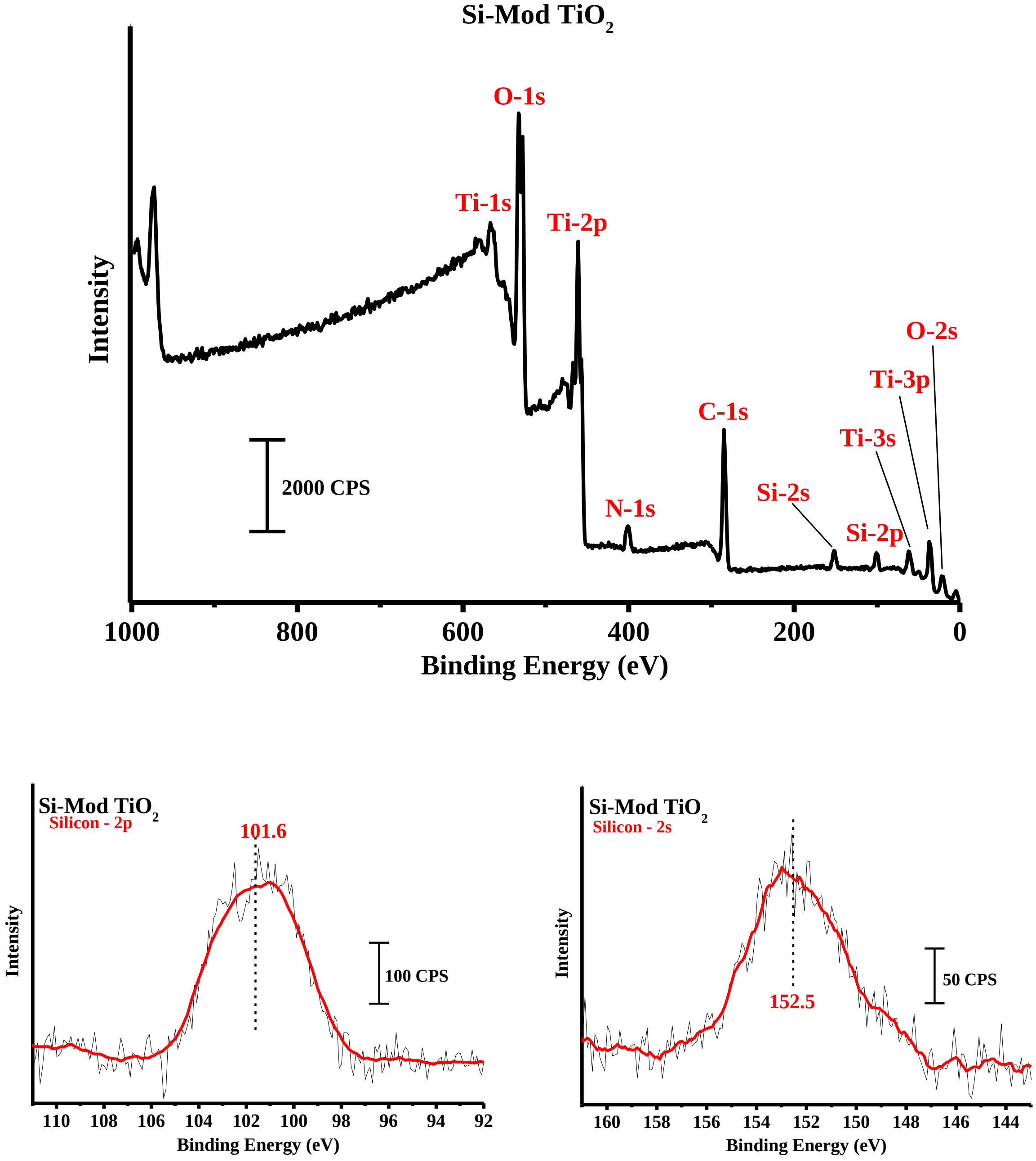

Figure A.9: XPS of Si-Mod TiO_2

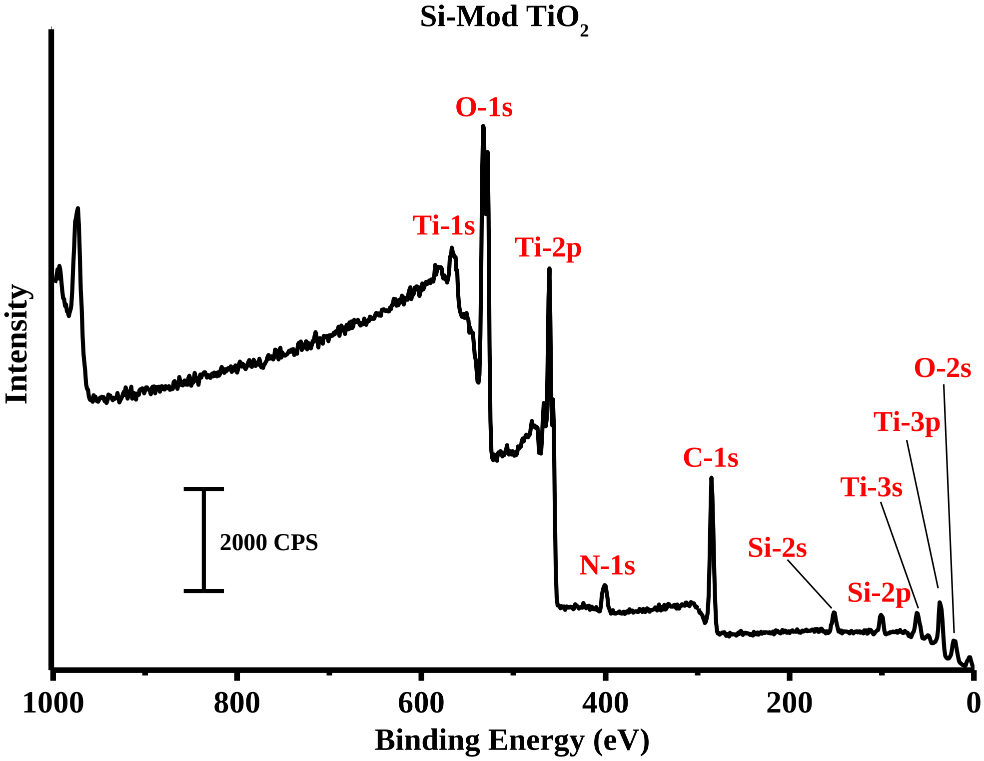

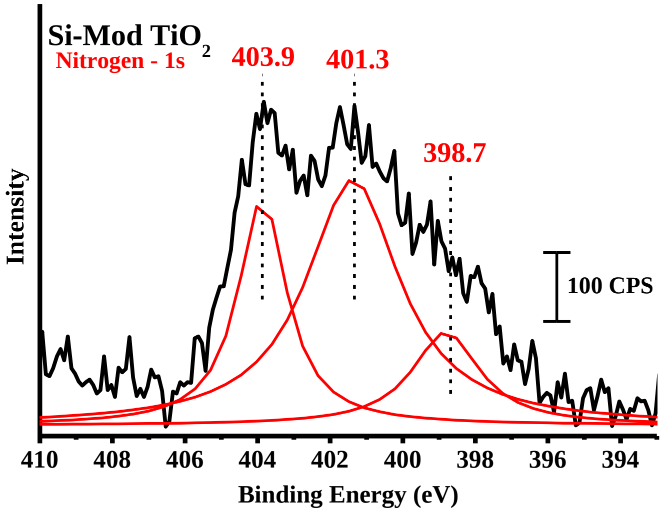

Figure A.10: XPS of Si-Mod TiO_2